

ZINC OXIDE SPUTTER DEPOSITION AND MODELING OF
COPPER-INDIUM-GALLIUM-DISELENIDE-BASED THIN FILM SOLAR CELLS

By

WEI LIU

A DISSERTATION PRESENTED TO THE GRADUATE SCHOOL
OF THE UNIVERSITY OF FLORIDA IN PARTIAL FULFILLMENT
OF THE REQUIREMENTS FOR THE DEGREE OF
DOCTOR OF PHILOSOPHY

UNIVERSITY OF FLORIDA

2007

© 2007 Wei Liu

To my beloved parents and family

ACKNOWLEDGMENTS

Dr. Crisalle is the chair of my supervisory committee and I express my sincere appreciation for his guidance and constant encouragement through the last five years. I am also obliged to thank Dr. Hoflund, Dr. Svoronos and Dr. Eisenstadt for their valuable discussions and serving as my research committee members. Of course my gratitude should be given to Dr. Holloway for his supports and suggestions based on his profound knowledge on vacuum science. Dr. Anderson, Dr. Li also provided a lot of support during the last five years and I would like to express my appreciation. I also thank Dr. Craciun for his valuable discussions on thin film characterization.

This work would not have been achieved without the collaborations from my colleagues working on the CIGS solar cell projects at University of Florida. In particular, I hereby extend my thanks to Xuege Wang, Ryan Kaczynski, Lei Li, Ryan Acher and Andre Baran for their valuable discussions and collaborations on device fabrication. Dr. Mark Davidson, Evan Law and Dr. Lei Qian from Dr. Holloway's group also provided their kind helps at different points of this work. I would like to show my sincere thanks to them.

Of course the acknowledgement would never be complete without expressing my gratitude to my parents. I own everything to them and the word is never enough to express my appreciation. Without their support and encouragement, I would not have made it to this point of my life.

TABLE OF CONTENTS

	<u>page</u>
ACKNOWLEDGMENTS	4
LIST OF TABLES	8
LIST OF FIGURES	9
ABSTRACT	12
CHAPTER	
1 INTRODUCTION	14
2 LITERATURE REVIEW	18
Solar Light	18
The Photovoltaic Effect	19
History of Photovoltaic Technology	19
Device Physics	20
Solar Cells using Different Materials	22
Crystalline Silicon Solar Cells	23
Single crystalline silicon	23
Polycrystalline silicon	24
Thin Film Solar Cells	25
Amorphous silicon	25
CuInSe ₂ and CuGaSe ₂	27
Transparent Conductive Oxide	28
Sputter Deposition	30
Introduction	30
Advantages of Sputter Deposition	31
Sputter Deposition of ZnO	32
Summary	33
3 EXPERIMENTAL METHODS	40
ZnO Sputtering System	40
Substrate Cleaning	42
Characterization Techniques	43
Electrical Property Characterization	43
Four-point probe	43
Hall measurement	44
Optical Spectrophotometer Characterization	45
Other Characterizations	46
Profilometry	46
X-Ray Diffraction	47

	Atomic Force Microscopy.....	49
	Auger Electron Spectroscopy.....	51
4	GROWTH AND CHARACTERIZATION OF ZINC OXIDE.....	56
	Optimization of Sputter Deposition of Aluminum Doped ZnO	56
	Experiments at Different Base Pressures	56
	Optical property.....	57
	Electrical property.....	58
	Growth rate.....	58
	Power Effect.....	59
	Working Pressure Effect.....	61
	Characterization.....	62
	Auger Electron Spectroscopy Analysis	62
	Surface scan.....	63
	Al sensitivity	64
	Depth profile	65
	Atomic Force Microscopy	65
5	EFFECT OF HYDROGEN ON SPUTTERED ZINC OXIDE.....	78
	Motivation from the Base Pressure Effect.....	78
	Experiments and Results.....	78
	Hall Characterization.....	79
	AFM and SEM Characterization.....	80
	Film Uniformity Study	81
	Summary.....	83
6	DEVICE FABRICATION AND CHARACTERIZATION.....	92
	Device Fabrication Procedure.....	92
	Substrate	92
	Back Contact Sputtering.....	92
	Absorber Growth.....	93
	Buffer Layer Deposition.....	94
	Window Layer Deposition	95
	Metallization.....	96
	Device Characterization System.....	96
	Devices with Absorbers from UF PMEE Reactor.....	97
	CIGS Devices	97
	CGS Devices	98
	Effect of Zinc Oxide Window Layer on Device Performance	99
	Effect of Window Layer Transmission	100
	Effect of Sheet Resistance.....	101
	Impact of the Intrinsic ZnO Layer.....	102
	Summary.....	102

7	INVERSE MODELING OF CIGS SOLAR CELLS.....	110
	Definition of Inverse Modeling.....	110
	Inverse Modeling for Photovoltaic Cells.....	111
	Application of Inverse Modeling — Performance Optimization	112
	Approach.....	112
	Forward Modeling.....	113
	Cell structure generation	113
	Input parameters.....	114
	Example of a forward modeling.....	114
	Modeling of NREL champion device	116
	Inverse Modeling.....	116
	Inverse Modeling of NREL champion device.....	117
8	CONCLUSION.....	130
	Parameter Effects on Sputtered AZO	130
	Device Fabrication.....	131
	Defects in CIGS Absorbers	132
	Future Work.....	132
	LIST OF REFERENCES.....	134
	BIOGRAPHICAL SKETCH	138

LIST OF TABLES

<u>Table</u>	<u>page</u>
4-1	Estimated grain size using XRD data obtained for AZO deposited at different power.....77
4-2	Parameters used for collecting the Auger depth profile of AZO thin films.....77
4-3	AFM surface roughness evolution with working pressure.77
5-1	Growth parameters comparison for AZO and H-AZO thin films.....91
5-2	Deposition condition comparison between two AZO thin films shown in Figure 5-5.....91
5-3	Thickness, Rq and estimated grain size comparison between two AZO thin films shown in Figure 5-5.91
5-4	Roughness data evolution with increasing film thickness.91
5-5	Hall measurements results on two films with different positions under the target.....91
5-6	Comparison of Hall and four-point-probe measurement results.....91
6-2	Recipe for CdS buffer layer deposition.104
6-3	Composition and thickness data for UF CIGS absorbers.104
6-4	Calibration of the reference cell.....104
6-5	I-V character of the UF CIGS devices.....105
6-6	Growth recipe and composition for UF CGS absorbers.105
6-7	I-V character of the UF CGS devices.105
6-8	Performance of CIGS solar cells with different window layer transmission.....105
6-9	Performance of CIGS solar cells with and without i-ZnO layer.....105
7-1	Typical input parameters for Medici.....129

LIST OF FIGURES

<u>Figure</u>	<u>page</u>
2-1 Energy current density per wavelength of AM0 spectrum(heavy line) compared with blackbody radiation at 5800K(thin line).	34
2-2 Schematic of the Air Mass definition.	34
2-3 Energy current density per photon energy of AM1.5 spectrum (heavy line) compared with blackbody radiation at 5800K (thin line).	35
2-4 Formation of built-in potential between p-n junction.	35
2-5 An equivalent circuit of a typical solar cell.	36
2-6 Effect of series resistance and shunt resistance on solar cell performance.....	36
2-7 Effect of series resistance on solar cell performance.....	37
2-8 World PV market share by technology in 2002.....	38
2-9 Development history of thin film solar cells. (Courtesy of NREL).....	38
2-10 Thin film CIGS solar cell structure.....	39
3-1 Perkin-Elmer 4400 sputtering system.....	53
3-2 Schematic of the ZnO Sputtering System (Perkin-Elmer 4400).....	53
3-3 Schematics of four-point probe measurement.	54
3-4 Square shaped van der Pauw sample geometry.	54
3-5 Generation of Cu K α radiation.	55
3-6 Bragg's condition.....	55
4-1 The effect of base pressure on the optical transmission of sputtered AZO films.	68
4-2 Effect of base pressure on the resistivity of sputtered AZO films.....	68
4-3 The effect of base pressure on the growth rate of ZnO:Al thin films (Fixed conditions: $D_{ts} = 5$ cm, $P = 4$ mTorr, Power = 400W).....	69
4-4 The effect of power on the resistivity of as grown ZnO:Al thin films (Fixed conditions: $D_{ts} = 5$ cm, $P_b = 8.0 \times 10^{-7}$ Torr, and $P = 4$ mTorr).....	69

4-5	The effect of power on the growth rate of ZnO:Al thin films (Fixed conditions: $D_{ts} = 5$ cm, $P_b = 8.0 \times 10^{-7}$ Torr, and $P = 4$ mTorr).	70
4-6	X-ray diffraction pattern of thin films deposited from a reduced ZnO target	70
4-7	X-ray diffraction pattern of thin films deposited from an oxidized ZnO target	71
4-8	High resolution XRD pattern for AZO films deposited using different power (Fixed conditions: $D_{ts} = 5$ cm, $P_b = 8.0 \times 10^{-7}$ Torr, Pressure = 4mTorr).	71
4-9	The effect of working pressure on the resistivity of ZnO:Al thin films (Fixed conditions: $D_{ts} = 5$ cm, $P_b = 8.0 \times 10^{-7}$ Torr, and Power = 500 W)	72
4-10	The effect of working power on the growth rate of ZnO:Al thin films (Fixed conditions: $D_{ts} = 5$ cm, $P_b = 8.0 \times 10^{-7}$ Torr, and Power = 500 W)	72
4-11	High resolution XRD pattern of AZO thin films deposited at different working pressures (Fixed conditions: $D_{ts} = 5$ cm, $P_b = 4.0 \times 10^{-7}$ Torr, Power = 500 W).	73
4-12	AES survey scan pattern for an AZO thin film with organic contamination on the surface.	73
4-13	AES scan results after sputtering for 3 minutes.	74
4-14	Al Auger peak shown by using increased primary beam energy.	74
4-15	Depth profile for each element of AZO obtained with AES.	75
4-16	AFM graph of AZO thin films deposited with different working pressure. a) 2mTorr, $R_q = 2.2$ nm; b) 3mTorr, $R_q = 2.8$ nm; c) 4mTorr, $R_q = 3.6$ nm.	76
5-1	Effect of injecting hydrogen gas on the resistivity of sputtered AZO films.	85
5-2	Hall measurement results for aluminum-zinc-oxide thin films deposited using only argon as the working gas (sample labeled as AZO) and using a mixture of argon with 0.1 wt% of hydrogen (sampled labeled H-AZO).	85
5-3	AFM image of two AZO films deposited using different sputtering gas. a) AZO b) H-AZO	86
5-4	AFM image of H-AZO thin films with increasing thickness. a)200nm b)400nm c)600nm d)800nm.....	87
5-6	Variation of AZO thickness with different positions along the axial direction.	89
5-7	Variation of sheet resistance with different positions along the axial direction.	89
5-8	Variation of resistivity with different positions along the axial direction.	90

6-1	Schematic of the PMEE reactor.....	106
6-2	Photo of CIGS solar cells fabricated on a 2”×1” soda-lime glass substrate.	106
6-3	Cross section SEM image of absorber #582.....	107
6-4	Cross-section SEM image of absorber #588.....	107
6-5	Cross-section SEM image of CGS device #640.	108
6-6	AZO window layer optical transmission of three CIGS solar cells.....	109
6-7	CIGS cell efficiency versus the AZO layer sheet resistance.	109
7-1	Schematic diagram illustrating the forward modeling and inverse modeling operations for a given physical system S	120
7-2	Parameter classification with examples for solar devices.....	121
7-3	Procedure chart for solar cell inverse modeling.	122
7-4	A typical CIGS cell structure.....	123
7-5	Cell structure described in Medici.	123
7-7	A typical I-V curve generated by Medici.	124
7-8	Medici simulation result for an NREL champion device.	125
7-9	Iteration of inverse modeling process for there solar cell performance variables: (a) I_{sc} , (b) V_{oc} , and (c) FF . (Case 1).....	126
7-10	Iteration of inverse modeling process for there solar cell performance variables: (a) I_{sc} , (b) V_{oc} , and (c) FF . (Case 2).....	127
7-11	Iteration of inverse modeling process for there solar cell performance variables: (a) I_{sc} , (b) V_{oc} , and (c) FF . (Case 3).....	128

Abstract of Dissertation Presented to the Graduate School
of the University of Florida in Partial Fulfillment of the
Requirements for the Degree of Doctor of Philosophy

ZINC OXIDE SPUTTER DEPOSITION AND MODELING OF
COPPER-INDIUM-GALLIUM-DISELENIDE-BASED THIN FILM SOLAR CELLS

By

Wei Liu

December 2007

Chair: Oscar D. Crisalle
Major: Chemical Engineering

Highly transparent and conductive aluminum doped zinc oxide (AZO) thin films were successfully obtained through RF magnetron sputtering using argon as the sputtering gas. Thin film AZO grown under different conditions such as base pressure, deposition power and working pressure was characterized. A correlation between various operational parameters and the optical and electrical properties of AZO was developed and used to suggest optimum of operational conditions.

The sputtering process was improved by adding a small amount of hydrogen into the sputtering gas. A significant improvement of the conductivity of AZO thin films was observed. This observation together with results obtained under different base pressures supports the literature prediction that hydrogen plays a favorable role in n-type zinc oxide thin films. Hydrogen participates in the doping process and causes increased carrier concentration.

The AZO thin films sputtered with the Ar and H₂ mixture gas were incorporated in copper-indium-gallium diselenide (CIGS) solar cells and devices with a thin film layer structure of the form ZnO/CdS/CIGS/Mo were fabricated. It is found that the sheet resistance and thickness of the AZO layer can be an important factor determining the performance of CIGS solar cells. The

devices were measured under AM 1.5 radiation and a conversion efficiency of approximately 9% was achieved.

To better understand solar cell devices fabricated using chalcopyrite semiconductors such as CuInSe_2 and CuGaSe_2 , an inverse modeling process was developed. The inverse modeling process was realized by integrating two software tools, namely Matlab and Medici, under a Linux environment. Matlab provides the values of candidate input parameters to Medici, which in turn outputs device simulation results that are fed back to Matlab. This process continues until the outputs reach the target values. The inverse modeling process successfully identified the defect distribution in a CIGS layer that matched a known cell performance. In an ensuing optimization step, optimal defect concentrations were found, revealing that the shallow acceptor defect concentrations are favorable for increasing the efficiency.

CHAPTER 1 INTRODUCTION

With the decline of the traditional fossil fuel resources in the world, renewable energy sources are emerging as the future solution to maintain a sustainable development of human society. Among various kinds of renewable energy solutions including hydroelectric, geothermal, wind, and solar (photovoltaic and thermal), photovoltaic technology has attracted more and more attentions for its advantages over other options. Photovoltaic technology has the following advantages. The first advantage is the abundant energy source. The sun is a reliable energy source and it constantly radiates a tremendous amount of energy toward the earth. The second advantage is clean and environmentally friendly. Photovoltaic devices, commonly known as solar cells, convert the energy from sunlight directly into electricity. There is no emission, noise or pollution of any kind during the operation. With more and more concerns about the “greenhouse gases” and their detrimental effect on our planet, with the awareness of the possibility of irreversible environmental pollution that could be brought by nuclear power, the value of PV technology as a clean, renewable energy source has been increasingly appreciated. The third advantage is reliability. PV technology was originally developed for space applications where solar cells were used to power satellites. With no moving parts, solar cells can operate reliably and require little maintenance. With all these advantages, solar energy is emerging as a promising alternative to traditional energy sources.

The amount of light energy available annually in a particular landmass on earth depends on the climate and the latitude. In areas closer to the equator, available energy per unit area is larger. On average between 2 and 3 megawatt-hours (MWh) of solar energy falls on a square meter of land in the United States annually. Accordingly, computed annual solar energy available over the total land area of the United States is about 2.4×10^{16} kWh, which is 10,000

times larger than the annual electricity consumption of the United States [1]. The sun is a huge energy reservoir that could provide the increasing need for energy consumption.

Solar cells have been successfully applied in various fields to provide electricity. Examples of these applications are powering devices on satellites for space applications, providing electricity for remote areas where the power infrastructure is not available. Although cost is not a big concern in these situations, it becomes a major problem for terrestrial applications where power grid is available. When compared with fossil fuels, the relatively high costs of semiconductor materials and processing are a major barrier for the large-scale implementation of solar devices. The high material and fabrication cost keeps the price of solar panels at a high level. As a result, the huge investment on these solar panels may keep consumers from choosing solar electricity considering the fact that it may require tens of years to return the initial investment and start saving consumer's money. Until low cost, highly efficient photovoltaic devices are ready to be fabricated, the application of solar electricity is unlikely to replace the traditional energy source and become the mainstream. Therefore, it is imperative to develop low cost processes and improve performance of PV materials to bring down the cost per watt for solar electricity.

In order to reduce the cost of PV systems, which is usually evaluated in dollars per kilowatt hour (\$/kWh), the current R&D is concentrated on both improving the conversion efficiency and reducing the semiconductor material cost as well as the processing cost. The average residential price for utility-generated electric energy in the U.S. in 1994 was US\$0.079/kWh. In order to reach a cost target as US\$0.06/kWh for electricity from a PV plant operating for 30 years, the module efficiencies are required to be in the range of 15% to 20% for a flat plate panel system and 25% to 30% for a system operating under concentrated sunlight.

These correspond to module area costs of \$45 to \$80/m² and \$60 to \$100/m², respectively [2].

Although the current fabrication cost is still beyond these values, with the favorable green energy policy from governments, such as government solar rebates, more and more solar panels are installed to provide clean utility energy.

Single crystal silicon solar cells have achieved good performance with efficiencies beyond 20%. However, due to the high cost nature of the Czochralski process used to produce single crystal silicon, the price for silicon solar panels remains high. Direct bandgap thin film materials have much higher light absorption coefficient than silicon and require a much less material thickness to absorb the light. They are possible alternatives that could significantly lower the material consumption and consequently the cost. Three typical thin film PV materials are amorphous silicon, cadmium telluride, and copper chalcogenides. Among these thin film PV materials, copper indium gallium di-selenide (CuIn_xGa_{1-x}Se₂ or simply CIGS) is very attractive for its high performance, long-term stability and relatively little toxicity. The work in the scope of this dissertation includes both theoretical analysis of CIGS solar cell device physics through simulation and experimental fabrication and characterization of this kind of solar cells.

A process to grow device quality zinc oxide window layer using an industry sputtering system was developed and optimized. Aluminum doped zinc oxide (AZO) thin films with good optical transmission and resistivity between $1 \times 10^{-3} \Omega \cdot \text{cm}$ and $2 \times 10^{-3} \Omega \cdot \text{cm}$ were repeatedly obtained. It is also observed that residue water vapor in the sputtering chamber is beneficial to the electrical conductivity of aluminum doped zinc oxide. Motivated by this observation, a modified process using hydrogen and argon mixture as the sputtering gas was implemented. Resulted zinc oxide thin films show a lower resistivity. Hall measurement shows that this lowered resistivity was achieved through the increase of carrier concentration in the film.

This process was then successfully applied in CIGS photovoltaic device fabrication. Efficiency of approximately 8% and 9% was achieved on CIGS from Energy Photovoltaic Inc. (EPV) and those from the PMEE reactor at the University of Florida, respectively. This is the first time that CIGS photovoltaic devices are completely fabricated in house, achieving the goal of two previous attempts [3], [4].

Although laboratory scale CIGS devices with efficiency of 19.5% have been achieved experimentally, this material system is not fully understood and many issues remain unknown. For example, the defect distribution in this layer has big impact on the performance of the final device and it is of great interest to investigate the relation between defects and cell performance. In order to do this, software Medici[®] from Synopsys Inc was utilized in simulation to predict solar cell performance under different conditions. An inverse modeling was implemented to identify the defect distribution and their impact on CIGS devices. Solar cell performance was also optimized using the inverse modeling program.

CHAPTER 2 LITERATURE REVIEW

Solar Light

The sun is a hot sphere of gas whose internal temperatures reach over 20 million degrees Kelvin due to nuclear fusion reactions at the sun's core converting hydrogen to helium. The radiation from the inner core is strongly absorbed by a layer of hydrogen closer to the sun's surface. Heat transfers through this layer by convection. The surface of the sun, called the photosphere, is at a temperature of about 6000K and can be represented as a blackbody radiation source.

An immense amount of solar energy radiates toward the earth at any time. The radiation power density at the sun's surface is about 5.96×10^6 mW/cm² and it decreases with increasing the distance from the sun's surface as the radiation sphere gets larger. When reaching the atmosphere of the earth, the sunlight carries a power density of about 135.3mW/cm² [5]. This spectral distribution is referred to as Air Mass Zero (AM0) since it has not passed through the air. Figure 2-1 shows a comparison between AM0 radiation and a blackbody radiation at 5800K [6]. During the process of going through the earth atmosphere, sunlight will be absorbed and scattered and its energy is reduced. Different incident angles will cause different amount of energy loss and this is reflected by Air Mass. In the situation shown in Figure 2-2, Air Mass is defined by

$$AM = \frac{P1}{P2} = \frac{1}{\cos \theta} \quad (2-1)$$

where P1 is the actual path length that light takes through the atmosphere and P2 is the shortest possible path length, i.e., the normal incident distance. For example, AM1.5 refers to sunlight passes through 1.5 atmospheres with a solar zenith angle (θ in Figure 2-2) of 48.19°.

AM1.5 is usually used as incident light for testing terrestrial solar devices. Figure 2-3 shows the comparison between AM1.5 radiation and a blackbody radiation at 5800K [6].

The Photovoltaic Effect

Photovoltaic effect is the creation of an electromotive force by the absorption of photons in a semiconductor device. When photons with energy higher than the energy bandgap of a specific material are radiated on the material, they can be absorbed and the photon energy will excite electrons from the valance band to the conduction band and consequently generate electron hole pairs. To make a solar cell, the electron hole pairs need to be separated before they recombine with each other. Semiconductor p-n junctions were successfully applied to realize this process. When a p-type semiconductor contacts with an n-type semiconductor, a built in electric filed will be generated. This electric field drives any electrons generated in the p-type semiconductor across the junction to the n-type semiconductor. Thus the electron-hole pairs are separated.

History of Photovoltaic Technology

The photovoltaic effect was first discovered by Frenchman Edmund Becquerel in 1839. He observed a special effect while experimenting with an electrolytic cell made up of two metal electrodes. When the metal plates immersed in a suitable electrolyte are exposed under sunlight, a small voltage and current were produced. The first solid-state materials that showed a significant light-dependent voltage were selenium in 1876 and later cuprous oxide, which indicated that semiconductors would eventually become the most promising materials for photovoltaic energy conversion.

PV technological development began with the build up of a silicon p-n junction by a group of researchers at Bell laboratory in 1954 [7]. But the powerful driving force for the PV technological development did not come until the advent of space exploration. The urgent demand for a reliable, long lasting energy source to power the spacecraft became the motivation

of solar cell development. By 1958, the first silicon solar cells were applied on spacecraft. Interest in solar cells as a clean, renewable terrestrial energy source arose after the oil embargoes in 1973 and 1979.

Shay *et al.*[8] at Bell Labs first discovered that the I-III-VI₂ semiconductor (CuInSe₂) can be effectively used as a photovoltaic material in the 1970s. A polycrystalline CuInSe₂ cell of nearly 6% efficiency was developed at the University of Maine in 1976 [9]. Over a period of more than one decade starting from early 1980s, a research group at Boeing was able to consistently push up the efficiency of polycrystalline chalcopyrite solar cells to a higher value when it reached 13.7% in 1993 [10]. The Boeing CIS project was ceased not long after that. The research of CIGS technology are later led by researchers at the National Renewable Energy Lab (NREL), who reported an conversion efficiency beyond 19% in 2003 [11]. CIGS technology has also been transferred to industry pilot production both in Europe and the United States. It is becoming a promising thin film technology that can dramatically lower the production cost.

Device Physics

Most solar cells rely on p-n junction to separate the photon generated electron and hole pairs. The p-n junctions are formed by joining a p-type and n-type semiconductor together. Once connected, diffusion happens due to the concentration difference of electrons and holes between these two types of semiconductors. Since the n-type semiconductor has a high electron concentration and the p-type a high hole concentration, electrons diffuse from the n-type region to the p-type region. Similarly, holes flow by diffusion from the p-type region to the n-type region. Because electrons and holes are charged, their diffusion causes charge redistribution in the junction area and an internal electric field is formed across the junction. The region where the electric field is present is called “space charge region”. All free carriers in the space charge

region are quickly swept away by the electric field and therefore this layer is also called as “depletion region” due to the unavailability of free carriers. As a result of the electric field, a built-in potential is present across the junction. This process can also be explained by the Fermi level alignment between the p-type and n-type region due to the diffusion of electrons and holes, which is shown in Figure 2-4. Under thermal equilibrium, both diffusion and drift happens and their current balance and there is no net current flow through the junction.

When the p-n junction is illuminated by photons whose energy is larger than the bandgap, electron and hole pairs are generated. These free carriers generally have very short lifetime and they will recombine with each other if they are not separated in a timely fashion. However, the built-in potential across the junction will swiftly sweep the electrons and holes across the junction so that photon generated electrons reaches the n-type region and holes the p-type region, where they become the so called majority carriers and no longer suffer a fast recombination. If the p-n junction is connected with external circuit, the light generated current flows out and the semiconductor p-n junction becomes a solar cell. If the p-n junction is not externally connected, i.e., under open circuit condition, the photon generated current will produce a forward bias across the diode, which reduces the barrier for diffusion and promotes the diffusion current to balance out the photon generated current. At equilibrium, the net current still remains zero. This forward bias created is referred to as open circuit voltage (V_{oc}).

Figure 2-5 shows an equivalent circuit of a solar cell [12]. R_s represents series resistance. Series resistance comes from the resistance of the material that constitutes the solar cell and the contact resistance between the body material and external circuit. R_{sh} represents shunt resistance, which is the resistance in parallel with a solar cell that results in current leakage losses within the cell. An ideal solar cell would have zero series resistance and infinite large

shunt resistance. The effects of series resistance and shunt resistance on solar cell performance can be found in Figure 2-6 [13]. From the calculated results shown in the graph, the solar cell current-voltage (I-V) curve (*i.e.*, performance) is strongly affected by the series resistance while shunt resistance plays a less important role. The results show that the I-V curve changed significantly when the series resistance increased from 0 to 5Ω . Instead when the shunt resistance reduced from infinite large to 100Ω , there is no major change for the I-V curve. Thus series resistance is a dominating factor in determining the power available from a solar cell. The performance deterioration mainly comes from the rapid drop of fill factor (FF), a response of a slight increase of series resistance. Figure 2-7 shows how quickly an increasing series resistance affects the performance of a solar cell.

This result shows that it is critical to obtain a low series resistance, *i.e.*, to reduce the resistance of the internal material that constitutes the device. This is the motivation for the efforts to deposit transparent zinc oxide with extremely low resistivity, which is part of the work in the scope of this dissertation.

Solar Cells using Different Materials

Among the various materials that have been tested as absorber layer for PV devices, several are quite successful in their applications. Examples of them are crystalline silicon, amorphous silicon and a wide variety of compound semiconductors such as GaAs, InP, CuInSe₂ and CdTe. These materials can be generally divided into two categories based on their energy band structure. One is called direct band gap material and the other is referred to as indirect band gap material. For direct band gap materials, the maximum of the valence band energy and the minimum of the conduction band energy show at the same crystal momentum values. The indirect band gap material does not have this property. This band gap structure difference leads

to the fact that direct band gap materials have a much higher absorption coefficient than indirect materials. Consequently, for indirect band gap material such as crystalline silicon, it requires more thickness of the material and more critical preparation technique to produce a qualified absorber layer with reasonable efficiency. For example, a silicon film of thickness about 100 microns is required to absorb 95% of the photons in the solar spectrum [14] while for a direct band gap material, a film of less than 1 micron thickness is capable of absorbing more than 90% of the incident sunlight. Because of the large thickness of material required, the silicon film has to be ultra-high pure for the generated minority carriers to travel the large distance towards the junctions without being captured by defects. Single crystal silicon used in PV applications is usually fabricated by the Czochralski (CZ) process [15], which significantly elevates the fabrication costs. Nevertheless, silicon technology still dominates the current PV market as a mature technology. Figure 2-8 shows the technology market share in 2002 [16]. Some of the important PV materials are briefly introduced in the following sections.

Crystalline Silicon Solar Cells

Silicon is the most extensively studied semiconductor and was the first commercially used PV cell material. It is a cheap and abundant element that can be found in sand and other minerals. Silicon processing is very mature through the continuous development of integrated circuit processing technique since the 1950s. This provides great background theory and technical support to silicon solar cell research.

Single crystalline silicon

High purity single crystal silicon solar cells are the first commercially developed solar cells. Efficiency of single crystal silicon has been beyond 20% as early as in the 1980s [17]. Commercial single crystalline silicon cells usually have lower efficiency.

Major drawback of single crystalline silicon solar cells are the high cost and silicon supply problem. Silicon wafers need to be cut off from ingots produced by Czochralski (CZ) process, which is a costly method. As an indirect bandgap material, it requires thicker silicon consequently more amount of materials than thin films to build a high efficiency cell. About half of the cost of a silicon module comes from the cost of single crystal silicon wafers. With the high demanding form the semiconductor industry, price of silicon wafers remains high. The PV industry has in the past used rejected silicon from the semiconductor industry that was available at a lower cost. This creates a dependence on the source materials and restricts the development scale of this technology. The high material cost and processing cost together with the competition of wafer consumptions from the integration circuit industry led to the development of alternative solar cell materials.

Polycrystalline silicon

Polycrystalline silicon is typically produced by block casting and solidification of silicon[18], which avoids the costly pulling process used by the CZ method, resulting a process much more economic compared with the strict CZ process. Silicon is melted and poured into a square graphite crucible to create silicon blocks with a square shape, which yields better utilization of the wafer when later assembled into modules. With controlled cooling process, polycrystalline silicon block with a large crystal grain structure can be produced. The grain size can be obtained is about millimeters or centimeters. The silicon blocks are then sawn into wafers. A waste of about 50% of the silicon can happen during the process of sawing.

Polycrystalline silicon is not used in integration circuit industry and is only produced for fabrication solar cells. Although it typically has a lower solar cell efficiency, it is cheaper than single crystal silicon. Another advantage is that the square shaped wafers can easily be manufactured into square solar cells compared to round shaped pulled silicon crystals. Silicon

based PV technology is the most advanced and they share the largest percentage of the current market.

Thin Film Solar Cells

Materials used for thin film solar cells are direct band gap semiconductors with high absorption coefficients. With a thickness less than a few microns, they are able to absorb most of the incident sunlight. Because the film thickness is small, generated electron-hole pairs only need to travel a small distance to be gathered in the collector. The loss due to recombination is greatly reduced compared with crystalline silicon. Thus, the purity requirement is not as strict as that for silicon, which may lead to a significant drop for the manufacturing costs. Amorphous silicon, CdTe and CuInSe₂ (or its alloys) are three types of most promising material systems for thin film solar cells because of a good combination of reasonable efficiency, reliability and low production costs. The development history of these three thin film materials is shown in Figure 2-9.

Amorphous Silicon (a-Si:H) is the first thin-film material that has been commercially fabricated into photovoltaic cells and it holds the largest market share in thin film photovoltaic applications. It is also the most commercially developed thin film technology. CdTe and CIS technology have also been commercially developed recently. A brief introduction of amorphous Si and CIS technology is introduced next.

Amorphous silicon

Amorphous silicon is a disordered cousin of crystalline silicon. Although each silicon atom in amorphous Si has the same number of nearest neighbors as crystalline silicon, the bond angles connecting it to the neighbors are unequal. In stead of the 109° angles in crystalline silicon, the bond angles of a-Silicon are not constant. This disordered structure leads to a significant difference between amorphous Si and crystalline silicon. For example, instead of having an indirect band gap of 1.1eV (as for crystalline silicon), it has a direct band gap of about 1.75eV.

The average absorption coefficient of a-Silicon is much larger than that of single crystalline silicon over the visible light spectrum, which makes it possible to absorb the incident sunlight with a much smaller film thickness.

As stated before, a-Si has the most commercially advanced technology among all thin film materials. It is actually the only thin film material system that has an impact on the current PV market. But there is a major problem with a-Si solar cell system which holds back the development of reliable high efficiency a-Si modules. It is the performance degradation under illumination caused by light-induced photoconductivity degradation [19], a phenomenon known as Staebler-Wronski effect [20].

To improve the performance of a-Si solar cell, a critical technique called light trapping [21] is utilized to increase the light path length in a-Si, thus enhance the amount of photons to be absorbed. Transparent Conductive Oxide (TCO) plays a critical role in realizing light trapping. TCO can be deposited or post etched to form a rough surface with features serving as reflection mirrors. Light reaching these surface features can be scattered back into the device. By applying this technique appropriately, short circuit current can be significantly increased. Traditional TCOs like Indium Tin Oxide (ITO) and SnO_2 were originally applied to serve light trapping functions. But for superstrate structured a-Si solar cells, a-Si is typically deposited on top of TCO using PECVD (Plasma Enhanced CVD) process, during which the TCO is exposed to hydrogen plasma. It is found that the electrical conductivity and optical transmission of these traditional TCOs deteriorate when exposed to hydrogen plasma while ZnO as a new TCO material shows more resistance to hydrogen plasma [22].

Radio frequency magnetron sputtering can be used to deposit highly conductive and transparent ZnO:Al films to serve the light trapping purpose. But films grown by this technique

generally are smooth and do not have a light trapping structure. A wet etching process using hydrochloric acid is typically used to create surface roughness [23].

Amorphous Si based solar cells can be fabricated in two configurations: substrate and superstrate structure. Substrate type modules are built on stainless steel foil which has been first covered with a textured back reflector and superstrate structured devices are built on glass coated with TCOs. Tandem structured Si solar cells with a-Si as top cell are also fabricated to further increase the total conversion efficiency.

CuInSe₂ and CuGaSe₂

In the mid-1970s, a small group at Bell Laboratories in New Jersey began to work on several compound semiconductors for advanced photovoltaic applications. Among the materials studied, there was a category called chalcopyrite such as CuInSe₂ (CIS), CuGaSe₂ (CGS) and CuInS₂. They were successful to produce a single crystal CuInSe₂ based cell which reached 12% efficiency in 1975. This spurred the interest with the exploration of ternary and quaternary compound semiconductors on the application in photovoltaic field.

CIS is a direct band gap material and is the most light absorbing semiconductor known. The absorbance can be as high as 10^5 cm^{-1} . Half a micron of CIS is sufficient to absorb 90% of the incoming photons, making it possible to achieve high efficiency with much less material consumption than the silicon PV technology. Besides, this material system also possesses excellent stability and it is especially radiation hardness [24], which leads to a long life-time with consistent performance.

Figure 2-10 shows a typical CIGS solar cell structure. The typical substrate is glass. Flexible and light weight substrate such as metal foil can also be used. A thin layer of molybdenum is followed as the back contact. Then p-type CIGS compound is grown on top of Mo. After CIGS is a thin layer of cadmium sulfide (CdS) with n-type conductivity. Next to CdS

are the double transparent layers of intrinsic and doped ZnO. Optional MgF₂ antireflection layer can be evaporated on top of doped ZnO. Finally, it is nickel and aluminum dual metal layer serving as the top contact of the device, where nickel serves as a diffusion barrier between aluminum and zinc oxide.

CIS has a bandgap of 1.04 eV. This is smaller than the bandgap of silicon. Devices made out of CIS typically have a small open circuit voltage and a large short circuit current. This leads to a relatively large series resistance loss and compromise cell performance. Gallium can be added to increase the band gap of the compound and form an alloy typically referred to as CIGS. Sulfur can also be added to increase the band gap. High performance CIGS based devices generally require very high temperature to produce the absorber layer and the fundamental reason for that is not clear.

With a relatively large bandgap of 1.68 eV, ternary compound CGS is also a very interested material under investigation. Large bandgap CGS can be used as top cell for multi-junction solar cells (tandem cells) and it responds to the short wavelength part of the solar spectrum and allows long wavelength photos to pass through itself and reach the bottom cell. It is estimated that CGS/CIS tandem structure cells can reach efficiency beyond 30%. For CGS/CIGS tandem structure, modeling work predicted 25% conversion efficiency can be achieved [25].

Transparent Conductive Oxide

Because transparent electrode is an essential ingredient in most optical-electronic devices, extensive research has been done on both material selection and fabrication techniques. The most popular materials used to develop highly transparent and conductive thin films are n-type semiconductors consisting of metal oxides.

Transparent and electrically conductive films have been prepared from a wide variety of materials, including semi-conducting oxides of tin, indium, zinc and cadmium nitride [26], and they are commonly referred to as Transparent Conductive Oxide (TCO). Among these, the TCO thin films composed of binary compounds such as SnO₂ and In₂O₃ have been developed and doped SnO₂ (Sb or F doped SnO₂, *e.g.* SnO₂:Sb or SnO₂:F) and In₂O₃:Sn (indium tin oxide, ITO) are in practical use. In addition, ternary compounds such as Cd₂SnO₄, CdSnO₃ and CdIn₂O₄ have also been developed but have not yet been used widely [27]. One advantage of binary compound TCOs is that their chemical composition during the film deposition is relatively easier to control than that of ternary compounds and multi-component oxides. Typical undoped binary compound TCO films such as SnO₂, In₂O₃, ZnO, and CdO are n-type degenerate semiconductors, with electron concentrations of the order of 10²⁰ cm⁻³. To further lower the resistivity, doping materials are added into the films to enhance the free electron concentration. The lowest resistivity obtained is on the order of 10⁻⁵ Ω-cm, based on CdO:In films prepared for flat-panel displays. However, these were not practically used because of the toxicity of Cd. In practical films, the lowest resistivity comes from ITO films with a value of approximately 1×10⁻⁴ Ω-cm. Indium is an expensive material because the amount of Indium in nature is very small. There are no mines intentionally built to obtain indium simply because of the trivial amount available. In fact, indium is only obtained as a byproduct from mines for Zn and other metals. To obtain even lower resistivity than that of ITO and find an alternative to ITO, doped ZnO films were developed in the 1980s. Unlike In, Zn is an inexpensive, abundant and harmless material. Recently, ZnO:Al and ZnO:Ga doped thin films, with a resistivity of the order of 1×10⁻⁴ Ω-cm, have attracted much attention for deployment as the transparent electrode for thin film solar cells. It is believed that doped ZnO is a promising alternative to ITO.

Thin film ZnO has an energy bandgap greater than 3eV and can be deposited with high transparency. If heavily doped with Al or Ga, it can be very conductive as well. The high transparency allows the light to go through, reaching the absorber layer, where electron-hole pairs are generated. Highly doped conductive ZnO films easily form an ohmic contact with Al, which is essential for collecting the current generated from the cell.

Intensive research work on ZnO has been done for solar cell applications [28], organic light-emitting diodes [29-31] and transistors [32-34]. Thin films of zinc oxide can be prepared using various techniques such as spray pyrolysis [35-37], evaporation [38-40], chemical vapor deposition (CVD) [41-43], and sputtering [44-46]. The sputtering technique can produce as-deposited, highly conductive ZnO films without any post deposition treatment. Key advantages of sputtering are discussed in the next section.

Sputter Deposition

Introduction

Sputter deposition of films, which is often referred to as sputtering, was first reported by Wright in 1877. Edison patented a sputtering deposition processes to deposit silver on wax photograph cylinders in 1904[47].

Sputter deposition is a physical vaporization of atoms from a surface by momentum transfer from bombarding energetic particles, which generally are ions generated from a glow discharge or a plasma process. The ions developed in the plasma are accelerated in an electric field and bombard a target, which is the source of the deposited material. After ion impact, the eroded material then condenses from the gas phase onto the substrate where the film is grown. To attract the positive ions, the target is applied a negative electric field. Therefore the sputter deposition source is also referred to as the cathode.

Sputter deposition can be used deposit films of either element or compound material. When sputtering a compound thin film, the target can be either compound or elemental. In the later case, a reactive gas is incorporated in the sputtering gas and the compound is formed during the sputtering process. In some cases, sputtering a compound target can result a loss of some of the more volatile material (such as oxygen from ZnO) and the stoichiometry of the film may be different from that of the target. By adjusting the deposition parameters or add the volatile component into the sputtering gas to compensate the loss, resulted films can reach a desired stoichiometry, which is important for transparent conductive zinc oxide.

Advantages of Sputter Deposition

Sputter deposition is a flexible thin film growth process. It can be done under different vacuum conditions varying from below 10^{-5} Torr up to approximately 50mTorr. High vacuum sputter deposition using ion beams can reduce the damage of substrate from the plasma environment. Sputter deposition can deposit films of element, alloy and compound from either conductive or insulating target. There are also some of other advantages can be achieved through sputter deposition.

One of the major differences between sputtering as a plasma process and thermally excited thin-film preparation methods such as evaporation, chemical vapor deposition is the much higher energy input into the growing film. The relatively high kinetic energy of the adatoms with values of a few electron voltage can be achieved in contrast to around 100 meV for evaporation process. The high kinetic energy increases the thermal surface mobility of the adatoms, allowing more rearrangement of the atoms on the surface, consequently yielding improved film properties.

The target is generally cooled and the energy of ejected particles comes from momentum transfer form the bombarding ions. The cold surface presents little radiant heating to the vacuum system, which is an advantage over evaporation, where radiant heating can be significant,

especially in the case of long period intensive evaporation. The small amount of heating makes sputter deposition an appropriate process to deposit films on heat sensitive substrates.

The sputtering target can provide a stable, large area, solid vaporization source. Because the vaporization comes from a solid surface, the sputter geometry can be up, down or sideways, in contrast to evaporation from a melted source inside a crucible.

Sputter Deposition of ZnO

Thin film ZnO can be produced with different sputtering techniques such as radio frequency sputtering, direct current reactive sputtering and middle frequency reactive sputtering. The properties of sputtered ZnO films are dependent on many factors. Comprehensive studies on parameters such as deposition power, working pressure, substrate temperature, oxygen concentration, and target doping concentration have been carried on [48,49]. Individual parameters such as RF power [50], target to substrate distance [51] are also investigated. Although the research on sputtered ZnO is extensive, the reports from different authors are quite different. It seems that the optimum operation condition is equipment specific and there is not a universal recipe that guarantees ZnO films with good electrical and optical properties. Therefore, it is essential to determine the optimum parameter set for the UF oxide sputtering system.

Sputtered ZnO thin films have been successfully used for various optoelectronic devices such as organic light emitting diodes (OLED) and solar cells. Particularly for thin film solar cells, ZnO works well for different absorber materials such as CdTe [52], a-Si [53], CIGS [54]. There is also effort made to reduce the visible and particularly near-infrared optical absorption of ZnO films to further improve the performance of solar cells [55].

Recently, producing p-type ZnO has been a popular research area due to the interest in fabricating homojunction wide bandgap ZnO devices for optoelectronic applications. Sputtering

has been successfully demonstrated to produce p-type ZnO [56]. The thermal stability of p-type ZnO needs to be improved for reliable applications.

Summary

Thin film ZnO has broad applications in optoelectronic devices including light emitting diodes, lasers and solar cells. Sputter deposition is an effective method in producing n-type ZnO. The optical and electrical properties of sputtered ZnO can be affected by various deposition parameters. An optimization of the sputtering condition is necessary to produce highly conductive yet transparent ZnO films that are required for photovoltaic applications.

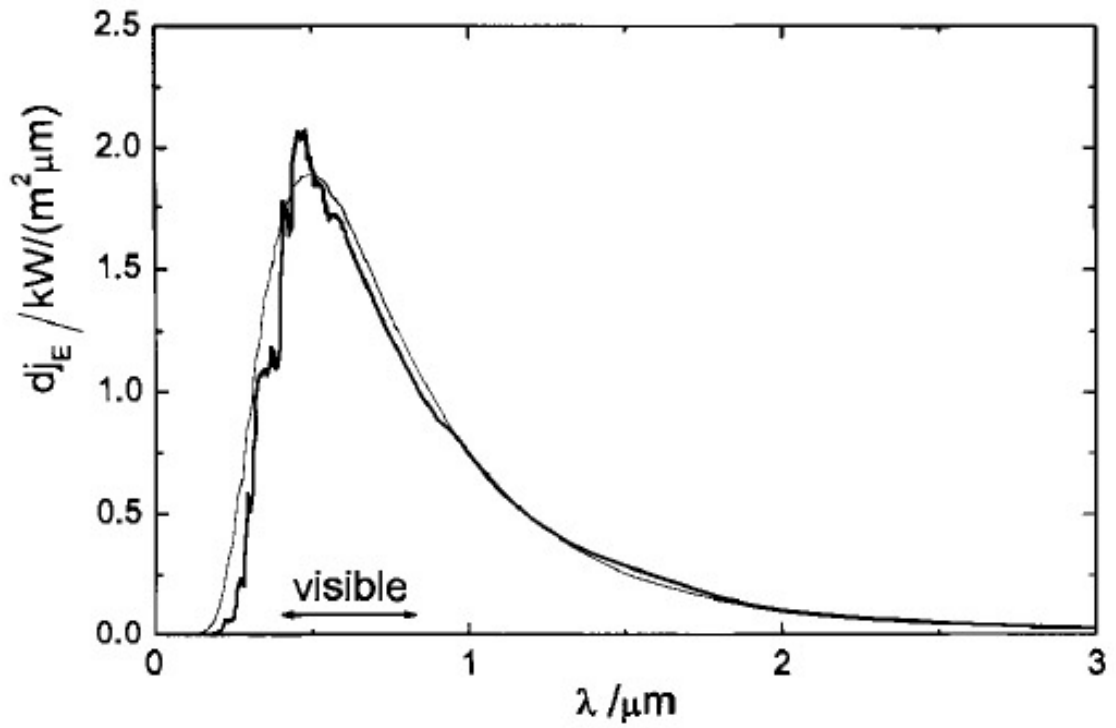


Figure 2-1. Energy current density per wavelength of AM0 spectrum (heavy line) compared with blackbody radiation at 5800K (thin line).

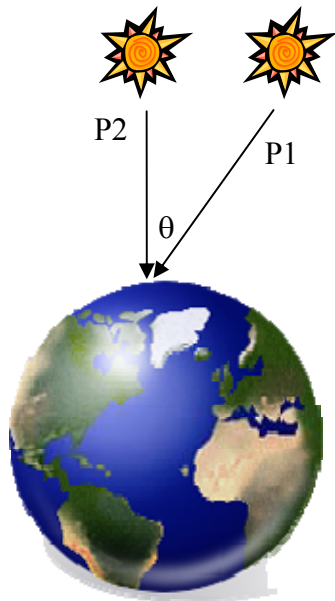


Figure 2-2. Schematic of the Air Mass definition.

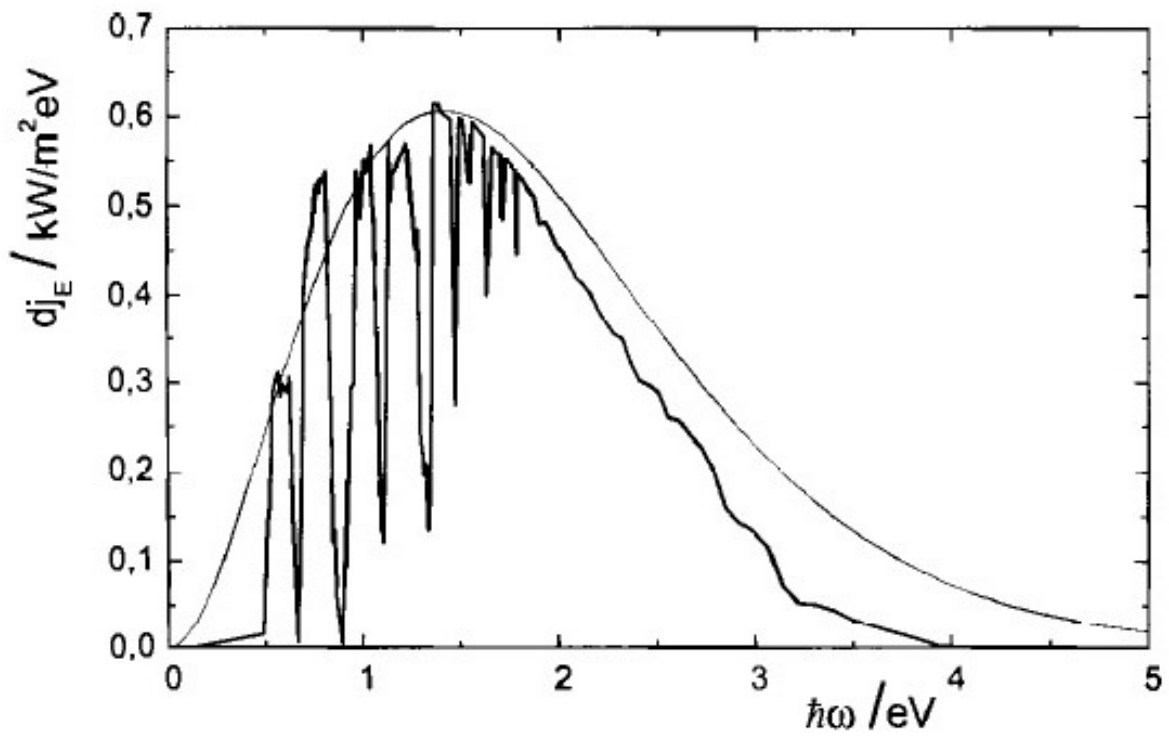


Figure 2-3. Energy current density per photon energy of AM1.5 spectrum (heavy line) compared with blackbody radiation at 5800K (thin line).

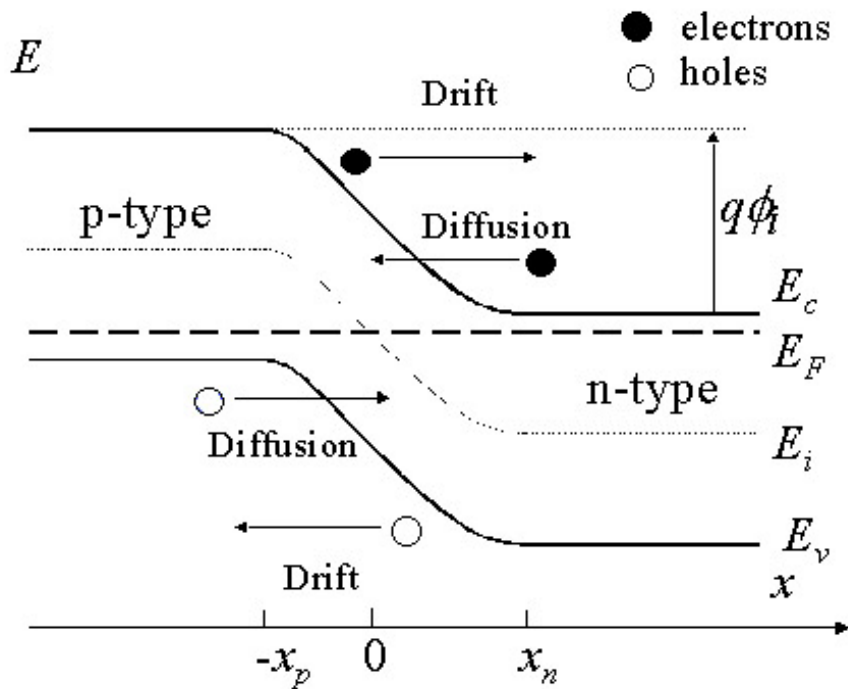


Figure 2-4. Formation of built-in potential between p-n junction.

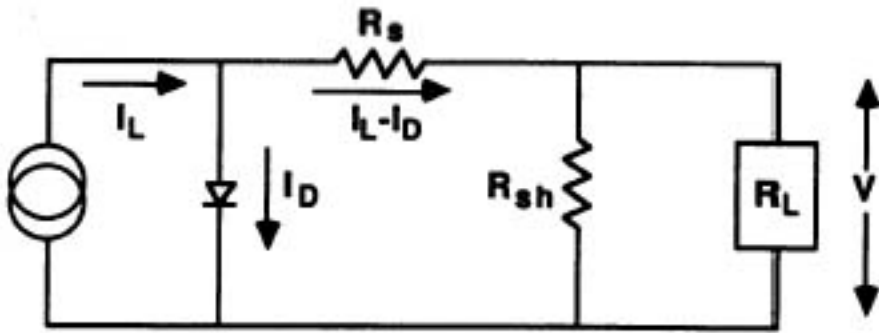


Figure 2-5. An equivalent circuit of a typical solar cell.

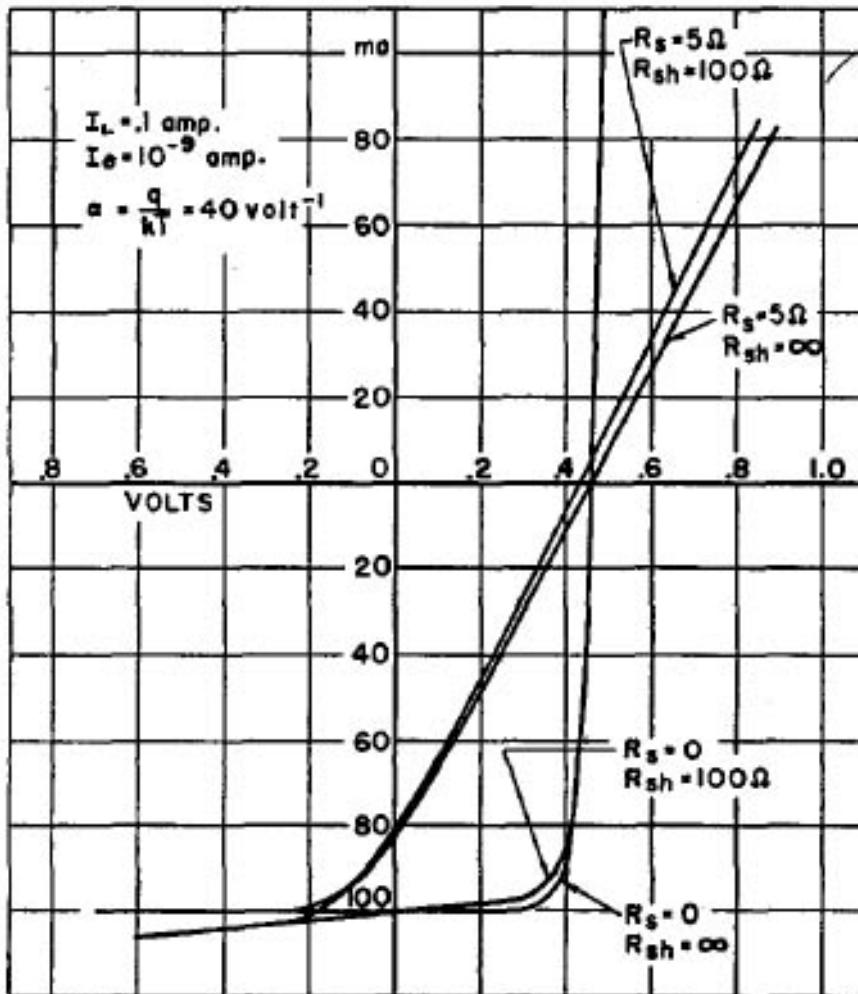
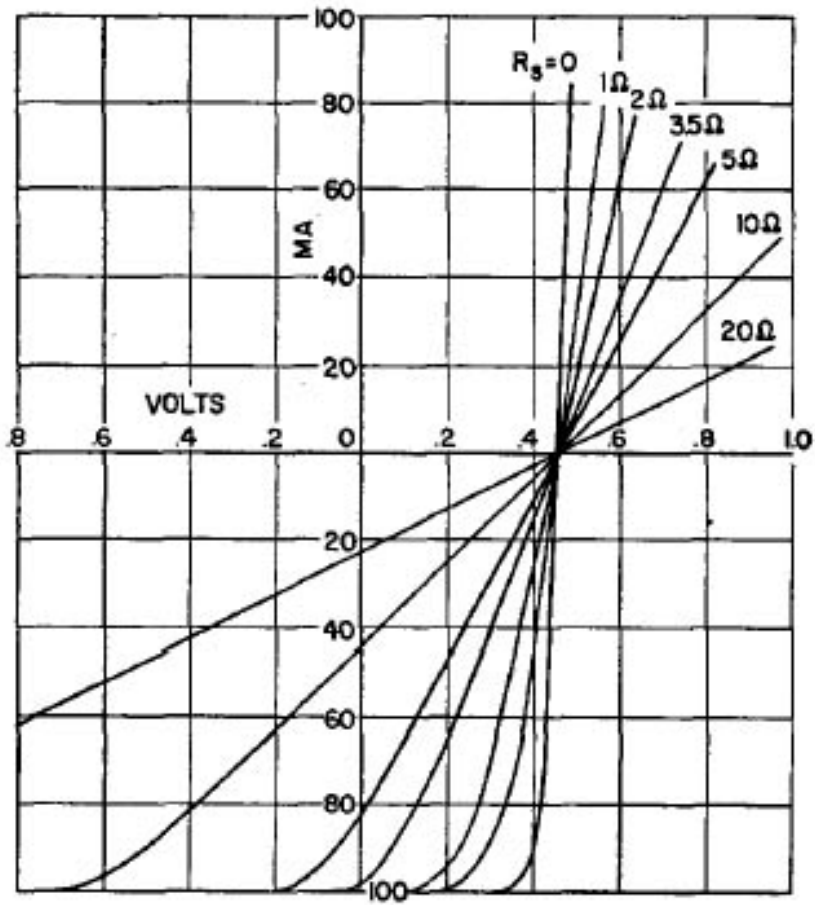
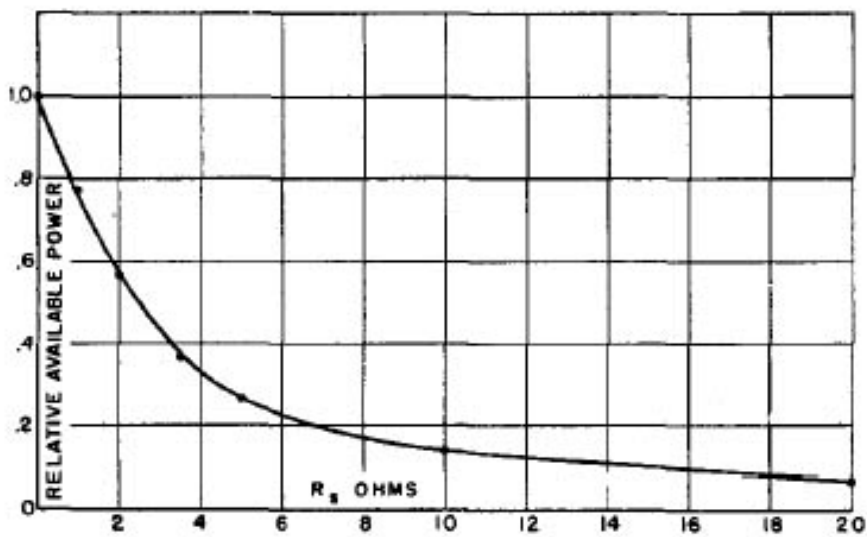


Figure 2-6. Effect of series resistance and shunt resistance on solar cell performance.



(a)



(b)

Figure 2-7. Effect of series resistance on solar cell performance.

World Market 2002 by Technology

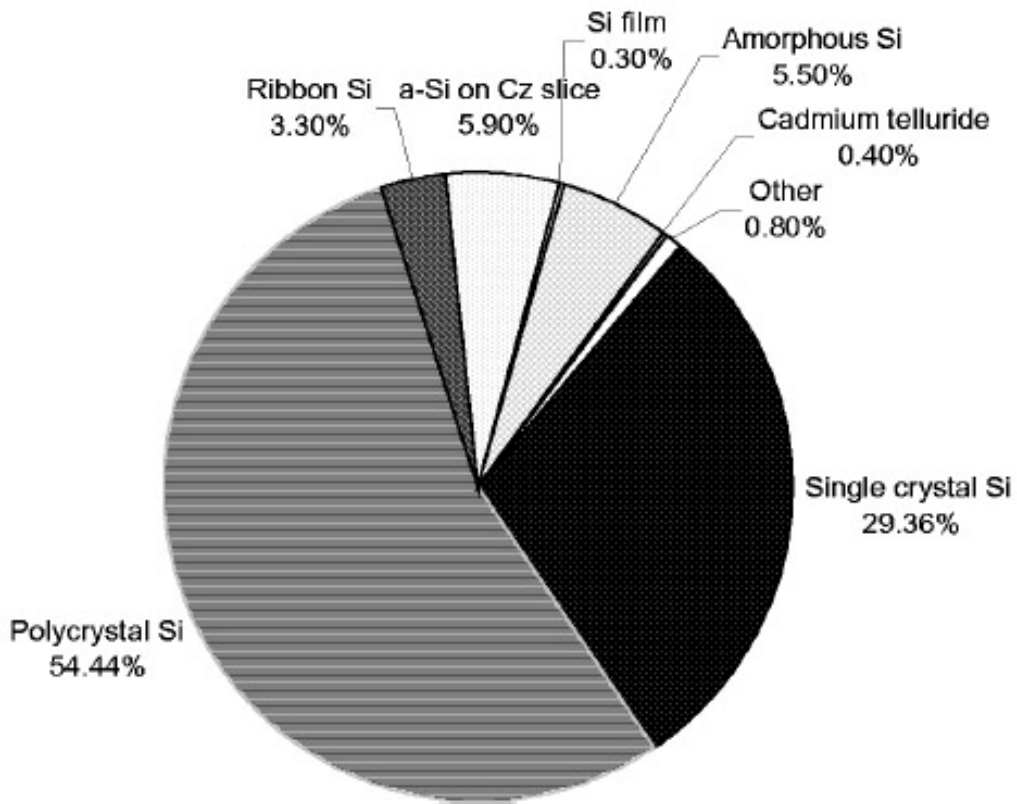


Figure 2-8. World PV market share by technology in 2002.

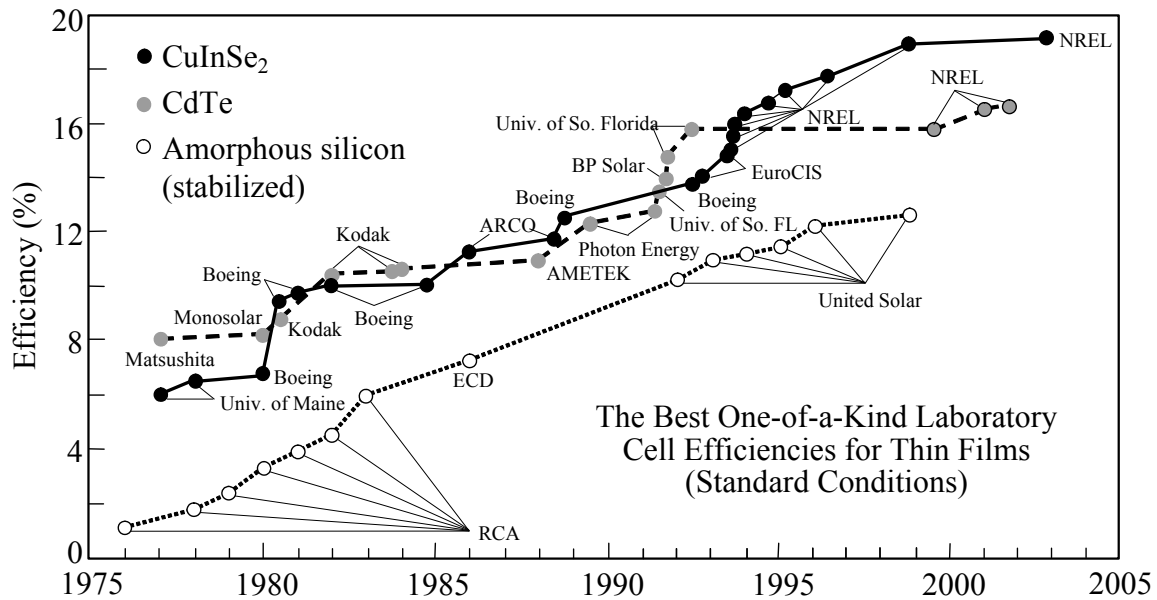


Figure 2-9. Development history of thin film solar cells. (Courtesy of NREL)

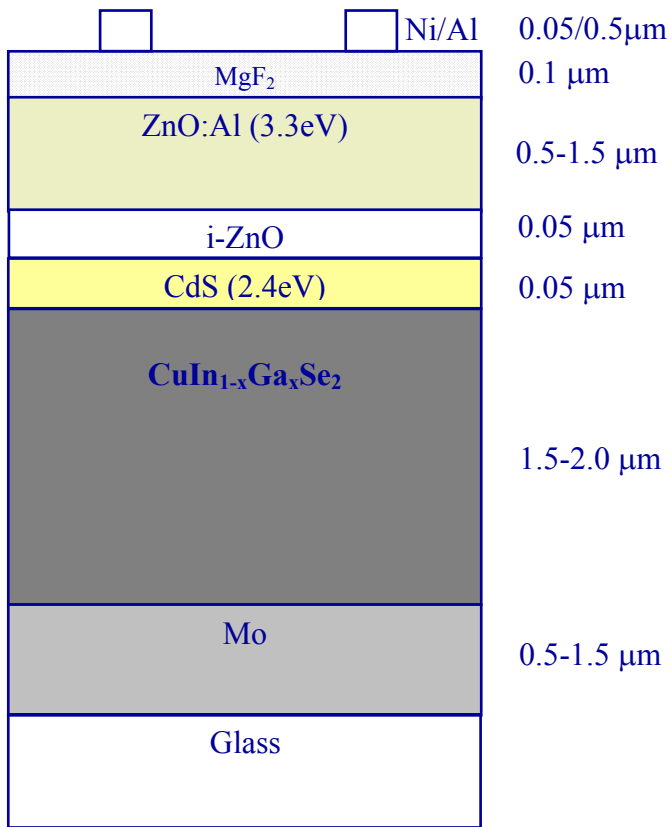


Figure 2-10. Thin film CIGS solar cell structure

CHAPTER 3 EXPERIMENTAL METHODS

ZnO Sputtering System

Sputter deposition was adopted as a room temperature process which could keep the pre-deposited CIS and CdS layers from being destroyed by high temperatures. The equipment used for ZnO sputtering is a Perkin-Elmer 4400 industry sputtering system. A photo and schematic of the equipment are shown in Figure 3-1 and Figure 3-2, respectively. It is equipped with a stainless steel, load-locked vacuum system to generate the vacuum required for sputter deposition. Typical base pressure of the system is approximately 6×10^{-7} Torr. However, it requires long period of pumping to reach this pressure due to the large size and surface area of the substrate transfer pallet.

The system originally has three RF planar sources, each handling an 8 inch target in a sputter down geometry. Targets currently being used are Mo, ZnO:Al₂O₃ (98wt%:2wt%) and Zn. An 8 inch diameter magnetron was later added on top of the ZnO:Al₂O₃ target to confine electrons close to the target and increase the sputter rate. Uniformity shields are integrated 1.6 cm below each target to compensate the short exposure time of substrates placed at large radial distance due to the higher angular velocity when rotating. These shields modify the flux rate from the target (blocking flux in small radial distance areas) to account for the different exposure time along the radial direction of the platen, thus generate a uniform film when the platen is rotated. Because the plasma distribution for magnetron sputtering and diode sputtering is different, the shape of the uniformity shields for the two cases are different. These uniformity shields are removed for experiments without substrate motion.

The sources and the substrate table are cooled by chilled water. The substrate platen has rotary motion capabilities, allowing deposition of uniform films on up to fourteen 4 inch wafers

in a single batch process. The motion system for the substrate platen is controlled with a stepping motor, which gives accurate control of the substrate motion. It can generate full rotation in either clockwise or counter clockwise direction at precise speed and acceleration, designated number of oscillations about a region below the target. Although these capabilities can be of utility for complicated procedures, accurate positioning of the substrates below the sources are the primary uses for the motion system. Generally motion on the substrate platen is not adapted during deposition to avoid generating particles, which could contaminate the vacuum environment. The throw or substrate to target distance can be set between 5 and 9 cm.

The RF power is supplied by a Randex 2kW RF generator which provides a radio frequency of 13.56 MHz. This power is delivered to the target through an impedance matching network. There is a switch available to route the power generated by the single generator to the appropriate source, or to the substrate table when sputter etching is used to clean or modify the substrate.

A CTI CryoTorr 8 cryopump and a Leybold Trivac 60cfm rotary vane pump provide the high vacuum and rough pumping, respectively. A throttle valve between the cryopump and the deposition chamber reduces the pump's effective pumping speed by up to a factor of 50 when engaged. Two mass flow controllers (MFCs) are used to regulate introduction of Ar and O₂ gas, and are used in conjunction with the throttling valve to generate a controlled gas ambient over the pressure range of 2-150 mTorr, a range typical for sputter deposition. Both MFCs have a range of 0-100 standard cubic centimeters per minute (SCCM), and control gases from ultrahigh purity gas bottles. The system operates at a typical base pressure of 6×10^{-7} Torr. Vacuum gauging is provided by an array of two Bayard-Alpert ionization gauges, two Convectron gauges, three thermocouple gauges, and one MKS Baratron capacitance manometer. The

Bayard-Alpert gauges are used for measurements at high vacuum conditions ($<10^{-5}$ Torr), and are therefore used to determine the base pressure of the system. The base pressure is a critical factor in controlling contamination in the growing film. The other critical gauge is the MKS Baratron gauge, which gives accurate, precise, fast, and direct measurement of the pressure for the range of 10^{-5} to 1 Torr, and therefore spans the pressure range used for sputter deposition. A direct gauge refers to the fact that the gauge measures the gas pressure directly, instead of using heat transfer rate to determine the ambient pressure. A direct gauge's calibration is therefore independent of the gas being measured. This is critical for generating ambient with controlled partial pressures of a multiple gas species.

Substrate Cleaning

ZnO thin films were deposited on 1mm thick soda-lime glass substrates for characterization purpose. The substrates are first rinsed in sprays of deionized (DI) water to remove any major contaminations attached on the surface. They are then vertically placed in a Teflon substrate holder. The substrate holder is then put in a hot DI water bath at approximately 80°C for 10 minutes with all glass substrates completely immersed in the bath. The substrates are then taken out and dipped in DI water dissolved with Alconox detergent. They are then individually taken out of the holder and physically scrubbed with a clean brush and then put back in the holder. Both the sides and edges are cleaned to remove all possible contaminations. The substrates are rinsed again in sprays of DI water and put in a second hot DI water bath in an ultrasonic cleaner. All substrates are completely immersed in the bath and the ultrasonic cleaning takes about 10 minutes. The holder are then removed from the ultrasonic cleaner and placed in a three stage cascade rinsers agitated with nitrogen bubbles. Finally the substrates are individually dried with nitrogen gun and placed in storage boxes.

For CIS device fabrication, the soda-lime glass substrates coated with Mo, CIS, CdS are stored in vacuum sealed bags to prevent possible oxidation from air. The bags are only opened before the ZnO deposition and the substrates are quickly put into the vacuum chamber after they are exposed in air.

Characterization Techniques

To fully understand the various aspects of semiconductor property, a number of material characterization techniques are utilized. The electrical, optical and other properties are comprehensively investigated using the following techniques.

Electrical Property Characterization

Electrical property characterization includes four-point probe measurement to acquire the sheet resistance of the thin film and Hall measurement to obtain carrier type, concentration and mobility information.

Four-point probe

The four-point probe contains four thin collinearly placed tungsten wires probes which are made to contact the sample under test. In a configuration shown in Figure 3-3, a constant current I flows between the outer probes, and the voltage V is measured between the two inner probes, ideally without drawing any current.

The equipment used was an Alessi four point probe. It has a probe head with tungsten carbide tips with a point radius of 0.002", a probe space of 0.05". Current supplier was a Crytronics model 120 current source which can provide currents from 1 μ A to 100mA. Voltage was measured with a Keithley model 181 nanovolt electrometer. Sheet resistance with units of Ω /square, can be obtained from the four-point probe using the equation

$$R_s = \frac{4.532V}{I} \quad (3.1)$$

where V and I are voltage and current respectively and 4.532 is the geometric factor when the size of the thin film is much larger than the probe spacings. Resistivity ρ with units of $\Omega\cdot\text{cm}$ can be obtained by multiplying the thickness of the film by R_s , shown in the following equation

$$\rho = R_s t = \frac{4.532Vt}{I} \quad (3.2)$$

Hall measurement

Hall measurement is used to obtain the resistivity, carrier mobility and concentration information of zinc oxide thin film. The physical theory behind this characterization technique is the Hall effect. When electric current flows in the presence of a perpendicular applied magnetic field, the Lorentz force deflects the moving charge carriers to one side of the sample and generates an electric field perpendicular to both the current and the applied magnetic field. This is called the Hall effect. The Hall coefficient is the ratio of the perpendicular electric field to the product of current density and magnetic field, while the resistivity is the ratio of the parallel electric field to the current density.

A Lakeshore 7507 Hall system was used to conduct the Hall measurement. The samples were cleaved into squares with dimension $1\text{cm}\times 1\text{cm}$. They are mounted on Lakeshore Hall sample mount (Part number 671-201) using double stick tape. Care was taken to make sure the sample surface is in parallel to the sample surface. Lakeshore Hall sample wires (Part number 671-260) are used for connection between the contact spots on the sample mount and the corners of the sample. The wires are soldered with small amount of indium which forms Ohmic contact with the zinc oxide thin film.

Square shaped van der Pauw geometry is used, which is shown in Figure 3-4. In this geometry, the contacts are on the circumference of the sample and the dimension of the contacts

is made as small as possible. For the square van der Pauw geometry, the estimated correction factor for resistivity can be shown in the following equation[57]

$$\frac{\Delta\rho}{\rho} = \left(\frac{c}{a}\right)^2 \quad (3.3)$$

where c is the dimension of the contact spot and a is the length of the Hall sample. Efforts were made to ensure the dimension of the contact spot as small as 1 mm. Therefore, a good accuracy of the resistivity can be achieved.

Before conducting the variable field Hall measurement, a forward and reverse I-V curve measurement is always conducted to verify the Ohmic property of all of the four contacts spots.

Optical Spectrophotometer Characterization

The optical transmission data was measured from the UV region to near IR region using a Perkin-Elmer Lambda 900 spectrophotometer. The system is equipped with a monochromator and a chopper, which is used to generate a sample and a reference beam. For all the measurements, the reference beam path was left open. Background correction leaving both the reference and sample beam path open is always performed before taking the transmission data.

The samples are cleaned with acetone to remove possible contaminations such as fingerprints and dust particles, which may cause scattering of the incident light. All transmission data was taken between 300nm and 900nm using the normal incidence setup.

When an incident light with intensity I_0 enters the sample, the absorption process can be expressed as

$$I = I_0 e^{-A} = I_0 e^{-\alpha d} \quad (3.4)$$

where I is the remaining intensity and A is the absorbance, which is the product of the absorption coefficient α and the sample thickness d . The transmission T is defined as

$$T = \frac{I}{I_0} = e^{-A} = e^{-\alpha d} \quad (3.5)$$

The absorption coefficient α can be estimated by measuring the transmission of two samples with different thickness d_1 and d_2 . Then the absorption coefficient is derived using the equation

$$\alpha = \ln\left(\frac{T_1}{T_2}\right)/(d_2 - d_1) \quad (3.6)$$

where T_1 and T_2 are the transmission of sample 1 and sample 2 respectively.

Other Characterizations

Profilometry, X-ray diffraction, atomic force microscopy and Auger electron spectroscopy are used to characterize various material properties for sputtered zinc oxide thin films.

Profilometry

Because sputtering is a reproducible process, the growth rate can generally be maintained at a repeatable rate by using identical sputtering conditions. Therefore, there is no *in-situ* film thickness monitor set up in the UF zinc oxide sputtering system. The film thickness is determined using profilometer after the deposition and the growth rate is calculated. With growth rate obtained from previous runs, the film thickness can be controlled by choosing appropriate deposition duration.

A Tencor P2-long scan profilometer was used to measure the thickness. Profilometer is a measurement device that probes the sample surface by a sweeping stylus. The vertical movement of the stylus is recorded when it runs over the sample surface. This gives the height of the surface as a function of location.

To measure the thickness of the deposited films, a trench step needs to be created on the surface of the sample. Generally, two methods were utilized to create the step. The first method

is to cover part of the substrate before deposition and remove the cover later. A portion of the substrate was either masked with permanent marker or covered with a scotch tape. After the deposition, the marker was removed with acetone and a swab or the tape was simply removed by hand, which effectively removed the deposited film on top, yielding a well defined trench step. The second method to create the step is etching. The film area to be preserved are covered with tape and the unwanted area are exposed on top of a beaker containing aqua regia. The solution is heated to 50°C and the vapor etches away the oxide creating the step. The profilometer was then used to measure the height of the step, and therefore the film thickness.

X-Ray Diffraction

X-ray is the generic term used to describe electromagnetic radiation with wavelengths between roughly 0.01 nm and 10 nm. This is shorter than ultraviolet but longer than gamma radiation. The spacing of adjacent atoms in a crystal structure is typically about 0.3 nm. The wavelengths of X-rays are therefore of the same order of magnitude as the atomic spacing in a crystal.

X-rays are generated by accelerating electrons toward an anode target under vacuum conditions. The high-energy incident electrons interact with the target atoms and knock out some of the core electrons. Then the outer shell electrons fill in the holes left through relaxation process and the energy difference is released generating X-ray to conserve the energy. The energy or wavelength of the radiated X-ray is determined by the energy difference between the two electrons and is not related with the acceleration energy of the incident electrons. The Cu $K\alpha$ radiations are widely used in X-ray diffractometers. It is generated via transition between the Cu L shell electrons and K shell electrons. The intensity ratio between $K\alpha_1$ and $K\alpha_2$ radiation is 2:1. Figure 3-5 shows the schematic how Cu $K\alpha$ radiations are generated. Other

series of X-rays such as $K\beta$ and L series are generated at the same time. But they are filtered away and only the $K\alpha_1$ and $K\alpha_2$ are used to generate the diffraction pattern. The wavelengths of these two radiations are very close and the peaks are overlapped especially at the low 2θ angle. There are X-ray pattern processing software having the capabilities of stripping off the $K\alpha_2$ diffraction pattern allowing more accurate evaluation of the data.

X-Ray Diffraction (XRD) can generally be categorized as single crystal XRD and powder XRD. Single crystal XRD examines a single crystal whose unit cells are perfectly aligned. It requires careful orientation of the sample in order to obtain the diffraction pattern. X-ray powder diffraction is more widely used and the general term “X-ray diffraction” refers to the powder diffraction unless specified otherwise. The samples used for powder diffraction can be either powders or thin film samples. The diffraction geometry tells that only the crystallites with planes in parallel to the specimen surface will contribute to the diffraction intensity. An ideal powder sample consists of a collection of small crystallites randomly distributed with all available orientations contributing to the diffraction pattern. The diffraction pattern is a fingerprint of a specific crystalline substance (phase) and the International Center of Diffraction Data (ICDD, formerly known as JCPDS) maintains a diffraction pattern database of various minerals, inorganic and organic standards. By comparing the diffraction pattern of an unknown sample with the data of standards, the possible phases available in the unknown may be identified. It is noteworthy that XRD is a technique for phase identification. In most cases, it is still necessary to know the chemical compositions of the sample to accurately identify the phases in exist. For thin film samples, the peak intensity can vary significantly from the standards due to preferred orientation. Besides phase identification, careful examination of the peak broadening can be used to estimate grain size and stress associated with the sample. Finally,

quantitative analysis of the diffraction pattern can be used to estimate the ratio between different phases in a specimen.

The Bragg's law is the cornerstone of X-ray diffraction analysis. The relation was discovered in 1912 by W. L. Bragg. Bragg law describes the condition that the scattered rays from two parallel planes interact with each other in such a way as to create constructive interference.

As shown in Figure 3-6, the extra distance that ray B must travel is the distance X-Y-Z. Thus $X-Y-Z = n\lambda$ to create constructive interference. Notice that $X-Y = Y-Z = d \sin\theta$. Hence, the Bragg's law can be expressed with the equation

$$\lambda = 2d_{hkl} \sin\theta_{hkl} \quad (3.7)$$

where 2θ is the diffraction angle, which is the angle between the incident and diffracted x rays. In a typical experiment, the diffracted intensity is measured as a function of 2θ and the orientation of the specimen, which yields the diffraction pattern.

Atomic Force Microscopy

Atomic Force Microscopy (AFM) and Scanning Tunneling Microscopy (STM) are two forms of Scanning Probe Microscopy (SPM), a technique that can reveal information down to atomic scale by using a sharp probe to scan across the surface of a sample. It is relatively new techniques developed in 1980s.

Depending on the different operational conditions of the probe during scanning, there are three operation modes for AFM, namely contact mode, tapping mode and non-contact mode. During contact mode measurement, a tip mounted at the end of a cantilever scans across the sample while contacting the surface. The deflection of the cantilever is monitored using a laser shining on the tip and redirect the laser to a split photodiode, which measures the signal variation

coming from the vertical movement of the cantilever. A feedback control loop maintains a constant deflection of the cantilever by adjusting the vertical position of either the piezoelectric scanner or the sample. This position change is monitored and converted to the surface morphology of the sample. In tapping mode, the cantilever oscillates at or slightly below its resonance frequency at a position very close to the sample surface. Instead of direct contacting the sample surface, the tip only taps on the sample surface. The root mean square (RMS) of the oscillation signal is maintained by the feedback control loop by adjusting the positions of the scanner of the sample and the position change is converted to morphology. For non-contact mode, the tip oscillates close to the surface but never touches the sample surface. The oscillation amplitude and frequency will be changed by the van der Waals force, which extends a few nanometers above the sample surface. The feedback control loop maintains a constant oscillation amplitude and frequency by vertically moving the scanners and this movement is converted to surface morphology.

Contact mode AFM has high scan speed and good resolution, but the lateral forces exert on the sample surface may damage soft samples. Non-contact mode AFM exerts little force on the sample surface and is not likely to scrap the sample, but the scan speed is low and the sample should be extremely hydrophobic to prevent the tip from getting stuck by the adsorbed fluid layer on the sample surface. Tapping mode AFM has less surface damage than contract mode AFM and can be used on most samples comparing to non-contact mode AFM. The AFM images shown in this dissertation were obtained using a Veeco Dimension 3100 AFM operated under tapping mode AFM. The tips used are tapping mode etched single crystal silicon probes produced by Veeco.

Auger Electron Spectroscopy

Auger electron spectroscopy (AES) is a technique that can identify chemical composition information by analyzing the characteristic energy of Auger electrons from an element. Auger electron spectroscopy has been primarily used to determine the chemical compositions of materials, but it is being increasingly used to characterize chemical state properties. [58] It is applied to sputtered ZnO thin film characterization to evaluate the composition of the film and detect any possible contaminations.

When a core level electron is removed leaving a vacancy, electrons from higher energy level can relax and fall into the left vacancy. The energy difference between these two energy levels is released to balance the total energy. This released energy can be transferred to a third electron, which is excited and escape from the atom. The third electron is called Auger electron. Auger electrons have characteristic energy relating to the energy difference between involved energy levels. Three electrons are involved to generate an Auger electron. Therefore, AES can only analyze materials whose atoms have at least three electrons. Hydrogen and Helium are not detectable using AES and Lithium is material having the least atomic number required for AES analysis.

AES is a surface sensitive analytical technique because Auger electrons have low energy and they can only escape from areas a few atomic layers under the surface. Nevertheless, combined with ion-beam sputtering, which removes material from the surface, this technique can provide depth information. Depth profile data was taken by alternating between sputter etching the sample and collecting small windows of Auger spectra focused on the peaks for elements of interest.

A PHI model 660 Scanning Auger Microprobe (SAM) was used in this work. It has a LaB₆ filament as the thermionic emission electron source. A cylindrical mirror analyzer (CMA)

is used to analyze the kinetic energy of the secondary and Auger electrons. The system is equipped with an ion pump and normally operates at a base pressure of about 3×10^{-10} Torr. An Ar ion gun is equipped to sputter off material from the samples for the purpose of either cleaning the sample surface or depth profiling. During the sputtering process, the system typically works under a pressure in the range of middle 10^{-8} Torr.



Figure 3-1. Perkin-Elmer 4400 sputtering system.

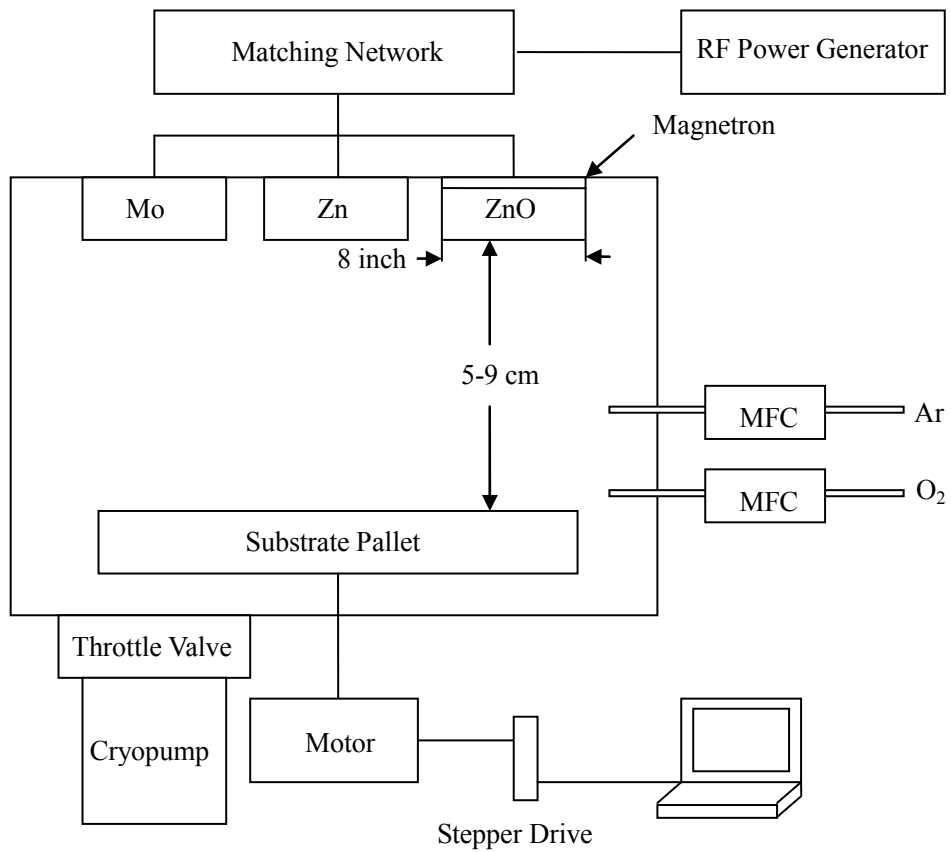


Figure 3-2. Schematic of the ZnO Sputtering System (Perkin-Elmer 4400).

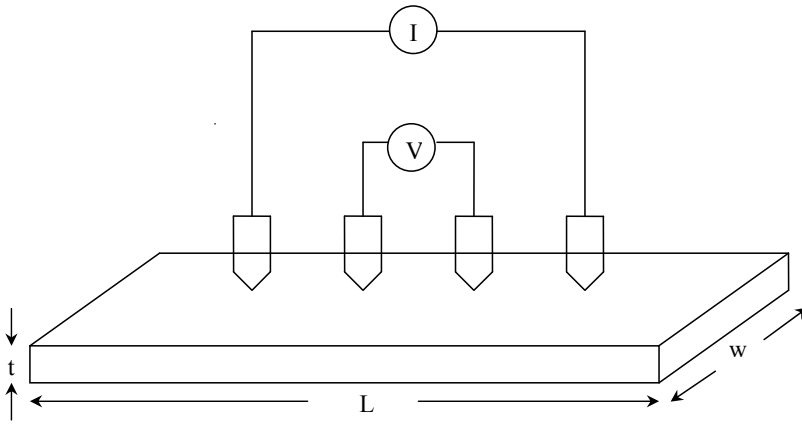


Figure 3-3. Schematics of four-point probe measurement.

⊙ B (oriented out of the page)

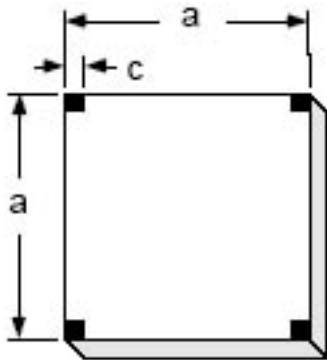


Figure 3-4. Square shaped van der Pauw sample geometry.

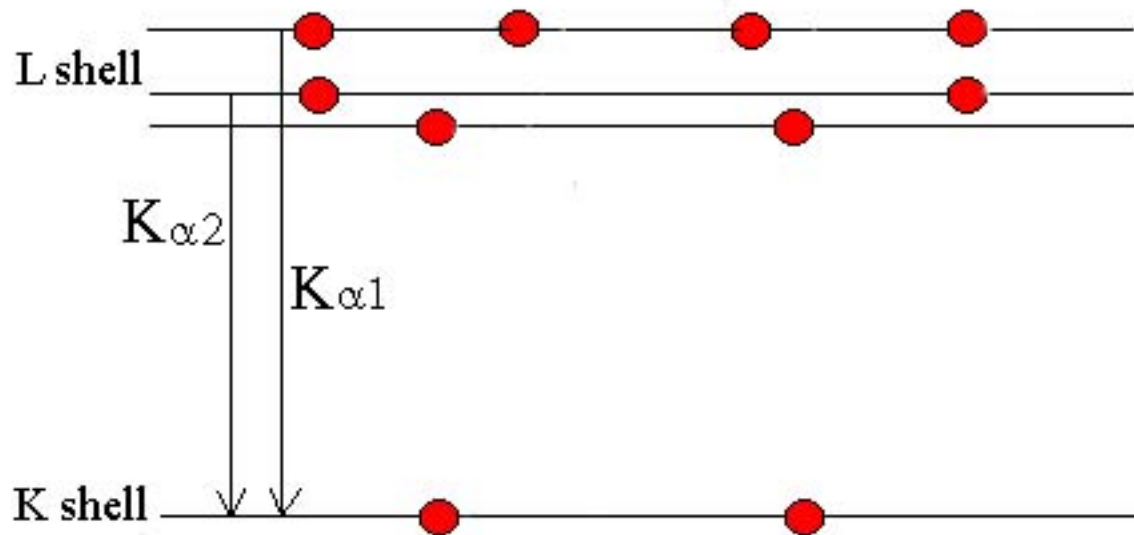


Figure 3-5. Generation of Cu K_{α} radiation.

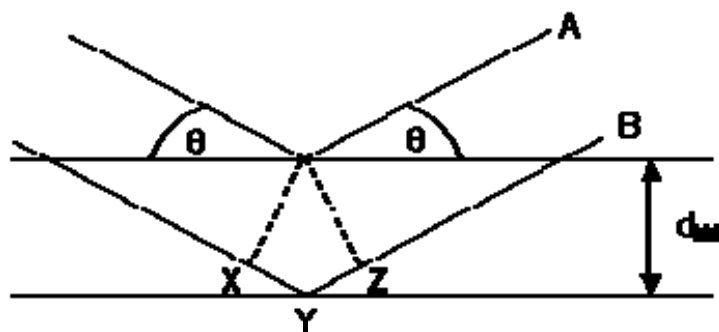


Figure 3-6. Bragg's condition.

CHAPTER 4
GROWTH AND CHARACTERIZATION OF ZINC OXIDE

Optimization of Sputter Deposition of Aluminum Doped ZnO

The optical and electrical properties of Al doped ZnO (AZO) can be affected by various deposition parameters such as base pressure, working pressure and deposition power. Films obtained under different deposition conditions are routinely characterized with four-point probe and profilometry to obtain the resistivity value. Various other techniques such as X-ray diffraction, atomic force microscope, Hall measurement and Auger electron spectroscopy are employed to further characterize these thin films. The results will be presented in this chapter.

Experiments at Different Base Pressures

Due to the large surface area of the substrate platen, it requires a long period of time for outgassing. The starting base pressure can vary over a large range depending on the pumping time. An investigation which extends the base pressure between 6.0×10^{-7} Torr and 2×10^{-6} Torr is carried out. The base pressures are categorized into three regions to better illustrate the obtained results, namely the low, medium and high base pressure region. The low base pressures represent approximately 6×10^{-7} Torr, obtained by adopting a very long period (typically greater than 24 hours) of pumping of the sputtering chamber before starting the deposition. This ensures that a minimum amount of residual water vapor is present during the sputtering process. The medium base pressure, approximately 9×10^{-7} Torr, is associated with a shorter pumping period, under conditions that the chamber's pressure still continues to drop when the deposition process starts. In this case, the pumping and outgassing have not reached equilibrium at the beginning of the deposition, and as a consequence the amount of water vapor present in the chamber is larger than in the low base-pressure region. Finally, the high base-pressure condition, approximately 2×10^{-6} Torr, is obtained after a short pumping period, and as a consequence the amount of

residual water vapor is relatively large. All of these three base pressure regions ensure a reasonable clean environment for the sputter-deposition process.

Optical property

The optical transmission of AZO films deposited under the three base-pressure regions is measured using Perkin-Elmer Lambda900 spectrophotometer over the wavelength between 300nm and 900nm, the spectrum region where solar light has most of its intensity. Figure 4-1 shows plots of the optical transmission of the resulting films as a function of incident-light wavelength for the three pressure-regimes investigated. The results clearly demonstrate that increasing the base pressure improves the optical transmission. For the film deposited under low base pressure, the average optical transmission between wavelength 300 nm and 900 nm is below 70%. The two films deposited under medium and high base pressure show better optical property and meet this requirement. Generally, for solar cell applications, an average optical transmission of 80% is desired for the visible and near infrared wavelength region.

It is known that the optical transmission and conductivity of zinc oxide is directly related to the stoichiometry, *i.e.*, the ratio between zinc and oxygen content. Higher concentrations of oxygen vacancies or zinc interstitials in turn provide higher concentrations of intrinsic carriers and result in a more conductive film. However, under such circumstances the optical transmission would be expected to drop. This is exactly what reflected in Figure 4-1, where the optical transmission indeed increases when the base-pressure favors the presence of water vapor in the chamber. Under the plasma environment the residual water vapor dissociates and the active oxygen species from the water vapor contributes the incorporation of oxygen in the sputtered AZO films. This explains why the optical transmission increases with an increasing of the base pressure.

Electrical property

Figure 4-2 plots the effect of each of the three base-pressure regimes on the resistivity of the sputtered AZO thin films. An arbitrary continuous line is drawn between the experimental points simply to suggest a trend and to aid in the discussion of the results. First consider the results obtained at the medium and high base-pressure regions. Note that the resistivity decreases as the base pressure is reduced from the high to the medium region. This result is expected because under medium base-pressure conditions the AZO films are more zinc-rich (*i.e.*, oxygen deficient) because less water vapor is present, leading the more conductive film.

Next consider the results obtained at the low and medium base-pressure regions. In contrast to the previous case, the resistivity now increases as the base pressure is reduced from the medium to the low region. Obviously, in this case a different mechanism must be in playing a significant role to a point where it causes a reversal in the resistivity trend. The explanation for this observation is based on the fact that less residual water vapor is present at the low base pressure, promoting the presence of insufficient amounts of hydrogen. The observation of this resistivity trend reversal lends evidence indicating that hydrogen plays a critical role in the resistivity of sputtered AZO thin films. Details of hydrogen effect on sputtered AZO will be addressed in the next chapter.

Growth rate

The effect of base pressure on growth rate was investigated. A series of films were deposited under all same deposition conditions except starting from different base pressures, which are 8×10^{-7} Torr, 1×10^{-6} Torr, 2×10^{-6} Torr, and 3×10^{-6} Torr respectively. From the results shown in Figure 4-3, an increase of the base pressure from 8.0×10^{-7} Torr to 3×10^{-6} Torr caused a growth rate decrease from 3.4 Å/second to 2 Å/second. This effect is also due to the existence of water vapor. The oxygen generated in the highly energetic plasma process not only reacts with

the deposited film, it also reacts with the target and increases the oxidation extent of the target. It is known that the sputtering rate for an oxide target is generally much lower than that of a metal target under the same sputtering conditions. Thus, the growth rate from a more oxidized target is expected to be smaller than that from a more reduced target, when all other sputtering conditions are held constantly.

Power Effect

The effect of deposition power on the resistivity of sputtered ZnO:Al films was investigated by holding all other deposition parameters as constant except the power.

All other deposition conditions are fixed with target to substrate distance of 5 cm, base pressure of 8.0×10^{-7} Torr, and working gas pressure 4 mTorr.

The results show that the power can directly affect the resistivity. As shown in Figure 4-4, it is clear that with all other deposition parameters held as constant, the film deposited at 400W shows lower resistivity than those obtained using other values of power.

The relation between growth rate and deposition was also evaluated and the result is shown in Figure 4-5. It can be seen that the trend is increasing the deposition power causes the increase of the film growth rate. This is caused by an increase of the sputter yield upon increasing the deposition power.

Discharge power is a critical factor that determines the properties of sputtered ZnO. When sputtering from a compound target, the more volatile component can be more rapidly lost into the gas phase without being condensed on the substrate. This may result a different stoichiometry of the film from that of the target. For the case of ZnO sputtering, oxygen is more volatile than zinc. With a careful adjustment of the deposition power, a desired Zn rich stoichiometry can be achieved.

Through experiments, it is observed that the deposition parameters, especially the power, can affect the surface stoichiometry of the ZnO target. For magnetron sputtering of ZnO, when large power density (greater than 2 Watt/cm²) is exerted on the target for a long period of time, the target surface could be significantly reduced. Thin films sputtered from a heavily reduced target can contain strong separated Zn phase. This conclusion is obtained by employing X-ray diffraction characterization on sputtered thin film from a reduced target. The equipment used was a Philips APD 3720 powder diffractometer using Cu K α radiation with $\lambda(K\alpha 1)$ equals 0.154056 nm and $\lambda(K\alpha 2)$ equals 0.154439 nm. The X-ray generation conditions on the diffractometer were set at 40KV and 20mA.

For survey scanning, continuous scans with a 2θ range between 10° to 80°, a step size of 0.03°, and a step time of 0.5 second was used. Figure 4-6 shows the XRD survey pattern of a thin film sputtered from a heavily reduced target. The vertical lines indicate the 2θ angle and relative intensity of Zn taken from JCPDS database. It is evident that there is Zn phase available in the resulted thin film. In contrast, Figure 4-7 shows the XRD survey pattern of a typical ZnO thin film sputtered from an oxidized target. The pattern shows a strong ZnO (002) peak indicating the sputtered film has preferred orientation. These results show evidently that the target condition is important determining the property of sputtered ZnO thin film. A control of deposition power with in certain limit is required to maintain the oxidization status of the ZnO target.

High resolution continuous scans were also implemented using the following parameters: 2θ ranging from 33.5° to 35.5°; step size of 0.01°; and 1.0 second per step. Figure 4-8 shows the high resolution scan pattern of three AZO thin films deposited at 300 W, 400 W and 500 W,

respectively. The Full Width at Half Maximum (FWHM) values were obtained from the high resolution scan and their values are list in table 4-1.

Table 4-1 also contains grain size information. The mean grain size τ was evaluated using Scherrer equation [59] :

$$\tau = \frac{K\lambda}{\beta \cos \theta} \quad (4-1)$$

where K is a constant called shape factor, whose typical value is 0.9[60]. The term β represents the line broadening due to the effect of small crystallites. Note it is the additional broadening in diffraction peaks beyond the inherent peak widths due to the instrument effect. The instrument broadening contribution can be obtained by measuring a standard material that has no significant stress and grain size effect. Here for approximation, only the measured FWHM in radians was used. The other two terms λ and θ are the wavelength of the X-ray and the diffraction angle. With this simplification, the estimated grain sizes are 36.3, 32.3, and 30.7 nm for films deposited using 300W, 400W and 500W, respectively.

Working Pressure Effect

Similarly, the relationship between working pressure and film resistivity is investigated by changing the working pressure while fixing all other deposition parameters. Experiments are done under four working pressure evenly distributed between 2 mTorr and 5 mTorr. The results are shown in Figure 4-9. It is clear that 4 mTorr working pressure gives the lowest film resistivity for this specific experiment set.

The film growth rate is also dependent on working pressure. As shown in Figure 4-10, the general trend is increasing the working pressure would lead to an increase of the film growth rate. This effect is especially strong at the relatively low working pressure region with pressure

changing from 2 mTorr to 3 mTorr. The curve start to flat out at high pressure region and only a slight increment was observed when increasing the pressure from 3 mTorr to 5 mTorr.

High resolution XRD scans of films deposited with different working pressures are shown in Figure 4-11. The three working pressures used are 2 mTorr, 3 mTorr and 4 mTorr. All other deposition conditions are fixed with target to substrate distance of 5 cm, base pressure of 4.0×10^{-7} Torr, and deposition power of 500W. It is found that the measured FWHM of the three XRD rocking curves decreases with the increased working pressure, indicating larger grain size can be achieved by using a higher working pressure.

Characterization

Besides four-point-probe, profilometry and X-ray diffraction, other characterization techniques were used in analyzing sputtered ZnO thin films. Auger electron spectroscopy was applied for chemical composition and depth profile analysis. Atomic force microscopy was used to evaluate surface morphology properties.

Auger Electron Spectroscopy Analysis

Auger electron spectroscopy was utilized to verify the chemical composition of the deposited films and to detect any unexpected impurities that may exist in the deposited films. Results reveal that the films contain only Zn, O and Al in the bulk, with C contamination only in the surface. The source of the carbon is organic contaminations residing on the surface of the sample. Depth profile analysis shows a uniform distribution of Zn and O through the film, indicating good stoichiometry control during the deposition.

Auger electron spectroscopy is a surface sensitive analytical technique because the Auger electron, generated with a small energy, can only escape from a few atomic layers on the top. Like SEM, Auger electron spectroscopy uses a electron beam hitting the sample to generate secondary and Auger electrons. The resulted secondary electrons can be collected and

transferred into secondary electron images, which is just like what a scanning electron microscopy does. Beyond that, the Auger electrons are analyzed by a cylindrical mirror analyzer (CMA) and transferred to information regarding the chemical composition.

The distance between the CMA and the sample surface was always calibrated using the elastic scattering peak from a 3KeV electron beam before taking the survey spectrum. Typical energy of the electron beam used for survey spectrum was varied between 5KeV to 10KeV. The spectrum of counted electrons at an energy ($n(E)$) versus kinetic energy (KE) were taken with an energy step size of 1.0 eV, and a dwell time of 30ms at each energy step. Ten sweeps of this spectrum were taken over the energy range of 50 to 2050 eV and the average value was used for numerical processing. This spectrum is then numerically differentiated using algorithm from the computer acquisition software (AugerScan) to yield the spectrum in terms of $d(n(E))/d(E)$ versus kinetic energy. The differentiated spectrum is then used to compare standard results and consequently determine the elements present on the sample's surface.

Surface scan

Figure 4-12 shows a survey spectrum of an AZO thin film. The differentiated energy distribution $d(n(E))/d(E)$ was plotted against the kinetic energy. The key instrument parameters used for this survey were as follows: e-beam acceleration voltage 5kV, probe current 50nA, and sample tilting 30 degrees. The Auger peaks of C, O, and Zn are identified and labeled in the figure. The result verifies the film composition as Zn, O and it also suggests that there is carbon contamination at the surface of the ZnO film. The source of carbon is from organic contaminations on the sample surface. These contaminations can be reduced by careful handle and storage of the sample after it is taken out of vacuum.

Al peak was not distinguishable from Figure 4-12. Various factors are responsible for it. First of all, the noise signal level is quite significant due to the surface contamination. Secondly,

Al only constitutes less than 2% of the target, therefore, it is estimated the film would only contain a relatively small amount of Al. The third reason is Al has a small relative sensitivity factor S_x (~ 0.09 , 10keV) compared with Zn (~ 0.16 , 10keV) and O (~ 0.4 , 10keV).

Ar ion beam was used to sputter the sample surface for 3 minutes to remove the surface contamination. Another survey spectrum was taken using identical survey conditions and the result is shown in Figure 4-13. Compared with result shown in Figure 4-12, it is clear that the carbon peak is no longer present. This verifies the previous assumption that carbon is only a surface contamination and not part of the film constitution. Ar peak is detected indicating implanted Ar from the ion beam exist on the surface of the sample. Comparing with previous results, the noise signal in the second survey (shown in Figure 4-13) is much smaller than that in the previous survey (shown in Figure 4-12). Considering the fact that two scans used identical survey parameters, the noise reduction was achieved through the removal of surface contaminations. Semi-quantitative data of the concentration of each species detected are also labeled in the diagram.

Al sensitivity

Because of the reasons presented earlier, the aluminum peak was not clear in either of the previous cases. To identify the aluminum peak and verify its existence, another scan was conducted using higher e-beam energy. Increasing the acceleration voltage to 10kV, the new survey result is shown in Figure 4-14. In this spectrum, Aluminum Auger peak at approximately 1375 eV kinetic energy was clearly distinguished. The increased beam energy caused more excitation of Al Auger electrons, which increased the size of the peak, making it distinguishable from the noise signal.

Depth profile

Depth profile was measured to examine the distribution of those main elements along the depth of the sample. Depth profile analysis can be performed using the window method by alternatively sputter etching the sample and collecting small energy windows of Auger spectrum focused on the peaks for elements of interest. The energy window is defined using the 3-point method, which uses two background energy position and one peak energy position to define the area of the peak. The system uses the difference between the peak value and the background values to evaluate the intensity of the peak. This intensity is then plotted as a function of the sputter etching time, giving a distribution of the element distribution along the depth direction. Parameters used for collecting depth profiles are presented in Table 4-2. The sputtering rate can be controlled by adjusting the ion beam parameters. With the Ar ion beam energy of 3KeV, beam current of 90 nA and raster pattern of 3x3 mm, the sputter etch rate is estimated to be approximately 100 Å/min.

Figure 4-15 shows the Auger depth profile of a ZnO thin film. 30 sputtering cycles was used in the particular measurement and during each sputtering cycle, the sample is sputtered for 6 seconds. Therefore, the estimated sputter etch rate is approximately 10 Å/cycle and a total depth of approximately 300 Å into the bulk of the film was characterized. The results show that carbon contamination is highest on the surface, and that it stabilizes at noise level at the position approximately 100 Å below the surface. The depth profile analysis also shows that the concentration of Zn and O inside the bulk of the film is uniform.

Atomic Force Microscopy

Atomic force microscopy was applied to examine the surface morphology of sputtered AZO thin films. A Veeco DI Dimension 3100 system was utilized for this purpose. The surface

of the sample was carefully cleaned using acetone to remove attached contaminations before the examination.

The AFM image was digitally processed before any analysis is performed to eliminate the effects coming from artifacts such as tilt and bow. Tilt happens when the sample is not perfectly leveled and bow is generally caused by large area scans using a large scanner. These unwanted effects need to be eliminated before surface roughness analysis is performed.

A “Flatten” command from the diNanoScope Software 7.0 was first executed to eliminate unwanted features from scan lines. A third order flatten is used. The software calculates a third order least-squares fit then subtracting it from the scan line. This effectively removes the Z offset between scan lines and also eliminates sample tilt and bow from each scan line. After flattening, “Plane Fit” command which computes a polynomial of a selectable order for an image and subtracts it from the image was used. A third order “Plane Fit” command was applied on both X and Y direction. Arithmetic roughness R_a and root mean square roughness R_q values are then obtained from the roughness analysis. R_a is the arithmetic average of the absolute value of the surface height deviation and R_q is the standard deviation of the surface height value. They can be expressed using the following equations:

$$R_a = \frac{\sum |z_i - \bar{z}|}{N} \quad (4-1)$$

$$R_q = \sqrt{\frac{\sum (z_i - \bar{z})^2}{N}} \quad (4-2)$$

where z_i is the height value of a specific position and N is the total number of positions evaluated.

Figure 4-16 shows the AFM micrograph of AZO thin films deposited using identical deposition parameter except the working pressure. Sample a,b, and c are grown on Corning

1417 glass substrates under working pressure 2mTorr, 3mTorr and 4mTorr, respectively. Care was taken to ensure the samples have similar thickness to eliminate the thickness effect on surface morphology. It is found that with the increase of the working pressure, larger grain size is found on the sample surface. Generally, larger grain size is favorable for polycrystalline AZO because it can be beneficial to reduce grain boundary effect and therefore increase the electron mobility, which then improves the conductivity of the film. The surface roughness also increases along with increasing the working pressure. With a working pressure change from 2mTorr to 4mTorr, the root mean square roughness increased from 2.2nm to 3.6nm. Details of the roughness data change with the working pressure is shown in Table 4-3.

The AFM analysis shows that 4mTorr is a favorable working pressure for larger grain sizes. Since larger grain size tends to yield a better conductivity, this is consistent with the resistivity characterization presented earlier, which indeed showed that AZO sputtered using 4mTorr working pressure has lower resistivity.

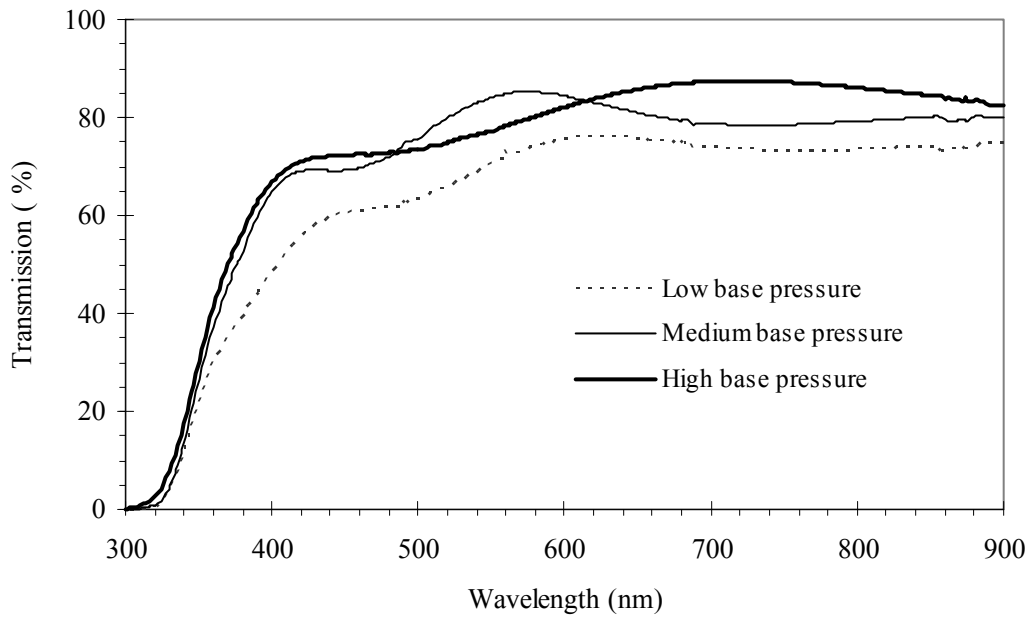


Figure 4-1. The effect of base pressure on the optical transmission of sputtered AZO films.

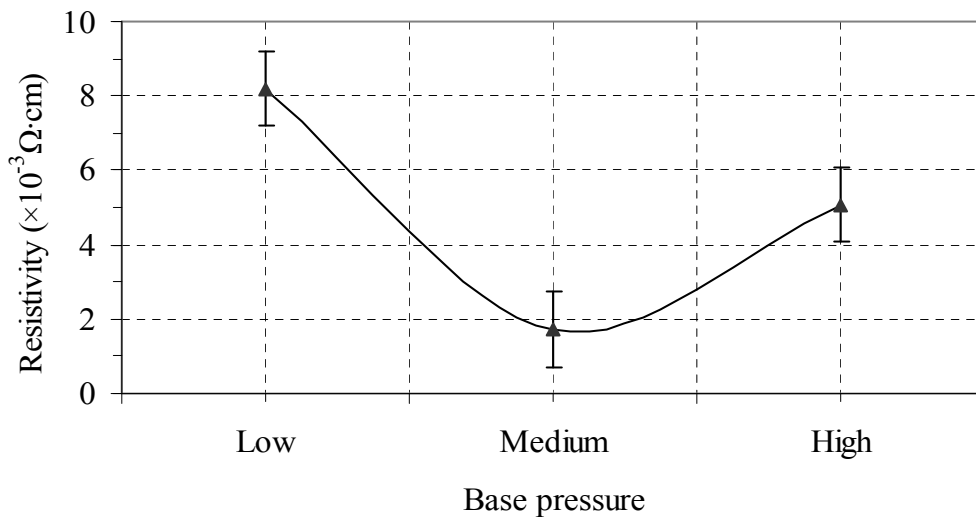


Figure 4-2. Effect of base pressure on the resistivity of sputtered AZO films.

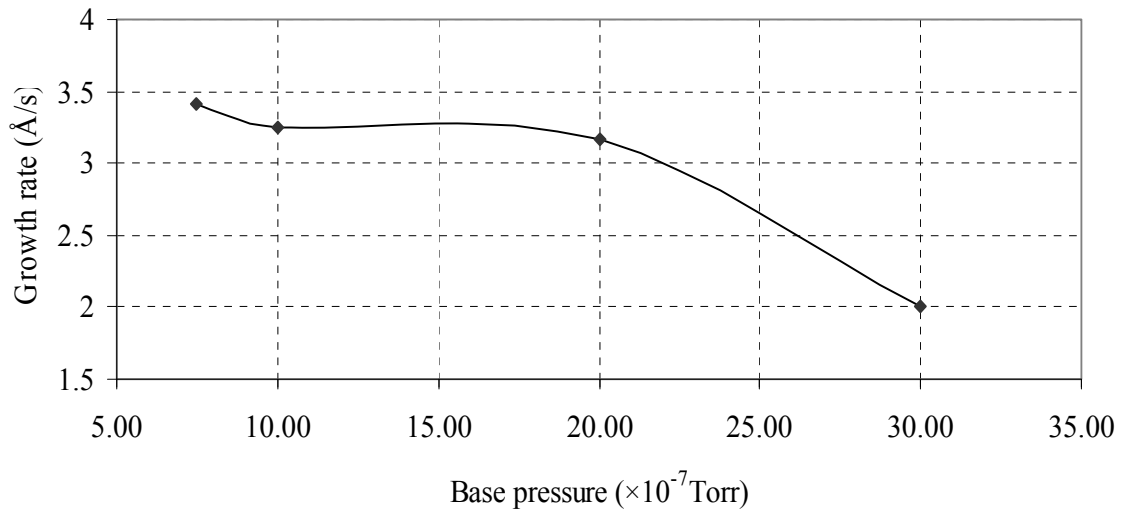


Figure 4-3. The effect of base pressure on the growth rate of ZnO:Al thin films (Fixed conditions: $D_{ts} = 5$ cm, $P = 4$ mTorr, Power = 400W).

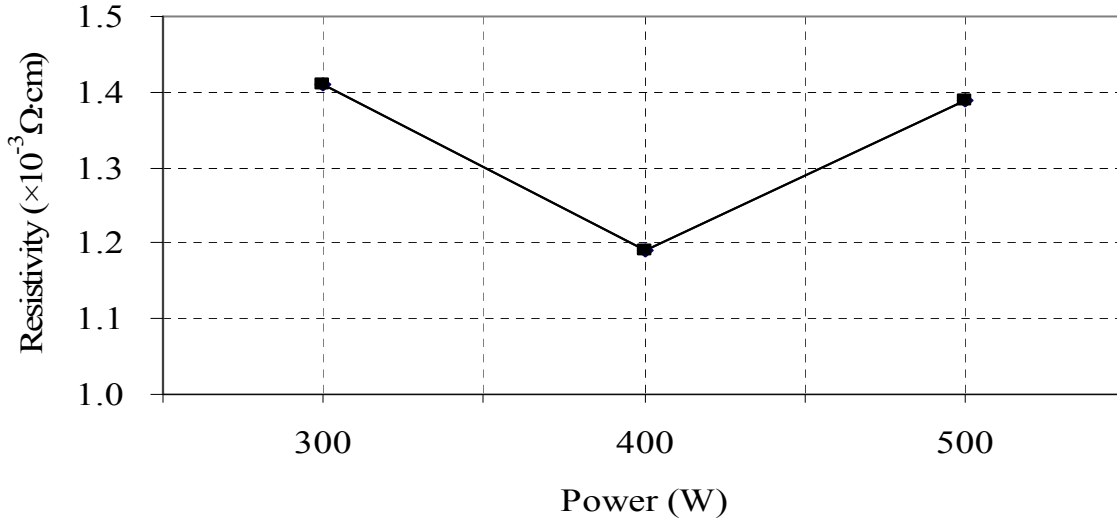


Figure 4-4. The effect of power on the resistivity of as grown ZnO:Al thin films (Fixed conditions: $D_{ts} = 5$ cm, $P_b = 8.0 \times 10^{-7}$ Torr, and $P = 4$ mTorr).

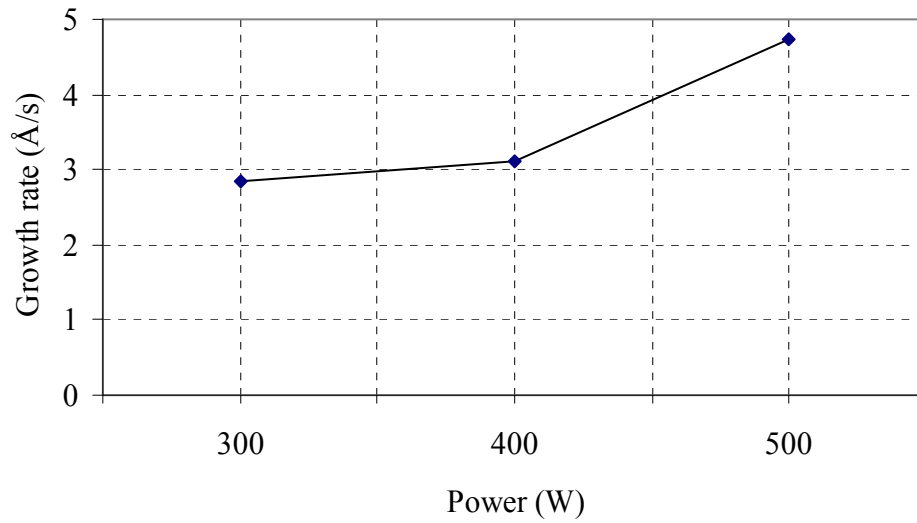


Figure 4-5. The effect of power on the growth rate of ZnO:Al thin films (Fixed conditions: $D_{ts} = 5$ cm, $P_b = 8.0 \times 10^{-7}$ Torr, and $P = 4$ mTorr).

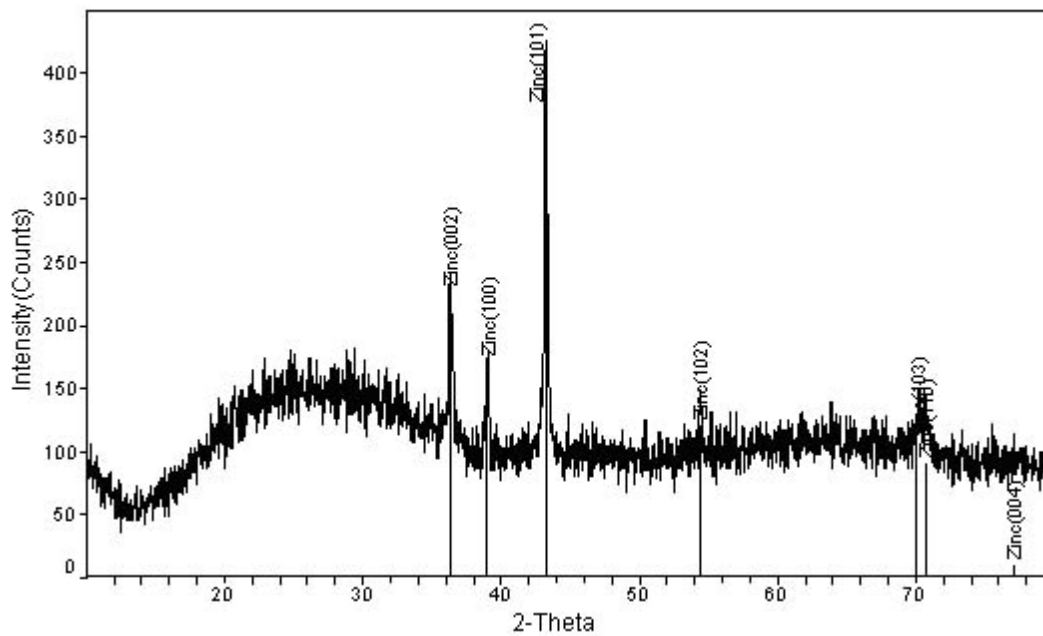


Figure 4-6. X-ray diffraction pattern of thin films deposited from a reduced ZnO target

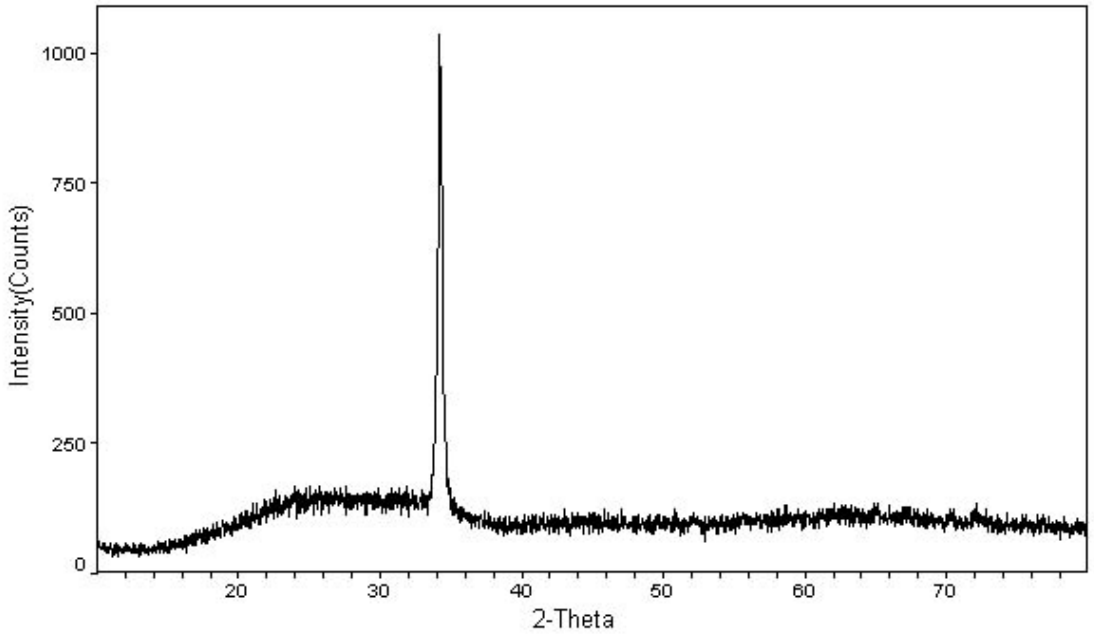


Figure 4-7. X-ray diffraction pattern of thin films deposited from an oxidized ZnO target

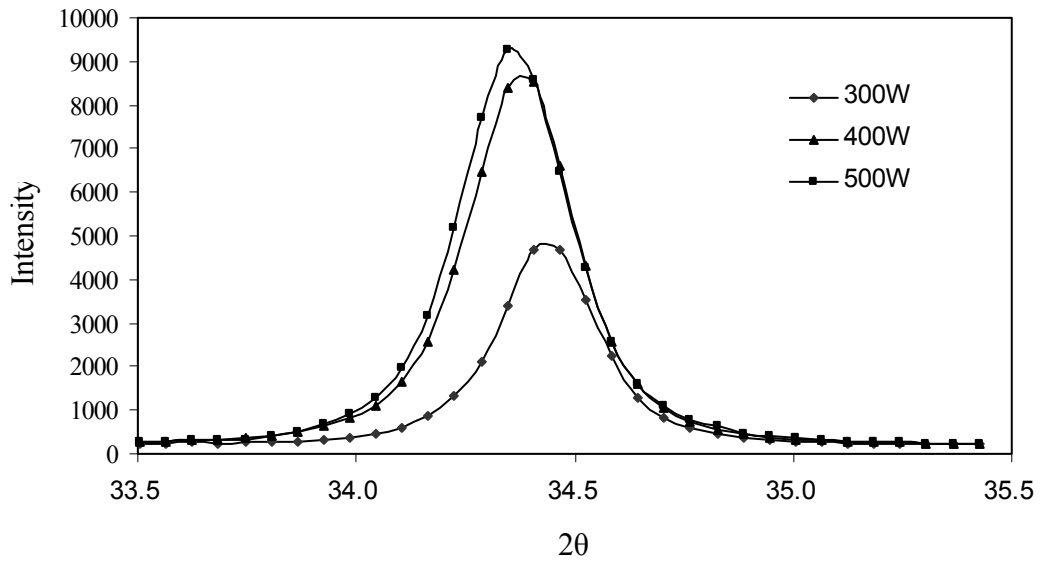


Figure 4-8. High resolution XRD pattern for AZO films deposited using different power (Fixed conditions: $D_{ts} = 5$ cm, $P_b = 8.0 \times 10^{-7}$ Torr, Pressure = 4mTorr).

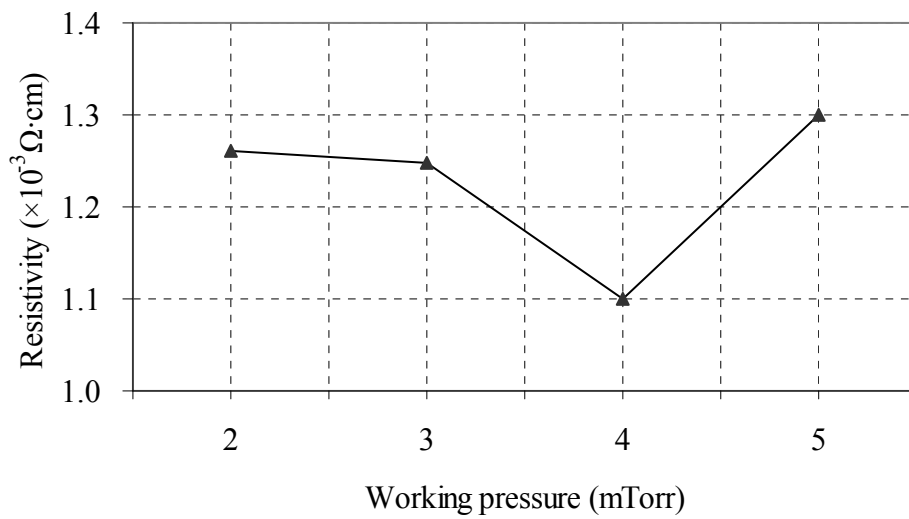


Figure 4-9. The effect of working pressure on the resistivity of ZnO:Al thin films (Fixed conditions: $D_{ts} = 5 \text{ cm}$, $P_b = 8.0 \times 10^{-7} \text{ Torr}$, and Power = 500 W)

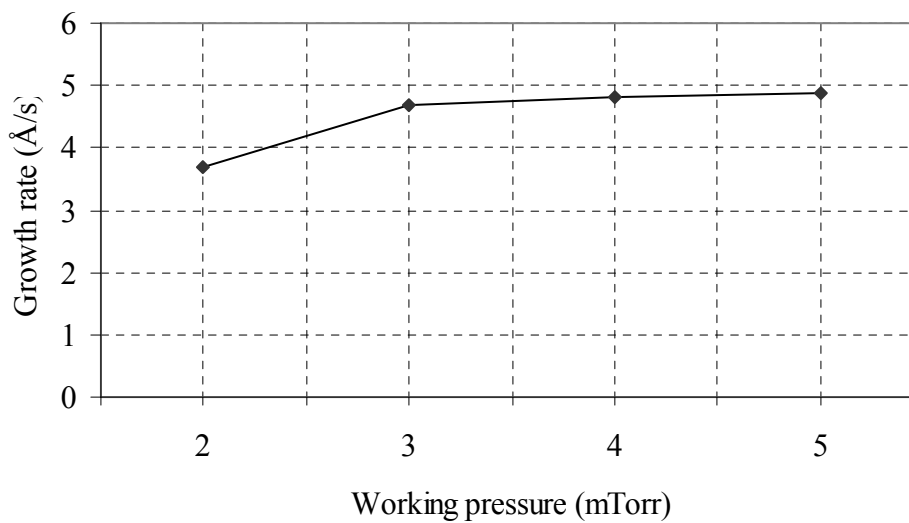


Figure 4-10. The effect of working power on the growth rate of ZnO:Al thin films (Fixed conditions: $D_{ts} = 5 \text{ cm}$, $P_b = 8.0 \times 10^{-7} \text{ Torr}$, and Power = 500 W)

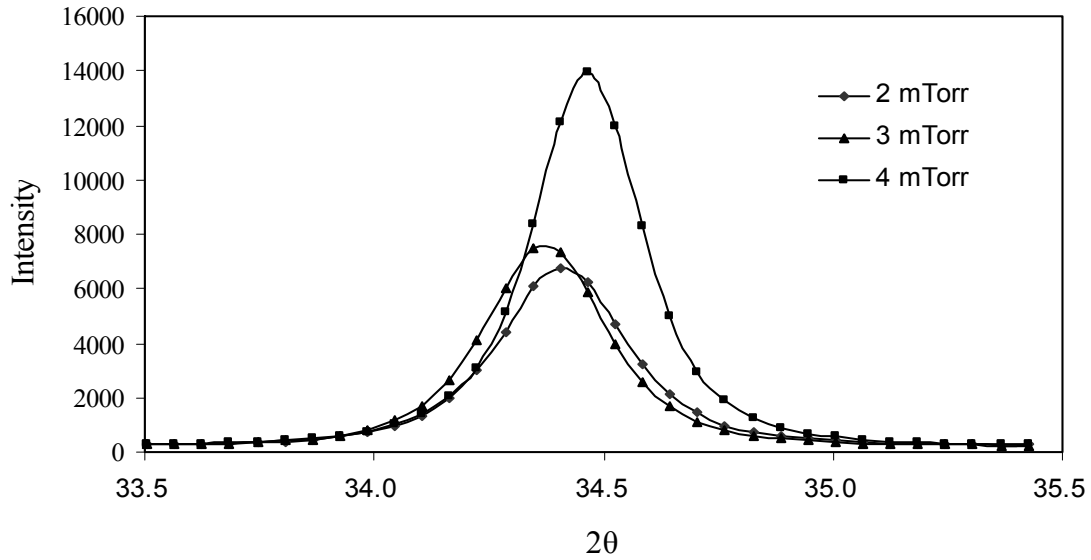


Figure 4-11. High resolution XRD pattern of AZO thin films deposited at different working pressures (Fixed conditions: $D_{ts} = 5$ cm, $P_b = 4.0 \times 10^{-7}$ Torr, Power = 500 W).

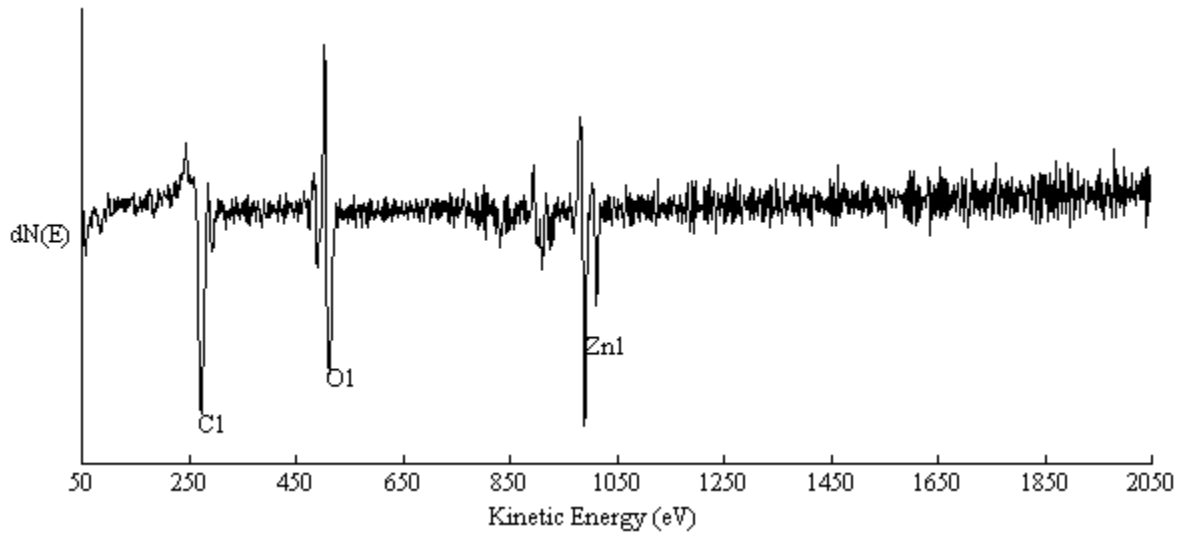


Figure 4-12. AES survey scan pattern for an AZO thin film with organic contamination on the surface.

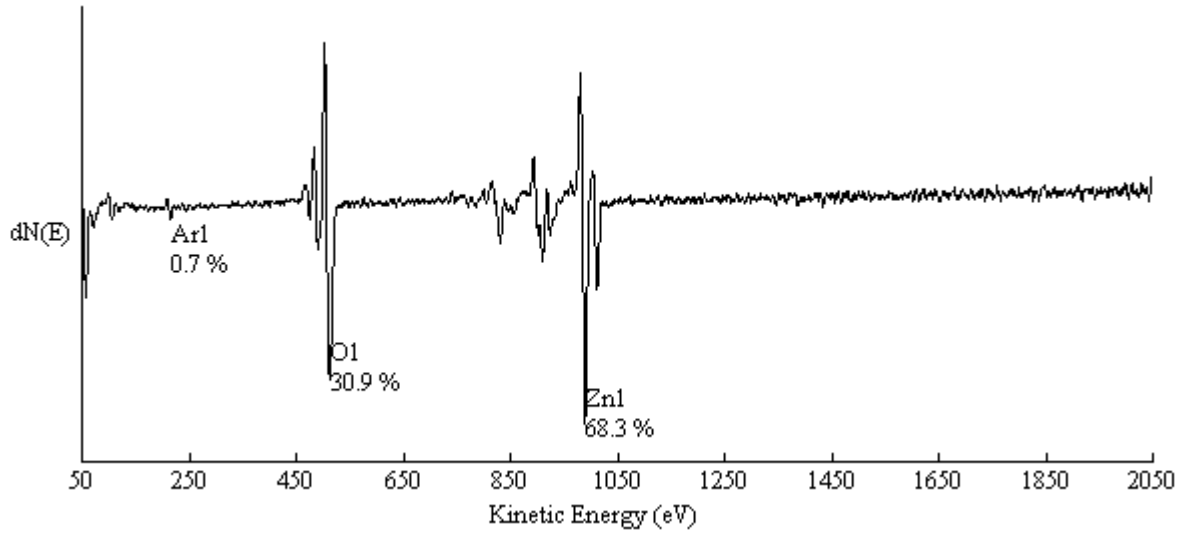


Figure 4-13. AES scan results after sputtering for 3 minutes.

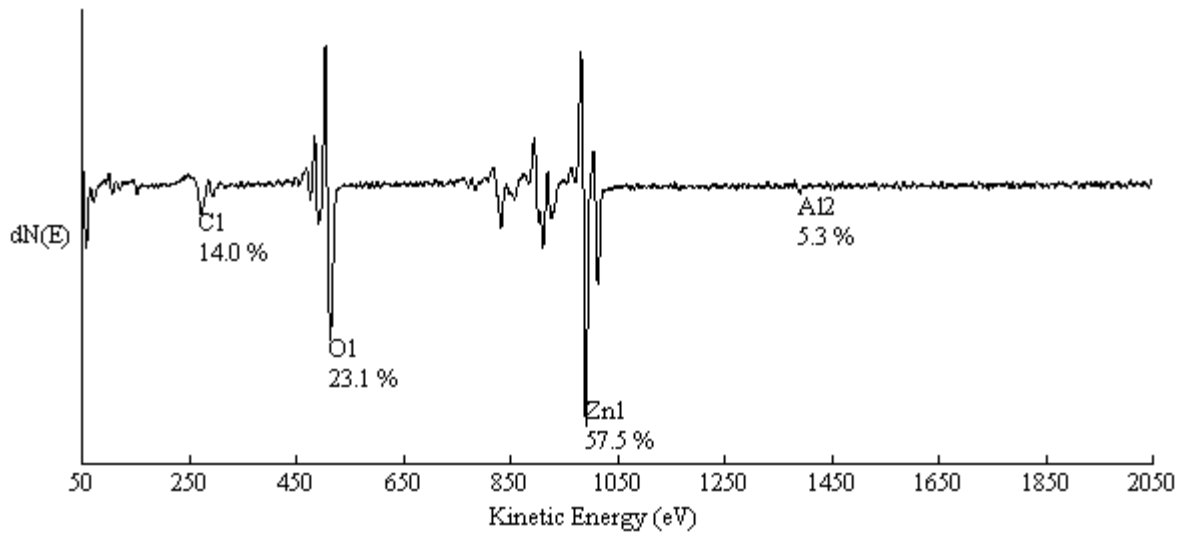


Figure 4-14. Al Auger peak shown by using increased primary beam energy

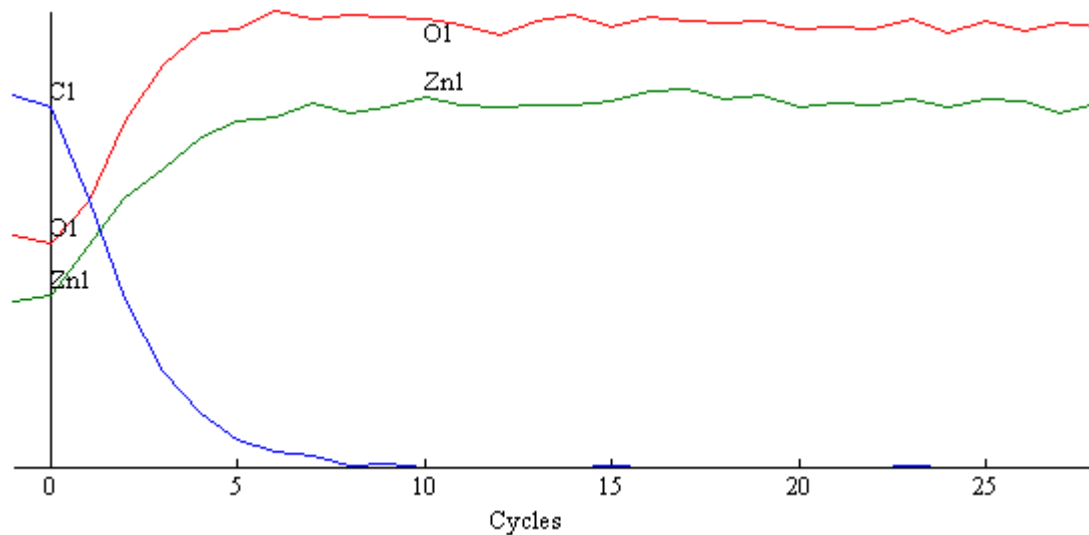
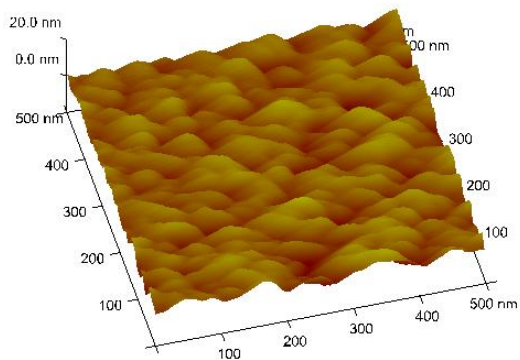
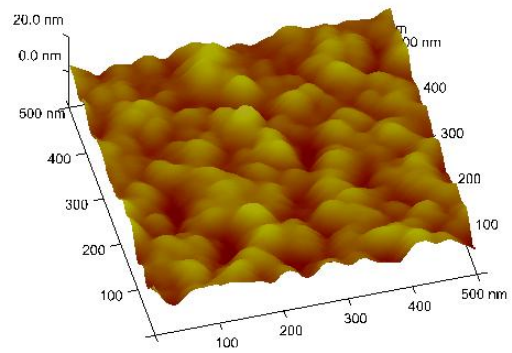


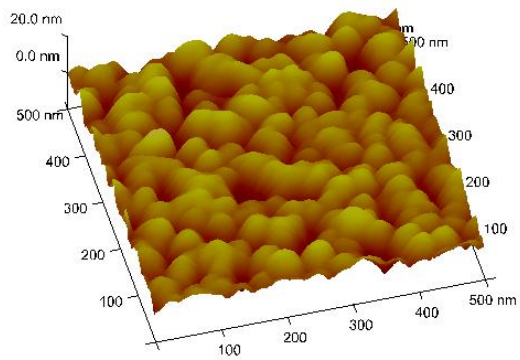
Figure 4-15. Depth profile for each element of AZO obtained with AES.



a)



b)



c)

Figure 4-16. AFM graph of AZO thin films deposited with different working pressure. a) 2mTorr, $R_q=2.2\text{nm}$; b) 3mTorr, $R_q=2.8\text{nm}$; c) 4mTorr, $R_q=3.6\text{nm}$.

Table 4-1. Estimated grain size using XRD data obtained for AZO deposited at different power.

Deposition power	FWHM	Grain size
300 W	0.229°	36.3 nm
400 W	0.257°	32.3 nm
500 W	0.270°	30.7 nm

Table 4-2. Parameters used for collecting the Auger depth profile of AZO thin films.

Peaks of interest	Peak energy (eV)	Background E1 (eV)	Background E2 (eV)	Dwell time (mS)	Number of sweeps
O1	506.0	523.0	479.0	250	2
Zn1	985.0	1017.0	975	250	2
C1	264.0	298.0	200.0	250	2

Table 4-3. AFM surface roughness evolution with working pressure.

Working pressure (mTorr)	R _q (nm)	R _a (nm)
2	2.2	1.7
3	2.8	2.3
4	3.6	2.9

CHAPTER 5 EFFECT OF HYDROGEN ON SPUTTERED ZINC OXIDE

Motivation from the Base Pressure Effect

The observation of base pressure's effect on AZO resistivity indicates that residue water vapor plays a critical role in determining the resistivity of sputtered zinc oxide thin film. Under the plasma environment during sputter deposition, the water vapor decomposes into hydrogen and oxygen. With the base pressure variation in the order of 10^{-7} Torr, the change of oxygen coming from H_2O is quite small and would not affect the amount of oxygen in the resulted film in dramatic fashion. Therefore, it is highly suspected that hydrogen, the other ingredient from H_2O plays certain roles in sputtered ZnO.

In most semiconductors interstitial hydrogen presents itself as an amphoteric impurity [61], and acts in a fashion that counteracts the prevailing conductivity. This behavior makes hydrogen an unusual candidate for semiconductor doping. However, in the case of zinc oxide, Van de Walle [62] predicted that interstitial hydrogen can provide a donor level just below the conduction band and that therefore it could contribute to enhance n-type conductivity in this material. Experimentally, hydrogen implantation experiments showed the change of carrier concentration and mobility in ZnO films [63]. However, hydrogen doping of ZnO needs to be experimentally implemented in our Perkin-Elmer sputtering system to see if a more conductive film can be obtained.

Experiments and Results

To directly investigate the effect of hydrogen on the electrical properties of sputtered AZO thin films, two groups of AZO films were deposited on soda-lime glass using identical conditions, except the composition of the sputtering gas. One group was deposited using UHP argon only, and the second group using a gas mixture of argon and 0.1% hydrogen gas. Special

care was taken trying to maintain an identical deposition conditions. This includes identical sputter parameter, deposition duration, substrate position, etc. The relevant experimental conditions are given in Table 5-1. The soda-lime glass substrates were thoroughly cleaned using the method described in Chapter 3 before depositing with the AZO films.

The resistivity obtained through four-point-probe and profilometry measurement of thin films from the two groups is plotted in the graph presented in Figure 5-1. AZO stands for the thin films sputtered using pure argon and H-AZO represents those grew with argon and hydrogen mixture.

The data reported in Figure 5-1 clearly demonstrates that the use of an argon-hydrogen gas mixture significantly decreases the resistivity of the sputtered AZO thin film. This observation is consistent with the claims made previously regarding the beneficial effect of the presence of hydrogen from the viewpoint of enhancement of the film conductivity. Hence, the data provides a strong experimental evidence to justify the claims of hydrogen's beneficial effect on sputtered AZO thin films in terms of lowering the resistivity.

Hall Characterization

To obtain an in-depth understanding of the mechanism on this improvement of conductivity, Hall measurements are done to evaluate the carrier concentration and mobility change between the AZO films deposited with pure Ar and Ar/H₂ gas mixture. Special care was taken to make sure the samples were taken from areas with identical positions under the target. This ensures the elimination of possible effects coming from the location difference.

Figure 5-2 shows Hall measurement results obtained for two AZO films. The sample denoted as AZO in the figure was deposited using only argon as the working gas, and the sample denoted as H-AZO was deposited using 0.1% hydrogen in the working gas. The results show that the carrier concentration increased from $2.5 \times 10^{20} \text{cm}^{-3}$ for the AZO film to $4.7 \times 10^{20} \text{cm}^{-3}$ for

the hydrogen doped H-AZO film while the hall mobility dropped from $15.1\text{ cm}^2/(\text{V}\cdot\text{s})$ to $12.7\text{ cm}^2/(\text{V}\cdot\text{s})$. As a result, the resistivity decreased from $1.67\times 10^{-3}\Omega\cdot\text{cm}$ for the AZO sample to $1.05\times 10^{-3}\Omega\cdot\text{cm}$ for the H-AZO sample. The resistivity value is consistent with that obtained using four-point probe measurement. It is evident that hydrogen improved the conductivity through increasing the carrier concentration inside the AZO film, indicating that it either acts as a dopant or increases the doping efficiency of aluminum for these sputtered ZnO thin films.

AFM and SEM Characterization

Atomic force microscopy was used to analyze the surface morphology of ZnO sputtered using different sputtering gas. A scan area of $1\times 1\mu\text{m}$ was used. Like mentioned in Chapter 4, the “Flatten” and “Plane Fit” commands from the diNanoScope Software 7.0 were applied to eliminate unwanted features such as tilt and bow. The root mean square roughness R_q and the arithmetic roughness R_a of the sample surface were then evaluated. The definition of these two parameters can be found in Chapter 4.

Figure 5-3 shows a comparison of surface morphology between AZO sputtered with Ar (referred to as AZO in the figure) and $\text{Ar}+0.1\%\text{H}_2$ (referred to as H-AZO in the figure). They are grown on soda-lime glass cleaned using the procedure described in Chapter 3. Both films have similar thickness of 600nm and they were deposited using identical deposition conditions except with different sputtering gas. Details of the deposition conditions are listed in Table 5-2.

The result shows that the AZO sputtered using Ar and H_2 mixture shows a much larger grain size compared to the film sputtered using Ar only. The RMS roughness R_q and R_a of these two films are compared in Table 5-3. It can be seen that the root mean square (RMS) roughness R_q of H-AZO film almost doubled that of the AZO film. This indicates that a much larger grain size can be achieved through using the Ar and H_2 mixture gas.

The thickness effect on surface morphology of sputtered ZnO was also investigated. H-AZO films with different thickness deposited using Ar and H₂ mixture gas were characterized and the resulted AFM micrographs are shown in Figure 5-4. It is clear that increasing the film thickness would tend to yield larger grain size. The R_q and R_a values of ZnO films with different thickness are shown in Table 5-4. The trend is that the surface roughness increases when the film gets thicker.

Figure 5-5 shows a typical cross-section SEM image of a H-AZO thin film grown on i-ZnO substrate. It can be seen that the film contains large column shaped grains grown perpendicular to the substrate.

Film Uniformity Study

To investigate the uniformity related issue, aluminum doped zinc oxide thin films were deposited onto large size glass substrate covering areas up to 3 inches away from the center axis of the target. The deposition duration was 30 minutes.

The thickness of the film was measured every 0.5 inch along the radius and the results are shown in Figure 5-6. Sheet resistance was measured using four-point probe at identical positions where the thickness was measured and the result is shown in Figure 5-7. Resistivity was then calculated and its variation with position is shown in Figure 5-8. In these figures, a position of 0 inch indicates the position directly below the target center. The number in front of a position indicates the distance between this position and the 0 inch center point. The positive or negative sign of this number indicates the position locates at the right hand side of the center point or the left hand side, respectively. For example, a position with a value of -1 inch denotes the location one inch away from the center point sitting on the left hand side.

From Figure 5-6, it is clear that the film thickness is the lowest at the center point and it increases with an extended distance from the center point until it reaches its maximum value of

about 600nm at the location approximately 2.5 inch away from the center point. After passing this maximum point, the thickness starts to decrease with increasing the distance from the center point.

Figure 5-7 and Figure 5-8 indicate that the sheet resistance and film resistivity show similar distribution along the axial direction. The resistivity at the center point is the highest and it decreases along the direction away from the center. This trend persists until a minimum value is reached at the position approximately 2-2.5 inch away from the center point. After this point, the resistivity starts to increase again.

To further investigate the mechanism behind the resistivity distribution, Hall measurement was utilized to reveal the carrier concentration and mobility variation on films with different positions under the target. Two samples were cleaved off the large substrate from positions with the highest and lowest resistivity indicated by four-point-probe measurement results. The comparative results are shown in Table 5-5. It is found that the film deposited directly under the center of the target has a much lower electron mobility and relatively higher carrier concentration comparing to that deposited 2.5 inch away from the center. As a result, the lower electron mobility directly leads to a higher resistivity. The lower electron mobility of the film deposited at the center point could be caused by the heavy bombardment of the ions from the plasma during the sputtering deposition process. It is noteworthy that for hall measurement, the measured carrier concentration is directly related to the van der Pauw sample thickness, which is a manual input before the measurement. Due to the nature of non-uniformly distributed film thickness along the Hall sample, it is difficult to use an accurate description of the Hall sample thickness. Thus, some errors could exist on the carrier concentration results.

The resistivity obtained by using Hall and four-point-probe measurements is compared in Table 5-6. It can be found that the resistivity values obtained from different methods fall in a reasonable close range. The difference between results obtained using these two measurement techniques could come from the uncertainty of the position where the Hall samples were cleaved from.

Summary

The experiments on base pressure effect on sputtered AZO thin films are extended to very low base pressure region. The resistivity obtained at this region show different trend from those at higher region presented in Chapter 4. Results suggest that hydrogen emanating from residual water vapor affects in a favorable fashion the resistivity. This supports Van de Walle's theory on hydrogen's doping effect on zinc oxide thin films.

To direct investigate hydrogen's effect, a different sputtering gas consisted of UHP argon and 0.1% hydrogen was utilized to produce AZO thin films. Properties of resulted AZO thin films were compared with control sample. Hall measurements show an increase of both carrier concentration and mobility, resulting a much more conductive thin film. This directly provides a second piece of evidence confirming the claimed role of hydrogen.

The results are particularly relevant from practical viewpoint, given that it is demonstrated that improved optical and electrical properties can be obtained by the addition of hydrogen into the working gas and/or the selection of a relatively high base-pressure that permits the presence of residual water vapor in the chamber. This identifies a path towards the development of a more consistent method for depositing good-quality transparent AZO films via magnetron sputter deposition method. Further work needed to achieve this goal include experimental studies aimed at characterizing the optimal ranges of hydrogen content in the working gas as well as the optimal range of operating base-pressures. This is a feasible goal

given that the experimental evidence provided here conclusively demonstrates that the two variables in question have a significant effect on the electrical and optical film properties.

The film uniformity distribution was investigated on AZO thin films sputtered using Ar and 0.1% H₂ gas. Non-uniform distribution of the film thickness and resistivity was observed over a range covering up to 3 inch away from the center point under the target. It is found that the center point has the lowest film thickness and highest resistivity. The difference between the highest and lowest resistivity is within a factor of two for freshly deposited films. This result is helpful for determining the feasibility of large area AZO coating using this equipment for large size solar module applications.

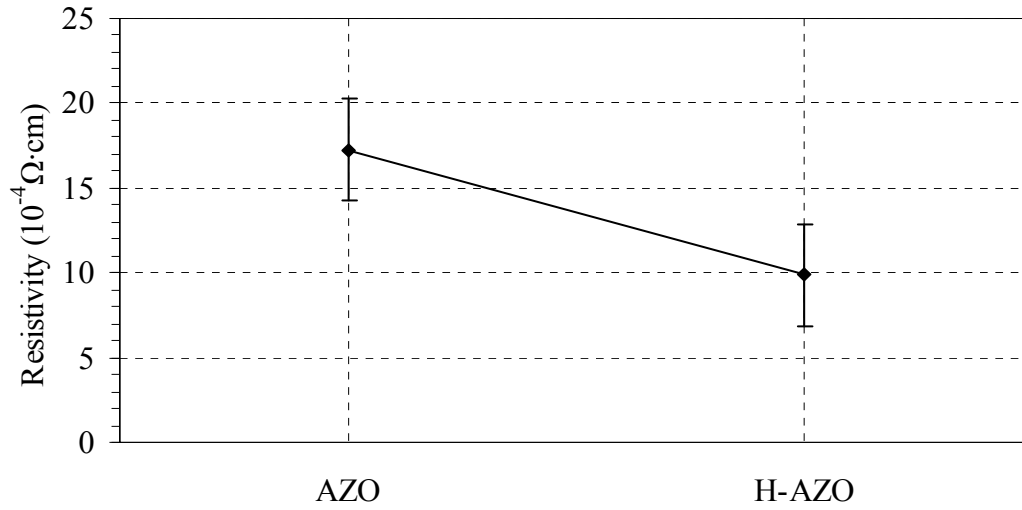


Figure 5-1. Effect of injecting hydrogen gas on the resistivity of sputtered AZO films.

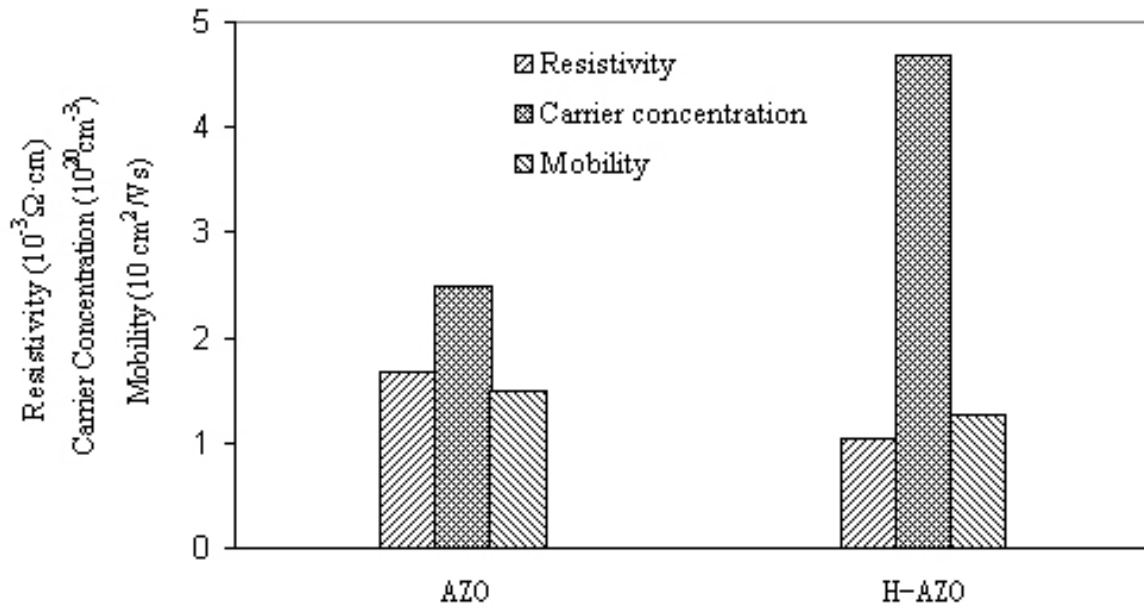
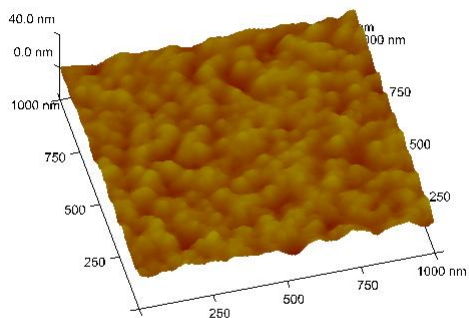
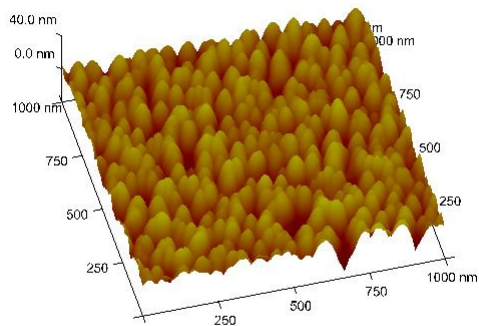


Figure 5-2. Hall measurement results for aluminum-zinc-oxide thin films deposited using only argon as the working gas (sample labeled as AZO) and using a mixture of argon with 0.1 wt% of hydrogen (sampled labeled H-AZO).

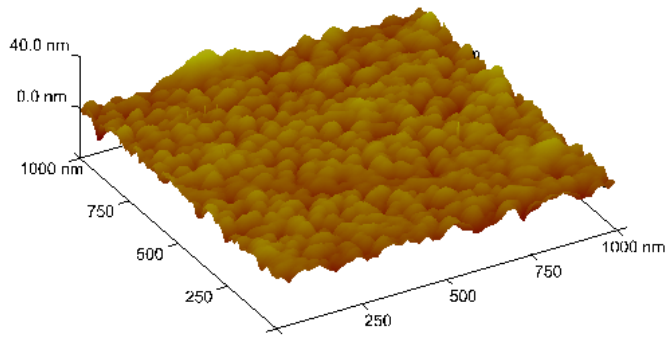


a)

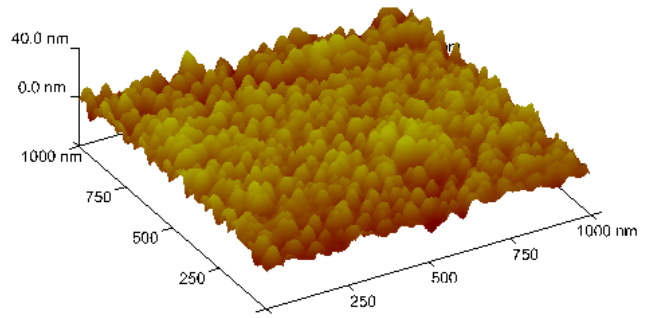


b)

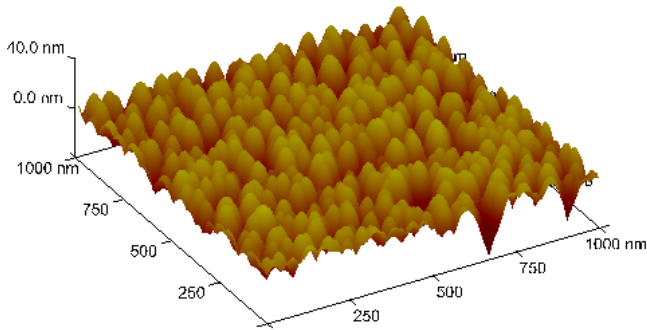
Figure 5-3. AFM image of two AZO films deposited using different sputtering gas. a) AZO b) H-AZO



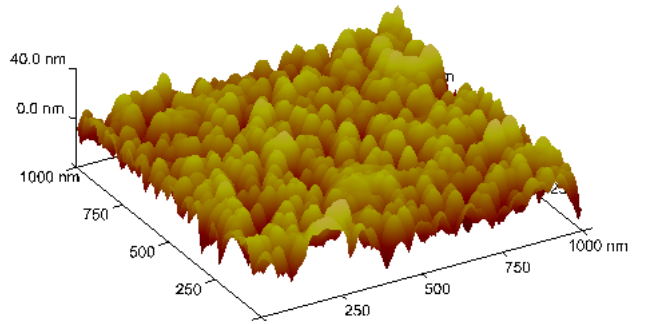
a)



b)



c)



d)

Figure 5-4. AFM image of H-AZO thin films with increasing thickness. a)200nm b)400nm c)600nm d)800nm

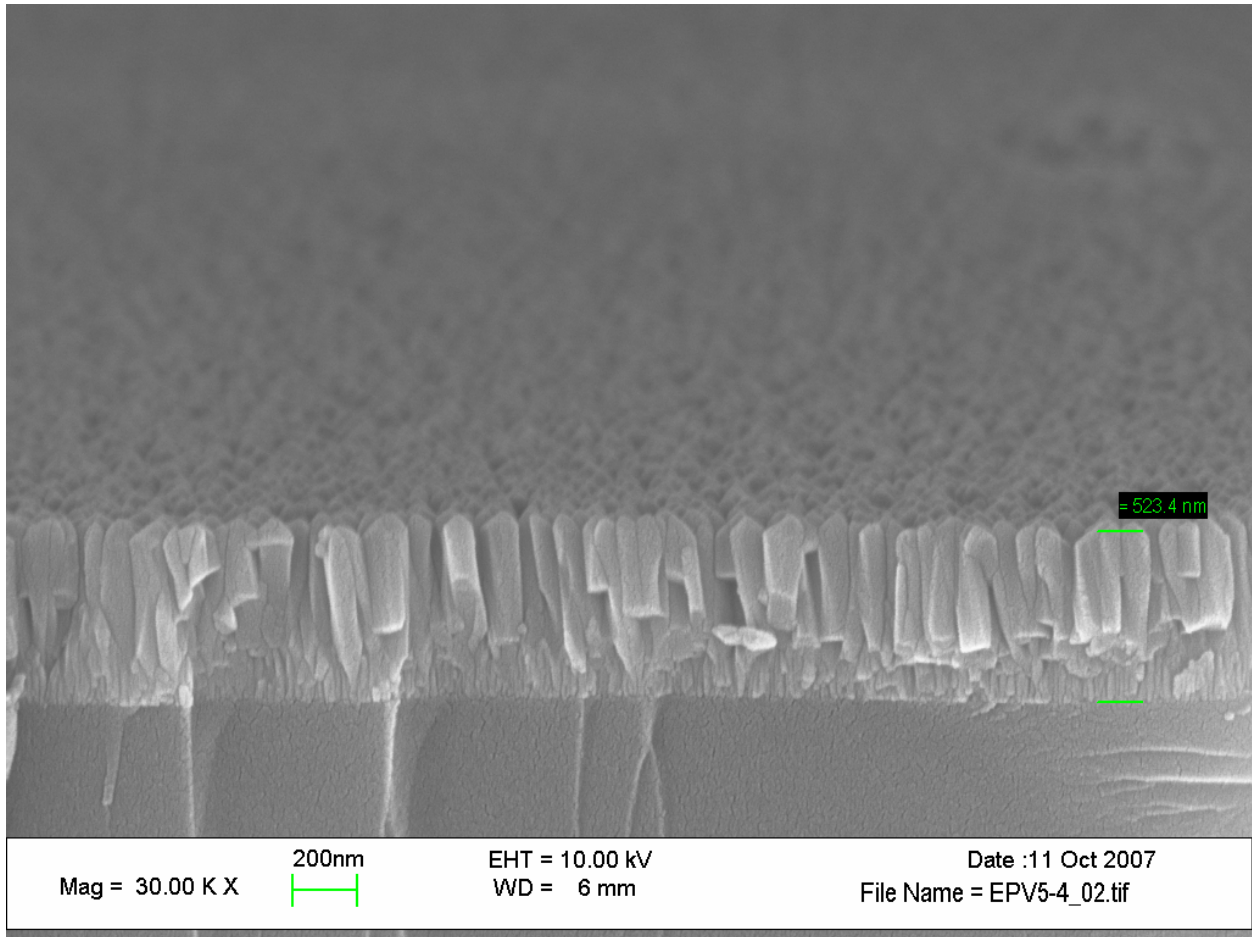


Figure 5-5. Cross-section SEM image of H-AZO thin films grown on i-ZnO substrate showing large column shaped grain structure.

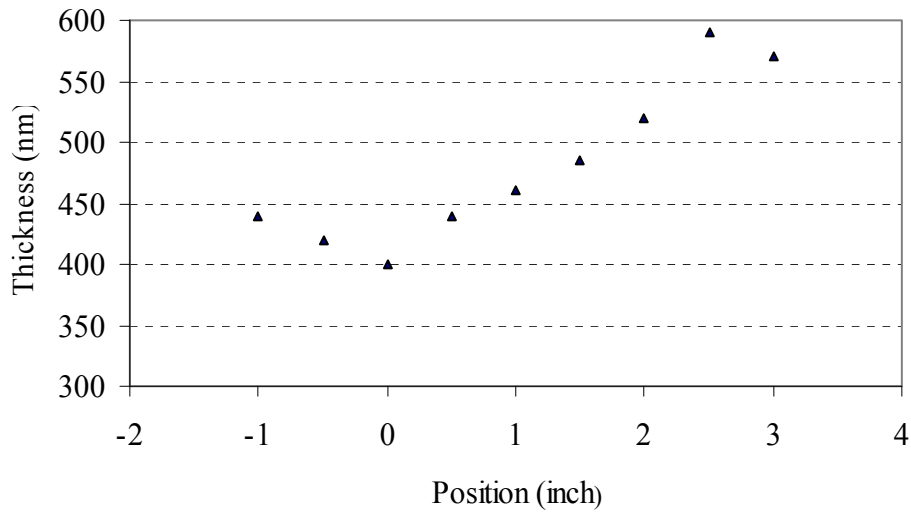


Figure 5-6. Variation of AZO thickness with different positions along the axial direction.

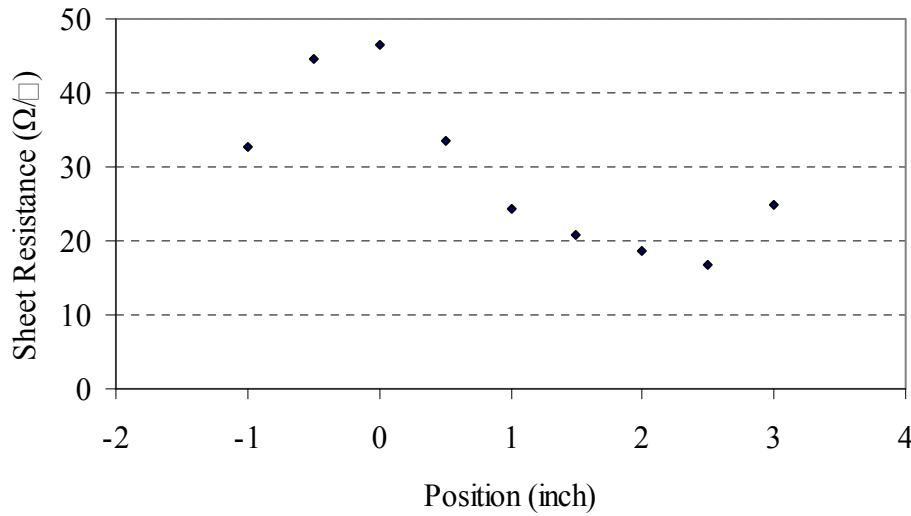


Figure 5-7. Variation of sheet resistance with different positions along the axial direction.

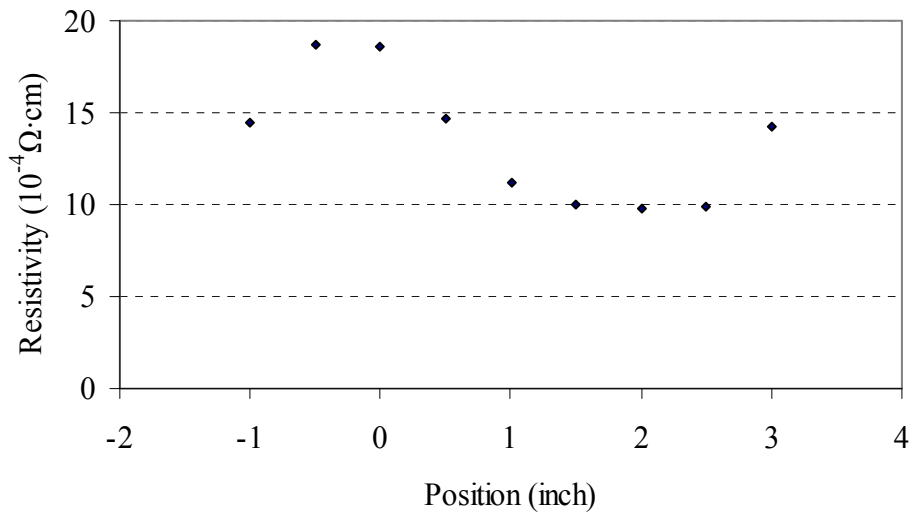


Figure 5-8. Variation of resistivity with different positions along the axial direction.

Table 5-1. Growth parameters comparison for AZO and H-AZO thin films.

Film composition	Base pressure	Working pressure	Power density	Sputtering gas
AZO	1.0×10^{-6} Torr	4 mTorr	350W	Ar only
H-AZO	1.0×10^{-6} Torr	4 mTorr	350W	Ar + 0.1% H ₂

Table 5-2. Deposition condition comparison between two AZO thin films shown in Figure 5-5.

Film	Power	Working pressure	Deposition duration
AZO	350 W	4mTorr	30min
H-AZO	350 W	4mTorr	30min

Table 5-3. Thickness, R_q and estimated grain size comparison between two AZO thin films shown in Figure 5-5.

Film	Thickness	R _q	R _a
AZO	~600 nm	2.89 nm	2.34 nm
H-AZO	~600 nm	5.85 nm	4.63 nm

Table 5-4. Roughness data evolution with increasing film thickness.

Thickness	R _q	R _a
~200 nm	2.38 nm	1.89 nm
~400 nm	4.15 nm	3.38 nm
~600 nm	5.85 nm	4.63 nm
~800 nm	8.18 nm	6.51 nm

Table 5-5. Hall measurements results on two films with different positions under the target.

Position	Carrier concentration	Hall mobility	Resistivity
center	6.5×10^{20} (cm ⁻³)	4.79cm ² /(V·s)	2.00×10^{-3} Ω·cm
2.5 inch from the center	4.3×10^{20} (cm ⁻³)	14.2cm ² /(V·s)	1.03×10^{-3} Ω·cm

Table 5-6. Comparison of Hall and four-point-probe measurement results.

Position	Resistivity obtained from Hall measurement	Resistivity obtained from four-point-probe measurement
center	2.00×10^{-3} Ω·cm	1.86×10^{-3} Ω·cm
2.5 inch from the center	1.03×10^{-3} Ω·cm	9.74×10^{-4} Ω·cm

CHAPTER 6 DEVICE FABRICATION AND CHARACTERIZATION

Device Fabrication Procedure

Substrate

The fabrication of CIGS solar cells starts from choosing the right substrate. Soda-lime glass (SLG) is generally preferred due to its chemical inactivity, thermal stability, and vacuum compatibility. Soda-lime glass contains 15.6 wt % of sodium in the form of Na_2O . At the high processing temperatures used for absorber growth, soda-lime glass starts softening. The sodium ions can diffuse through the molybdenum back contact entering the absorber layer. It is also found that an optimum amount of diffused sodium is beneficial to improve the performance of the devices [64]. It is noteworthy that CIGS solar cells can also be fabricated on flexible substrates such as metal foil and polymer substrates. Sodium doping may be required to achieve high efficiency from devices fabricated on these sodium free substrates.

Back Contact Sputtering

Sputtering is generally used for coating the thin layer of molybdenum back contact. Molybdenum is chosen because it forms good ohmic contact with CIGS. It is resistant to react with the elements contained in CIGS, and stays stable in the highly corrosive Se vapor environment during the absorber growth. The working pressure used during sputtering of Mo is found to be related to the diffusivity of sodium. Increasing the sputtering pressure generally increases the amount of sodium that can diffuse through. Since there is an optimum amount of sodium diffusion for best device performance, the Mo sputtering pressure needs to be adjusted well.

All the UF CIGS devices are fabricated on Mo coated soda-lime glass provided by Shell Solar Industries (SSI). Small amount of Mo was sputtered using the Perkin-Elmer system for

test purpose. For diode RF sputtering (non magnetron), with the uniformity shield blocking part of the flux, a growth rate between 10 to 15 nm/min can be achieved using 4mTorr working pressure and 400W deposition power. The substrate is heavily heated during sputtering and the substrate temperature is elevated beyond room temperature although the substrate platen is constantly cooled with chilled water. The resulted Mo film generally has good adhesion on soda-lime glass. Resistivity in the low $10^{-5}\Omega\cdot\text{cm}$ region was achieved on 150nm thick film.

Absorber Growth

The next step of fabrication is to deposit the CIGS layer. Vacuum processes are typically adopted for better device performance. Such vacuum processes are generally physical vapor depositions (PVD) including co-evaporation and sputtering [65,66]. The current champion CIGS devices are fabricated using absorber deposited through 3-stage process, which is basically a co-evaporation process [67]. Alternative pathways are selenization of metal precursors within a selenium environment [68-70]. Non-vacuum processes [71-73] are also reported to be feasible in producing the CIGS layer. The non-vacuum processes generally produce devices with less efficiency, but the production cost is lower than its vacuum counterparts. They could prove to be a promising way of producing low cost solar cells for terrestrial applications.

Here in the University of Florida, the CIGS layer is deposited using a Plasma Migration Enhanced Epitaxy (PMEE) system [74,75]. Figure 2-1 shows a schematic of the PMEE reactor. The system is a variant of traditional Molecular Beam Epitaxy (MBE) system. The substrate is put on a rotating platen and it sequentially passes under each source. The metal components, i.e., copper, indium, gallium are sequentially deposited during the exposure. The substrate then rotates into the selenium zone and encounters a surplus of selenium vapor. At the high substrate temperature (up to 490°C) used during the deposition, the components reacts and polycrystalline

CIGS is formed. The substrate is only exposed to each source once during every rotation cycle and the system has a very low throughput compared with other PVD processes such as co-evaporation. It is not economical for large scale production using the system but the epitaxial ability makes the system potentially capable for exploration into the single crystal regime. Single crystal growth of CIGS can be performed on GaAs substrates.

Buffer Layer Deposition

Following the absorber layer is the deposition of buffer layer. A wet chemical process called chemical bath deposition (CBD) was utilized to deposit a thin layer of n-type buffer layer on top of CIGS. CBD is a technique of controlled precipitation of a compound from its aqueous solution. It is a relatively economic way to deposit thin films because no vacuum or high temperature is required.

Traditional buffer layer for CIGS solar cell is cadmium sulfide (CdS). For CdS deposition, solutions containing certain concentrations of ammonia hydroxide, CdSO₄ and thiourea are mixed in a water circulated 1 Liter jacket beaker and reaction took place in a controlled batch under a preferred temperature of 65°C. CdS with approximately 50nm thickness is deposited on to the surface of the substrate during a 15minute deposition time. Table 6-1 shows detailed recipe for traditional CBD deposition of CdS buffer layer.

Due to the toxic nature of Cd, there have been efforts to remove or at least reduce the toxic cadmium component and produce more environmentally friendly CIGS solar cells. For the result presented in this dissertation, an alternative buffer layer of Cd_{1-x}Zn_xS was used. The targeted stoichiometry is a ratio between Cd and Zn as 7:3, which gives a good device performance [76]. The recipe used is similar to that in a patent from Beoing company [77]. It is basically an aqueous solution contains CdCl₂ 2(1/2)H₂O, NH₄Cl, thiourea (H₂NCSNH₂), ZnCl₂, and NH₄OH

was used for the UF CBD deposition. Detailed concentration of each ingredient is documented in Table 6-2.

The chemical bath is formed in a 1 liter jacket beaker heated by circulating hot water and the temperature is maintained at a target of 85 °C at all times during film growth. The bath is vigorously stirred and typical deposition duration is 45min, which gives a film thickness of approximately 50nm.

Window Layer Deposition

After depositing the buffer layer, an intrinsic ZnO and an Al doped ZnO (AZO) layer are sequentially deposited using a Perkin Elmer 4400 sputtering system. Details of the sputtering system are introduced in Chapter 3. It is known that both the optical transmission and electrical resistance of the window layer have strong impact on the performance of CIGS solar cells. The transmission determines the amount photons entering the absorber layer while the resistance is related with the series resistance of the device. Both of these factors are associated with window layer thickness in a conflicting way. Decreasing ZnO thickness would help to improve transmission but it also causes the increase of sheet resistance, which may result a deterioration of device performance. Therefore, the thickness of the AZO layer is adjusted to obtain a desirable sheet resistance while maintaining a reasonable optical transmission.

The intrinsic ZnO layer is deposited from a fully oxidized target and the growth rate is low. It will dramatically improve the throughput if this layer can be omitted. Ramanathan *et al.* [78] reported that the conversion efficiency of CIGS solar cell does not change using a simplified device structure without the intrinsic ZnO layer. This could be a major simplification of the fabrication process and could significantly reduce the cost and turn around time. However, there is contradictory report from Ishizuka *et al.* [79] showing different intrinsic ZnO thickness would

affect the performance of CIGS solar cell. An investigation on this issue is addressed in the work of this dissertation.

Metallization

To finish up the device, a dual metal layer contact grid consisting of nickel and aluminum is deposited onto ZnO:Al. A shadow mask is used to define the contact finger pattern. Nickel acts as a diffusion barrier to keep aluminum oxide from entering the zinc oxide layer. The high melting temperature of Nickel is out of the reach of typical thermal evaporators and makes it necessary to use e-beam evaporation. The thickness of Ni and Al are 50nm and 1 μ m respectively. The grid coverage should be small (approximately 5%) to allow light passing. To improve the cell performance, an MgF₂ anti-reflection layer can be evaporated to reduce the light reflection and allow maximum amount of light entering the device. For all the results shown in the scope of this work, no anti-reflection layer was used. Figure 7-2 shows the photo of a CIGS device completed at the University of Florida.

Device Characterization System

The device current-voltage (I-V) measurement was conducted in our optoelectronic lab. The I-V system uses an ELH (tungsten-halogen) lamp with an integral dichroic rear reflector as the solar simulator. It is classified as a class C solar simulator due to a lack of energy below the wavelength of 0.5 μ m and excess energy in the wavelength between 0.6 and 0.7 μ m compared to AM1.5G radiation.

The radiation intensity from the solar simulator was calibrated using the reference cell method. Basically, a calibration cell with NREL certified characterization report was used as the reference cell to calibrate the system. This calibration cell, namely S2049-A1 fabricated in November of 2002, with a total cell area of 0.408 cm² was measured on 3/22/04 at NREL with

the following parameters for cell #2: $V_{oc} = 0.661$ V, $J_{sc} = 33.73$ mA/cm², FF = 77.47 %, and $\eta = 17.28$ %. The distance between the light source and the calibration cell was adjusted to obtain a calibrated position where the measured J_{sc} matches the certified J_{sc} value.

The temperature of the device tends to increase under elongated radiation from the solar simulator. Water cooling system and a thermal couple is embedded in the test stage to control the temperature. Efforts were made to maintain the temperature of the test cell at $25 \pm 1^\circ\text{C}$ during the characterization.

Devices with Absorbers from UF PMEE Reactor

Devices were first time completely fabricated in house. Two kinds of absorbers, namely CIGS and CGS, were grown in the UF PMEE reactor. These absorbers were etched in 10% potassium cyanide solution to remove any possible Cu rich phases before putting on the buffer layer. All the buffer layers are CdZnS approximately 50nm thick. No intrinsic ZnO was deposited so that the structure is simplified and fewer variables are involved. AZO window layer of approximately 600nm was deposited to ensure a sheet resistance well below $50\Omega/\square$, although later optimization on EPV absorbers indicates that thinner AZO layer would be sufficient and should have improved the performance of these devices.

CIGS Devices

For $\text{CuIn}_{1-x}\text{Ga}_x\text{Se}$, absorbers with different x value and different Cu to group III metal ratio were grown and devices were fabricated using the method described earlier. The substrate temperature during absorber growth was approximately 490°C . All metal fluxes were kept constant during the growth. Therefore there was no bandgap grading for these absorbers. Table 6-3 shows the film properties of the CIGS absorbers used for device fabrication. These are Cu

poor films with x values vary around 0.3. Film thickness is around 1 μm . Only one thick sample with thickness of 1.9 μm was grown due to the low throughput of the system.

The I-V properties of these CIGS devices were measured using the I-V system. The solar simulator intensity was calibrated using the reference cell before and after the lengthy measurement to ensure there is no major parameter drift during the process. The calibration cell performance parameter is the short circuit current. Table 6-4 shows the NREL certified parameters of cell #2 on S2049-A1 and the calibrated parameters of this cell before and after the measurement. It can be seen that the calibrated results are conservative to avoid an exaggeration of the device performance.

Table 6-5 lists the measured I-V character of the UF CIGS devices. Device 582, the CIGS with zero Ga content (essentially CuInSe_2), showed the highest efficiency of 8.9%. It had a relatively high open circuit voltage and the highest short circuit current among all the CIGS devices. The highest CIGS device, #588, has good short circuit current and fill factor, but the lower open circuit voltage compared with device 582 made its efficiency lower.

The two best performance absorbers were evaluated under high resolution scanning electron microscope. Figure 6-3 and Figure 6-4 are the cross-section SEM images of absorber #582 and #588 respectively. It can be seen that these two films have similar thickness. Both of these two absorbers have relatively large grain size, which is important for high performance.

CGS Devices

High efficiency CuGaSe_2 devices are required as the top cell for high performance tandem chalcopyrite structure. Currently the efficiency of CGS is lagging far behind that of CIGS [80]. Much still needs to be done to improve the efficiency of CGS devices.

Some devices using CGS grown from the PMEE reactor were fabricated. The CGS growth parameters are shown in Table 6-6. Generally, two growth recipes were involved in producing these CGS absorbers. One recipe is an emulated NREL 3-stage growth process trying to create bandgap grading within the absorber layer. The other recipe uses constant metal flux to obtain a uniform band structure in the CGS thin films. All of these films were Ga rich with copper to gallium ratio varied slightly between 0.91 and 0.95. Table 6-7 shows the device performances of these CGS films. The highest efficiency of 4.9% was achieved on Device 640 grown via the emulated 3-stage process.

Cross-section SEM image was taken on the UF champion CIGS device and the result is shown in Figure 6-5. Each layer constituting the device can be clearly seen except there is no significant boundary between the CdS and ZnO layers. This device has a fairly thick absorber with large grain size in the order of microns. Good attachment between the absorber and the underneath Mo layer indicating a good stress control on the relatively thin Mo back contact.

Effect of Zinc Oxide Window Layer on Device Performance

CIGS devices are also fabricated using the absorbers provided by Energy Photovoltaics Inc. These absorbers are grown on large sheet of substrates then cut into smaller 2"×2" pieces and shipped from EPV to UF. Therefore, it is reasonable to assume that the absorber layer has similar performance and can be used for the window layer optimization. The effect of optical transmission and sheet resistance of the AZO layer was investigated. Another issue addressed is the effect of the intrinsic ZnO layer.

For experiments conducted to investigate the transmission and sheet resistance, only the AZO thin film layer was deposited and the intrinsic ZnO layer was skipped. Doing so would

simplify the solar cell structure and the fabrication process, reduce the possibility of effects brought in by an extra step and thus focus on the issue under investigation.

The impact of intrinsic ZnO layer on solar cell performance was then assessed. The motivation is to evaluate the necessity of this intrinsic ZnO layer. The deposition rate for this layer is generally low because it is sputtered from a fully oxidized target. Although only a very thin layer of intrinsic ZnO is required, it generally consumes comparable time as that for sputtering the AZO layer due to the much smaller deposition rate. If this layer can be proved to be unnecessary, it would significantly reduce the complication of the fabrication process and greatly improve the process throughput. In literature there are contradictory reports regarding to the effect of this layer and further investigation needs to be conducted. Devices fabricated with and without the intrinsic ZnO layer are compared and the results were analyzed.

Effect of Window Layer Transmission

The AZO transmission experiments were conducted using CIGS absorbers from EPV. Efforts were made trying to eliminate the possible variations coming from other layers. These include cutting the absorbers off from the same 2''×2'' CIGS substrate and depositing the ZnCdS buffer layer during the same batch of CBD process. A 2''×2'' substrate was cut into four 1''×1'' pieces and three of them were then coated with buffer layer during one single batch of bath deposition. The maximum number of substrates can be processed in one batch of CBD deposition is three due to the number of substrate holders available. The recipe used was targeted to a stoichiometry of $Cd_{1-x}Zn_xS$ with x equals 0.3. AZO thin films with different optical transmission were then deposited on top of the buffer layer. A dummy glass was placed beside each sample to monitor the optical transmission and sheet resistance. Finally, the metal top contact fingers are evaporated to finish the device.

Figure 6-6 shows the window layer optical transmission of the three aforementioned CIGS devices. For easy comparison, the transmission is categorized into three levels: low, medium and high. The current-voltage (I-V) properties of these solar cells were characterized and important device parameters are listed in Table 6-8. The results showed that by increasing the window layer optical transmission, both the open circuit voltage (V_{oc}) and short circuit current (J_{sc}) were increased. The V_{oc} improved from 0.436V to 0.477V and J_{sc} increased from 24.12mA/cm² to 27.50mA/cm² when the transmission improved from low to high region. As a result, the solar cell efficiency was improved from 4.59% for a low transmission window to 6.21% for a high transmission window. This is approximately 35% improvement of the efficiency.

The results from AZO transmission experiments showed that the window layer optical property is critical to solar cell performance. It is a very effective way to improve CIGS solar cell performance by enhancing the optical transmission of the AZO window layer. It is also known that improvement of transmission by applying MgF₂ antireflection layer can further increase the device performance.

Effect of Sheet Resistance

As mentioned before, the sheet resistance affects the series resistance of a solar cell and according the theory showed in Chapter2, it would affect the performance of a device. To evaluate this effect, a number of devices with various sheet resistances were fabricated on CIGS provided by EPV and the device performance was evaluated via I-V measurement.

Figure 6-7 shows the relationship between AZO layer sheet resistance and CIGS solar cell efficiency. Many data points were taken around 50Ω-cm region, a value adopted by literature report[81]. But exploration of sheet resistance to regions much higher than this value also

yielded devices with good efficiency. Generally, the device performance is very tolerant to sheet resistance over a fairly large range. Reasonable performance was obtained from devices with window layer as thin as 100nm.

A good tolerance to sheet resistance yet being sensitive to transmission indicate device performance can be improved by reducing the window layer thickness to achieve better transmission while maintaining a reasonable sheet resistance. Since many factors coming from different layers of the device can affect the efficiency, it is difficult to perform an optimization with limited amount of EPV absorbers available. Indeed, there is no straight forward trend observed from these performance data.

Impact of the Intrinsic ZnO Layer

Three pairs of devices were fabricated using CIGS from EPV to evaluate the effect of the intrinsic ZnO layer. Within each pair, one device is fabricated with the intrinsic ZnO layer and the other without. These devices were characterized using I-V measurement system and the result is shown in Table 6-9. It is evident that devices with the intrinsic ZnO layer unanimously showed an improvement of V_{oc} . The J_{sc} value is also higher for the devices with the intrinsic ZnO layer compared to its counterpart, with the first pair having very close J_{sc} values though. As the result, all devices with the intrinsic ZnO layer showed improved efficiency.

These data show that intrinsic ZnO is necessary in terms of achieving high efficiency, at least for the case of EPV absorbers. But from the standpoint of industry manufacturing, this improvement has to be balanced with the cost of an extra step of deposition. A careful evaluation of the benefit and cost need to be made. This is out of the scope of this dissertation.

Summary

Devices were fabricated using UF CIGS and CGS absorbers. Reasonable performance was achieved on these devices indicating device quality ZnO has been achieved. Further

optimization of the window layer to improve device performance was conducted using EPV absorbers. Results showed that the devices are tolerant to the sheet resistance over a large range. Optical transmission plays a more direct role affecting the efficiency. Device efficiency can be increased by using thinner ZnO as the window layer. The necessity of the intrinsic ZnO layer was investigated. The results showed that this layer is beneficial to improve the device efficiency. It is necessary to have this layer to achieve best efficiency devices.

Table 6-1. Recipe for CdS buffer layer deposition.

Constitute	Concentration	Volume
DI water	N/A	365mL
Thiourea	1.5mol/L	25mL
Ammonia hydroxide	28.0-30.0wt%	62.5mL
CdSO ₄	0.015mol/L	50mL

Table 6-2. Recipe for CdS buffer layer deposition.

Constitute	Concentration	Volume
DI water	N/A	490mL
Thiourea	0.0834mol/L	100mL
Ammonia hydroxide	3.5-3.75wt%	0.25mL
ZnCl ₂	0.254mol/L	1.4mL
CdCl ₂ 2.5H ₂ O	0.0084mol/L	121.9mL

Table 6-3. Composition and thickness data for UF CIGS absorbers.

Film ID	Cu/III ratio	Ga/(In+Ga) ratio	Thickness (μm)
569	0.97	0.30	0.8
575	0.97	0.33	0.85
578	0.97	0.32	1.3
579	1.00	0.30	1.9
582	0.91	0	1.0
586	0.90	0.25	0.9
587	0.99	0.41	0.85
588	0.98	0.21	0.9

Table 6-4. Calibration of the reference cell.

Data Source	V _{OC} (V)	J _{SC} (mA/cm ²)	FF (%)	Eff. (%)
NREL certified value	0.661	33.73	77.47	17.28
Calibration result before measurement	0.642	33.62	76.09	16.42
Calibration result after measurement	0.643	33.56	76.24	16.24

Table 6-5. I-V character of the UF CIGS devices.

Device ID	V _{OC} (V)	J _{SC} (mA/cm ²)	FF (%)	Eff. (%)
569	0.457	24.3	39.4	4.4
575	0.476	26.3	55.5	7.0
578	0.325	26.6	34.2	3.0
582	0.457	30.5	64.0	8.9
586	0.317	21.3	26.8	1.8
587	0.308	18.1	41.7	2.3
588	0.437	29.3	67.0	8.6

Note: Device 579 gave no I-V characteristics

Table 6-6. Growth recipe and composition for UF CGS absorbers.

Film ID	Process	Cu/Ga ratio
640	3-stage	0.91
647	Constant flux	0.92
649	3-stage	0.95
655	Constant flux	0.95

Table 6-7. I-V character of the UF CGS devices.

Device ID	V _{OC} (V)	J _{SC} (mA/cm ²)	FF (%)	Efficiency (%)
640	0.502	16.9	57.4	4.9
647	0.480	13.7	55.7	3.7
649	0.426	16.8	46.3	3.3
655	0.516	14.2	57.8	4.2

Table 6-8. Performance of CIGS solar cells with different window layer transmission.

Device ID	Transmission	V _{oc} (V)	J _{sc} (mA/cm ²)	FF(%)	Efficiency (%)
EPV5-2	Low	0.436	24.12	43.65	4.59
EPV5-1	Medium	0.467	25.79	47.89	5.77
EPV5-3	High	0.477	27.50	47.35	6.21

Table 6-9. Performance of CIGS solar cells with and without i-ZnO layer

Pair number	Device ID	i-ZnO	V _{oc} (V)	J _{sc} (mA/cm ²)	FF(%)	Efficiency (%)
Pair 1	EPV3-1	Yes	0.536	29.64	47.18	7.49
	EPV2-2	No	0.488	29.58	47.00	6.78
Pair 2	EPV5-4	Yes	0.494	26.78	45.51	6.02
	EPV5-1	No	0.467	25.79	47.89	5.77
Pair 3	EPV 6-1	Yes	0.498	28.75	50.63	7.25
	EPV 5-3	No	0.477	27.50	47.35	6.21

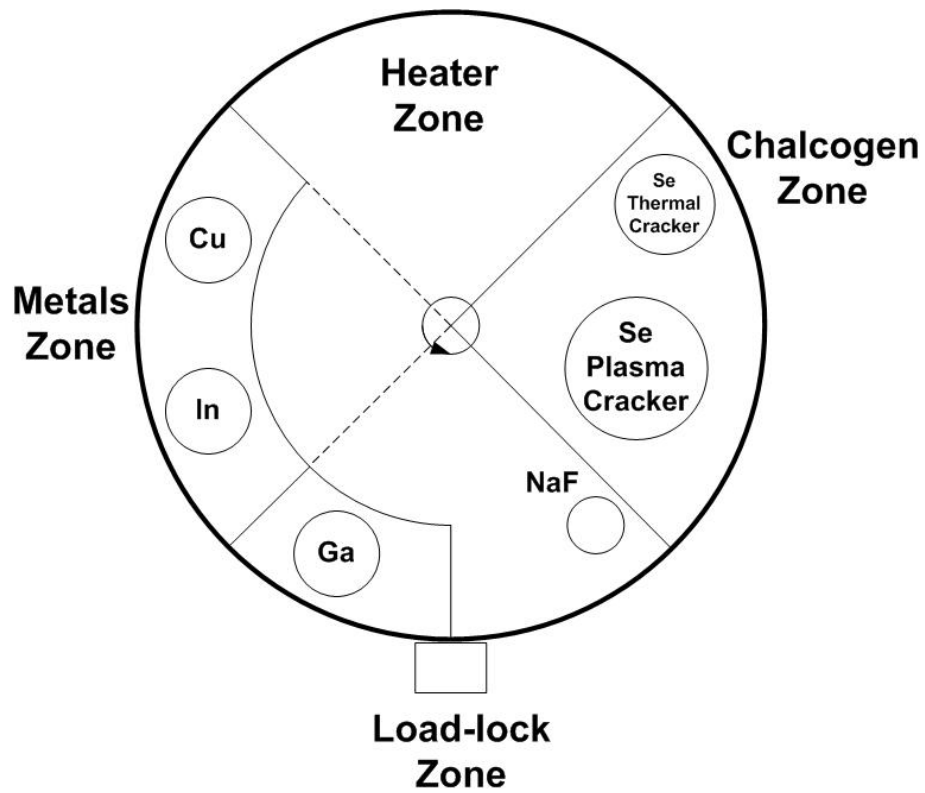


Figure 6-1. Schematic of the PMEE reactor.

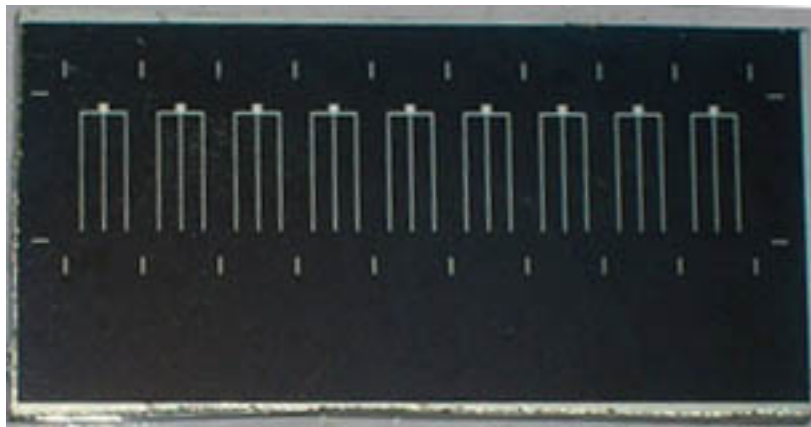


Figure 6-2. Photo of CIGS solar cells fabricated on a 2"×1" soda-lime glass substrate.

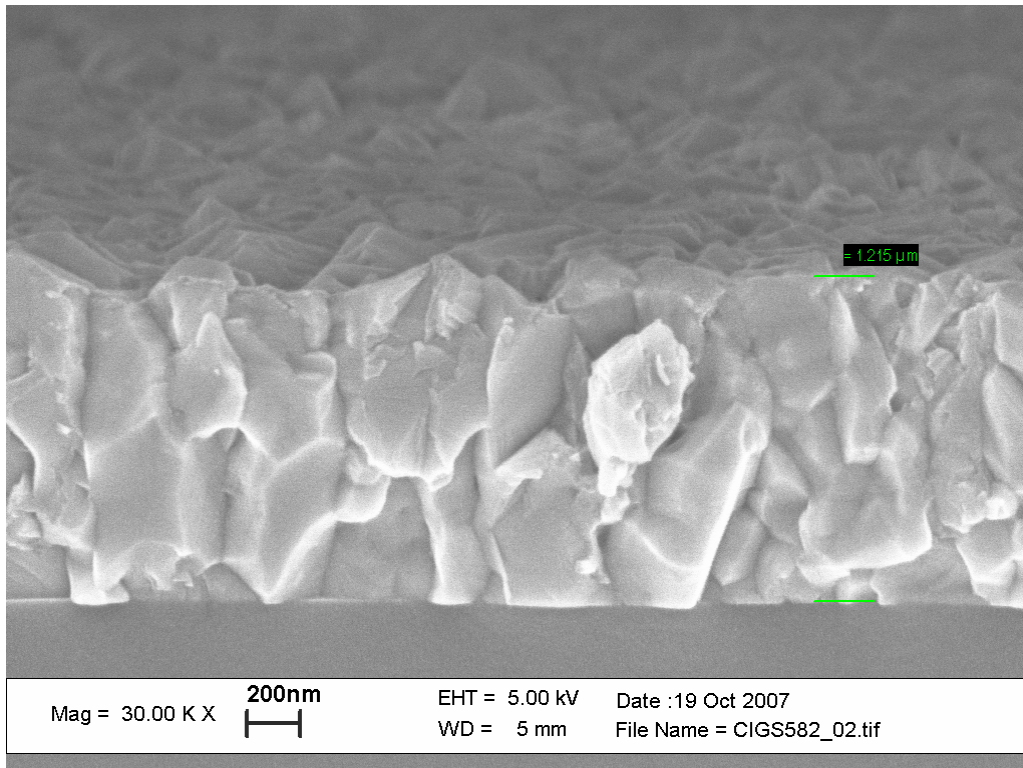


Figure 6-3. Cross section SEM image of absorber #582.

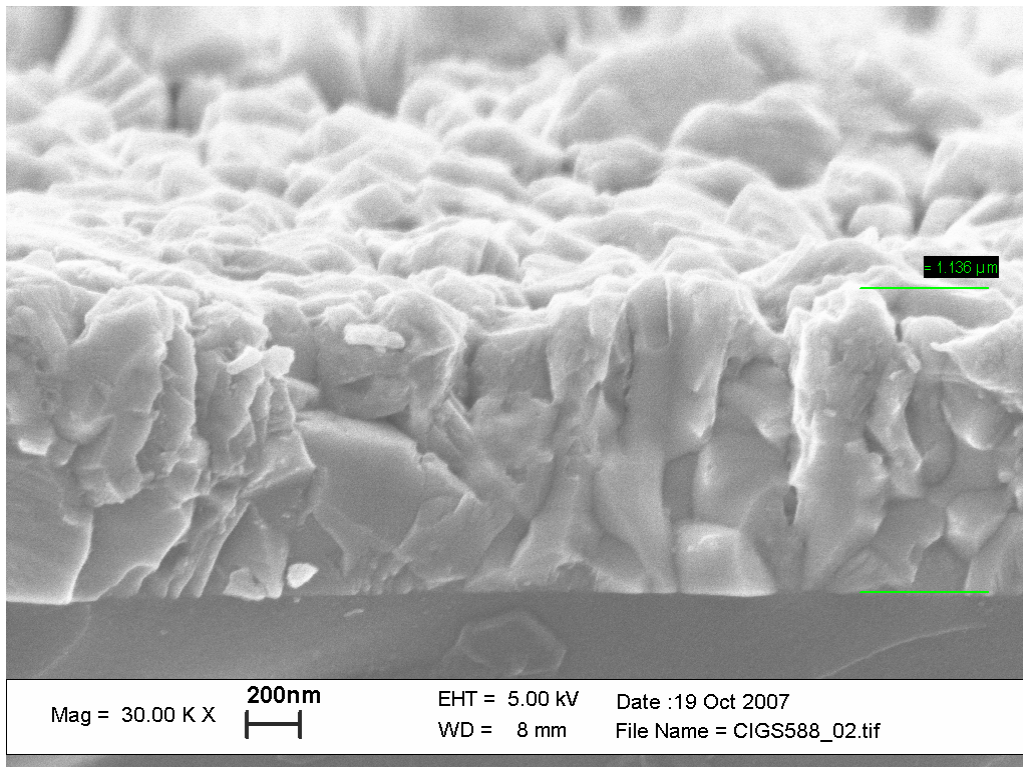


Figure 6-4. Cross-section SEM image of absorber #588.

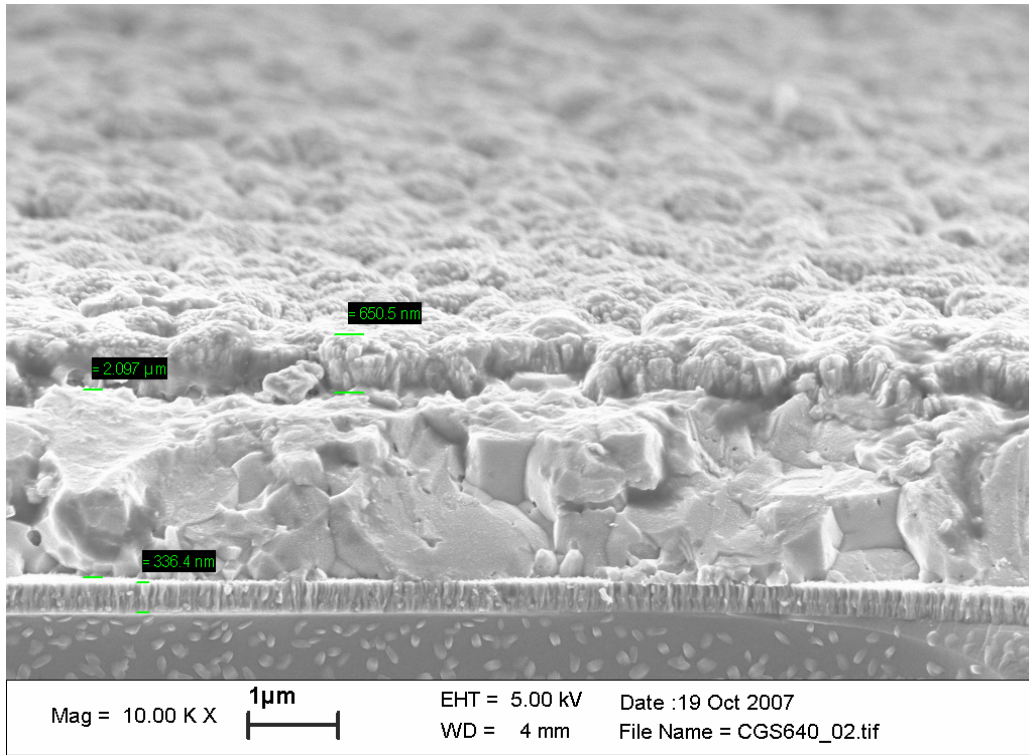


Figure 6-5. Cross-section SEM image of CGS device #640.

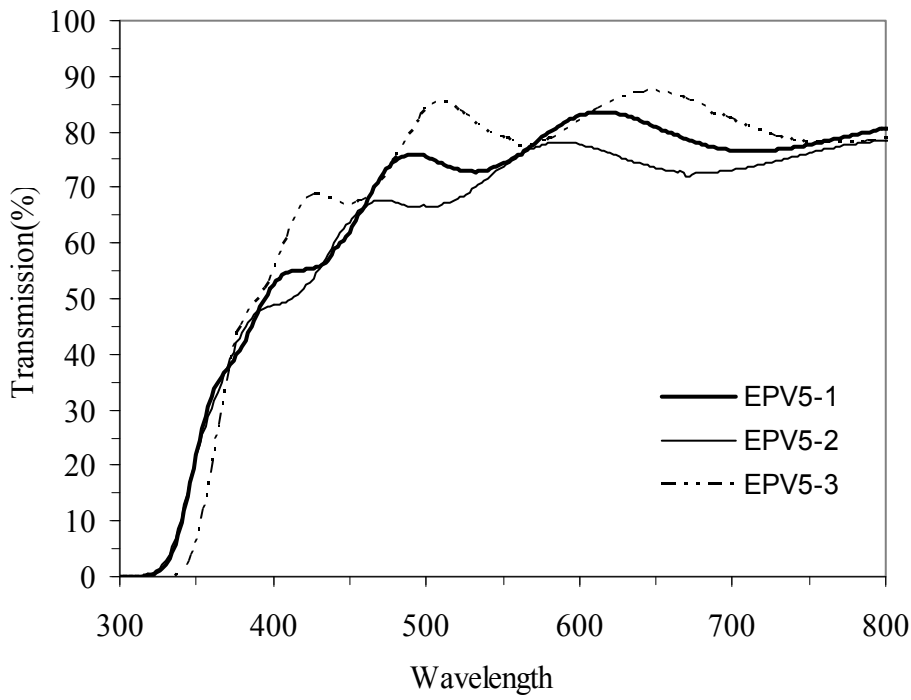


Figure 6-6. AZO window layer optical transmission of three CIGS solar cells.

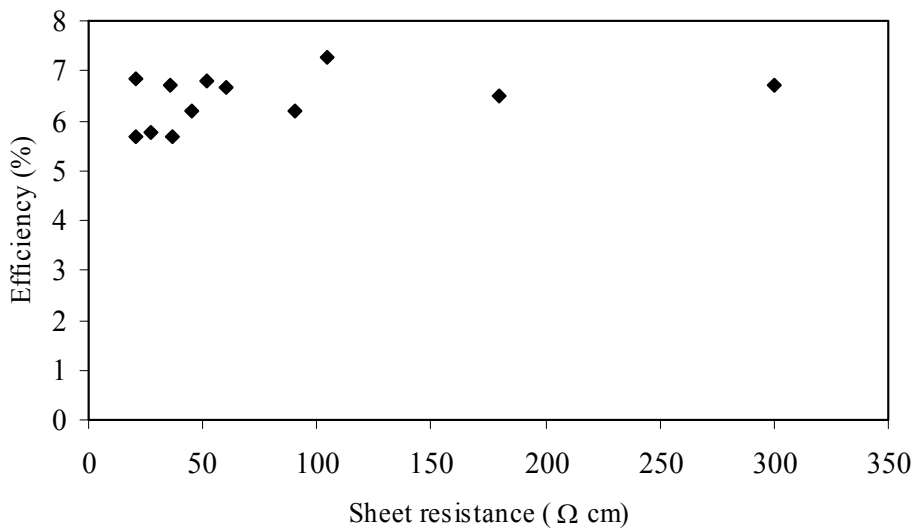


Figure 6-7. CIGS cell efficiency versus the AZO layer sheet resistance.

CHAPTER 7 INVERSE MODELING OF CIGS SOLAR CELLS

CIGS solar cell structure consists of several layers of compound semiconductors.

Although today's material characterization techniques are highly advanced, there is still much information remains unknown. For example, the defect distribution within the CIGS layer has a fundamental impact on the behavior of the absorber layer and it is critical to determine the cell conversion efficiency. The work shown in this section is dedicated to develop a convenient way of identifying some of the key unknown factors through numerical simulation. The idea is to construct an inverse problem and solve the unknown parameters through inverse modeling. Details of the procedure are addressed in the following sections.

Definition of Inverse Modeling

This section proposes a definition of *inverse modeling*, the process of solving an inverse problem. Let a physical system under study be denoted by S. The scientific analysis of system S can be divided into the following three aspects:

- (i) *Parameterization of the system*: specification of a minimal set of model parameters whose values completely characterize the system.
- (ii) *Forward modeling*: use of the physical laws to make predictions on some observable parameters (output values) basing on some input values.
- (iii) *Inverse modeling*: use of the actual results of some measurements of the observable parameters (output values) to infer the actual values of the model parameters.

Strong feedback exists among these three steps and a dramatic advance in one of them is usually followed by the other two [20].

A schematic description of the three components discussed above is given in Figure 7-1, which shows a system S with known parameters. The process of feeding through input values to derive output values is called forward modeling. The process of finding the input values that yield given output values is called inverse modeling. A special case of inverse modeling is

system identification, where both input values and output values are known, and the objective is to determine the parameters of system S.

Inverse Modeling for Photovoltaic Cells

Applying the three steps defined previously to the case of solar cell, the solar cell system can be analyzed under the following perspectives:

(i) *Parameterization of the system*

Examples of input and output parameters of a solar cell system are shown in Figure 7-2. The input parameters include cell configuration parameters and material properties parameters. The output parameters may include the open circuit voltage, short circuit current, fill factor, and energy conversion efficiency.

(ii) *Forward Modeling*

The physical laws followed in the forward process are the various physical models used in the device simulation software, such as Medici [21]. Basically, the input parameters are provided to Medici by the user, and the software does the calculation to predict the values of the output parameters of interest.

(iii) *Inverse Modeling*

Based on specified values of cell performance parameters (output values), such as cell efficiency, the inverse modeling method seeks to find the values of a set of input parameters that yield the given output values. It should be noted that for the solar cell case, it is believed that for certain efficiency, there may be more than one set of input parameters which yield the same efficiency value. In other words, different combinations of the input parameters may result in the same output parameter value.

Application of Inverse Modeling — Performance Optimization

Numerical simulation has been adapted to optimize the performance of CIGS solar cells [22], but a comprehensive study is far from complete. We hope to obtain better understanding and optimization by using inverse modeling.

An extension of inverse modeling is the endeavor to optimize key performance parameters, such as cell efficiency, to find a set of input parameters that generate the highest possible cell efficiency. This is extremely attractive because improving the cell efficiency has always been the most challenging task for the Photovoltaic community.

Approach

The inverse problem for solar cell proposed in this work consists of integrating Matlab [23] and Medici. Matlab is responsible for the parameter analysis and for providing the optimization algorithm. Medici is used to carry out the forward modeling part, and to predict the values of the output parameters.

The flow chart shown in Figure 7-3 describes the procedure for solving the inverse problem. The inverse modeling algorithm is comprised of all the steps between the Start and Stop indicators in the flow chart. The user must first specify the target output parameters. Then the user specifies an initial guess for the input values. At this point, an iteration procedure is initiated by Matlab, by feeding the input values to the Medici program. In the next step, Medici predicts the corresponding output value for the Matlab-specified parameters.

At the beginning, a set of initial attempted parameters such as defect energy distribution and concentration were input to Matlab. Then Matlab send this set of parameters to Medici. Medici will proceed to do the forward modeling and generate the criteria parameters such as open circuit voltage (V_{oc}), short circuit current (I_{sc}) and fill factor (FF). Then values of these criteria parameters were sent back to Matlab, where they were compared with the set value. If

the difference between the generated values and the set values is smaller than a tolerated value (usually a very small value), the inverse process stops and the set of input parameters that will yield the wanted criteria parameters are found. Otherwise, when there is still a significant difference between the generated values and the set values, Matlab will generate a new set of input parameters according the Algorithm used, and send them back to Medici and the process is repeated until the generated values fit the set values.

The process can be easily adapted to optimize arbitrary output values, such as V_{oc} , I_{sc} , FF and cell efficiency. The process stops once the optimized parameter reaches its optimum value. For the efficiency case, the process proceeds until the maximum cell efficiency is found.

Forward Modeling

This section describes details of utilizing Medici for the forward modeling. Cell structure is first built in Medici by defining each layer of the device. Then relevant input values for each layer is assigned to describe the properties of these layers. Some examples of the input values are listed.

Cell structure generation

The cell structure used in the forward modeling is shown in Figure 7-4. At the bottom is a layer of Molybdenum on top of a glass substrate serving as the ohmic contact for the p type Copper Indium Gallium di-Selenide ($\text{CuIn}_x\text{Ga}_{1-x}\text{Se}_2$ or simply CIGS). Next is the absorber layer p type CIGS. The typical thickness for the CIGS layer is about 2 microns so as to completely absorb the incoming sun light. The OVC (ordered vacancy compound) layer is not intentionally deposited. It is an indium rich n-type layer formed between the p-type CIGS and the n-type CdS. The existence of this layer was initially suggested by Schimid *et al.* [24]. The CdS buffer layer is deposited through Chemical Bath Deposition (CBD). On top of CdS, a thin layer of intrinsic ZnO (i-ZnO) is deposited typically by sputtering. Finally, the top of the structure consists of a

layer of Transparent Conductive Oxide (TCO) in the form of heavily Al-doped ZnO, which forms ohmic contact with an Aluminum grid (not shown in the figure) that completes the device.

The software Medici uses a mesh concept to describe the property distribution inside the simulated device. It does calculation at each mesh node and then combines these results to form a whole structure view of the complete device. The CIGS cell structure of Figure 7-4 should be first described using mesh concept in order for Medici to proceed with the calculation. As shown in Figure 7-5, the graph on the left shows the mesh generated in Medici and the graph on the right shows each layer. Starting from the bottom to the top, the successive layers are CIGS, OVC, CdS, i-ZnO and Al doped ZnO.

Input parameters

The simulation temperature is kept at 300K in all cases considered, and the input solar spectrum was introduced from the “AM0.dat” file provided by Medici. This spectrum generates an input energy density of approximately 100 mW/cm^2 .

Some of the important parameters used in the simulation are shown in Table 7-1. The values of these parameters are consistent with the values used in the simulation based on the widely used solar cell simulation software AMPS1D [25].

With all the materials parameters defined in Medici, the bandgap profile can be generated. An example is shown in Figure 7-6. The layers can be seen in the bandgap profile from left to right are Al-ZnO, i-ZnO, CdS, OVC, and CIGS. Graded CIGS bandgap profile can also be achieved by defining more than one layer of CIGS with different bandgap values.

Example of a forward modeling

Figure 7-7 shows a typical I-V curve generated by Medici. The input parameters were taken from Table 7-1. Several important device performance parameters can be extracted from

the I-V curve. They are short circuit current (I_{sc}), open circuit voltage (V_{oc}), fill factor (FF) and efficiency (η).

The short circuit current I_{sc} is defined as the current value at the spot where the I-V curve crosses the vertical axis [7]. From the graph it can be seen that the I_{sc} value is approximately 37 mA/cm². The open circuit voltage V_{oc} is the voltage value at the spot where the I-V curve crosses the horizontal axis. Hence, the V_{oc} value is approximately 0.61 V for the case shown in Figure 7-7.

Efficiency η is defined as

$$\eta = \frac{P_{max}}{P_{inp}} \quad (7.1)$$

where P_{max} is the maximum output power of the device and P_{inp} is the input power of the solar light. P_{max} is basically the maximum value of the product of I and V along the I-V curve. P_{inp} is the total input power of the solar light. Its value is approximately 100 mW/cm² for the input spectrum used in this simulation study. As the maximum power for the case shown in Figure 7-7 is approximately 17.5 mW/cm², the value of η approximately equals to 17.5% for this case.

The fill factor (FF) is defined using the expression

$$FF = \frac{P_{max}}{I_{sc}V_{oc}} \quad (7.2)$$

where I_{sc} and V_{oc} are the short circuit current and open circuit voltage respectively, which can be identified from the I-V curve. Note P_{max} can be geometrically taken as the largest rectangular within the I-V curve and the product of I_{sc} and V_{oc} is basically the rectangular whose corners are defined by the I_{sc} and V_{oc} spot together with the origin. FF can be geometrically

taken as the area ratio of these two rectangular. It has been discussed in early chapters that FF is sensitive with the series resistance of the device.

Note I_{sc} , V_{oc} , fill factor and efficiency are not four independent parameters. The efficiency can be calculated using I_{sc} , V_{oc} , and fill factor. Therefore, in the inverse process discussed later, the three output parameters used are only I_{sc} , V_{oc} , and fill factor.

Modeling of NREL champion device

The champion CIGS device in 2003 from NREL was modeled using Medici. This device has an efficiency of 19.2% with $I_{sc} = 35.71 \text{ mA/cm}^2$, $V_{oc} = 0.698 \text{ V}$ and $FF = 78.12\%$. Figure 7-8 shows the simulated I-V curve plotted together with the experimental data obtained by NREL. A reasonable agreement between simulation and experiment was achieved. This indicates the Medici forward modeling program may be used in the inverse process to automatically determine the appropriate values of some input parameters.

Inverse Modeling

Using the procedure described earlier, Matlab and Medici can be integrated to fulfill the inverse modeling process and identify important unknowns in the CIGS absorber layer. Matlab optimization toolbox was utilized for this purpose. The criteria “y” for optimization is shown in the following equation:

$$y = a \times \left(\frac{I_{sc} - I_{sc0}}{I_{sc0}} \right)^2 + b \times \left(\frac{V_{oc} - V_{oc0}}{V_{oc0}} \right)^2 + c \times \left(\frac{FF - FF_0}{FF_0} \right)^2 \quad (7.3)$$

where I_{sc0} , V_{oc0} and FF_0 are the targeted device performance value. Parameters a, b, and c are weighing factors to adjust the convergence preference among the three parameters. From the equation it is clear that during the minimization process of criteria y, the device performance parameters I_{sc} , V_{oc} , and fill factor approach their targeted values.

Three input variables were adjusted during the inverse process. They are three defect concentrations in the CIGS absorber layer. The interested defects in the CIGS layer are shallow level acceptor state, deep level electron trap and deep level hole trap. Their energy levels are assigned with reasonable values within the bandgap which are shown in Table 7-1. The inverse process is supposed to identify a set of input parameters that would yield certain output parameters. The search range for the three defects is between $2 \times 10^{17}/\text{cm}^3$ and $1 \times 10^{20}/\text{cm}^3$. Note that due to the complication of the forward model (the Medici simulation process), there could be more than one set of input parameters that would yield certain output parameters. In other word, the solution may not be unique.

Inverse Modeling of NREL champion device

The previous mentioned NREL champion device was used as the target for this inverse modeling process. This means the target performance was set so that $I_{sc0} = 35.71 \text{ mA}/\text{cm}^2$, $V_{oc0} = 0.689 \text{ V}$ and $FF_0 = 78.12\%$. Inverse modeling seeks a set of input values that yields the same performance values of the champion cell.

For the first run case, the starting values of the three defect concentrations are randomly chosen as 1×10^{19} , 5×10^{17} and $1 \times 10^{19}/\text{cm}^3$, respectively. This yields a performance parameter set of $V_{oc} = 0.500 \text{ V}$, $I_{sc} = 35.81 \text{ mA}/\text{cm}^2$, and $FF = 72.67\%$. The inverse process is then executed following the procedures described earlier in Figure 7-3. As shown in Figure 7-9, after only approximately 20 iterations, the three performance parameters are converged to values close to the target performance parameters. A set of defect concentrations with values 5.3×10^{19} , 6.6×10^{19} , and 2.6×10^{18} is identified to give a performance parameter set of $V_{oc} = 0.689 \text{ V}$, $I_{sc} = 35.7 \text{ mA}/\text{cm}^2$, and $FF = 78.4\%$.

The first run case was successful and very efficient. This can be contributed to a good initial guess which yields I_{sc} and FF close to their target value. For the second attempt, the initial

guess defect concentrations were taken as 5×10^{17} , 3×10^{18} and $8 \times 10^{17}/\text{cm}^3$. This reflects a performance parameter set of $V_{oc} = 0.357\text{V}$, $I_{sc} = 40.92 \text{ mA}/\text{cm}^2$, and $FF = 53.96\%$. Note none of these parameters are close to their final target value. The iteration process is shown in Figure 7-10. Compared with the first case, the second inverse process takes much more iterations to converge and stabilize at the target values. The variation of each of the three parameters also covers a much larger range. After approximately 80 iterations, a set of defect concentrations with values 5.2×10^{19} , 1.0×10^{20} , and $2.6 \times 10^{18}/\text{cm}^3$ is identified to give a performance parameter set of $V_{oc} = 0.688 \text{ V}$, $I_{sc} = 35.7 \text{ mA}/\text{cm}^2$, and $FF = 78.4\%$. Note that for the second inverse process, two defect concentrations converged to the same values that were obtained in the first run. Yet the electron trap concentration converged to another value which had the same order of magnitude. This suggests that the three output parameters are not very sensitive with the electron trap concentration.

For the third demonstration case, the defect concentrations were chosen at the upper boundary, which corresponds to values of 1.0×10^{20} , 1.0×10^{20} , and $1.0 \times 10^{20}/\text{cm}^3$. This makes the initial guess as far away as possible from the final converging point. With this initial guess, the performance parameters are: $V_{oc} = 0.500\text{V}$, $I_{sc} = 35.38 \text{ mA}/\text{cm}^2$, and $FF = 69.58\%$. As seen in the iteration process shown in Figure 7-11, after approximately 40 iterations, the performance parameters converged and stabilized at their targeted values. This yields a defect concentration combination of 5.3×10^{19} , 1.0×10^{20} , and $2.6 \times 10^{18}/\text{cm}^3$, the same point where the second case converged.

In conclusion, the inverse process is feasible to identify some input parameters in the CIGS layer. It has been demonstrated through different cases, no matter what the initial guess is, the sensitive parameters all converge to the same point. Yet the insensitive parameters can be

randomly located. This process can provide an alternative way to determine or at least shine light on some of the sensitive parameters that can not be easily measured through experiments. But numerical simulation can never completely replace experimental work. Theoretical predictions still need to be verified through experimental methods.

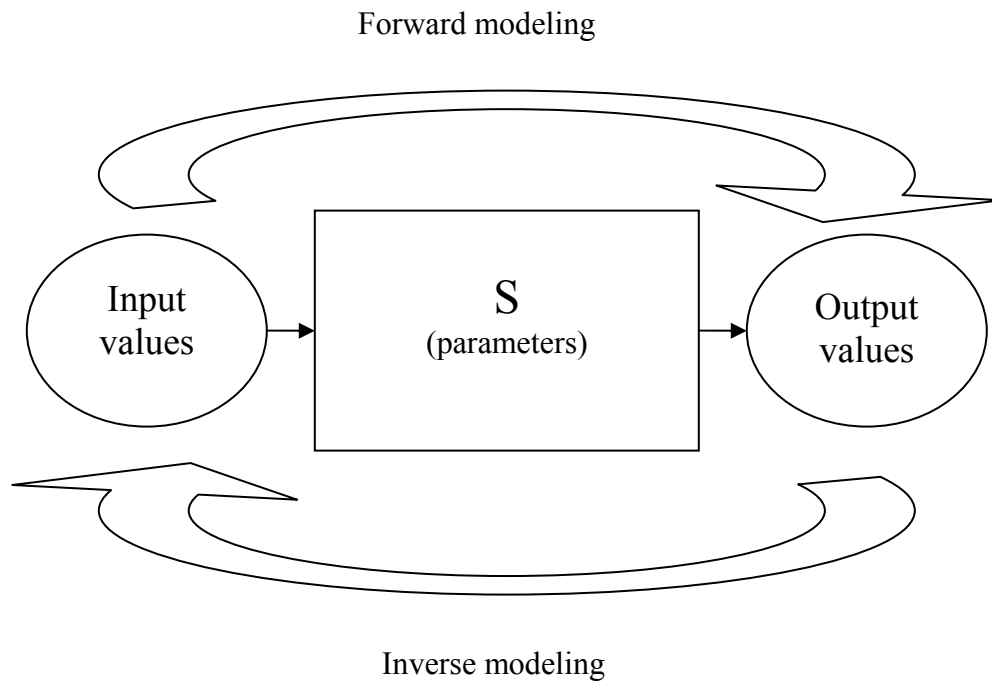


Figure 7-1. Schematic diagram illustrating the forward modeling and inverse modeling operations for a given physical system S

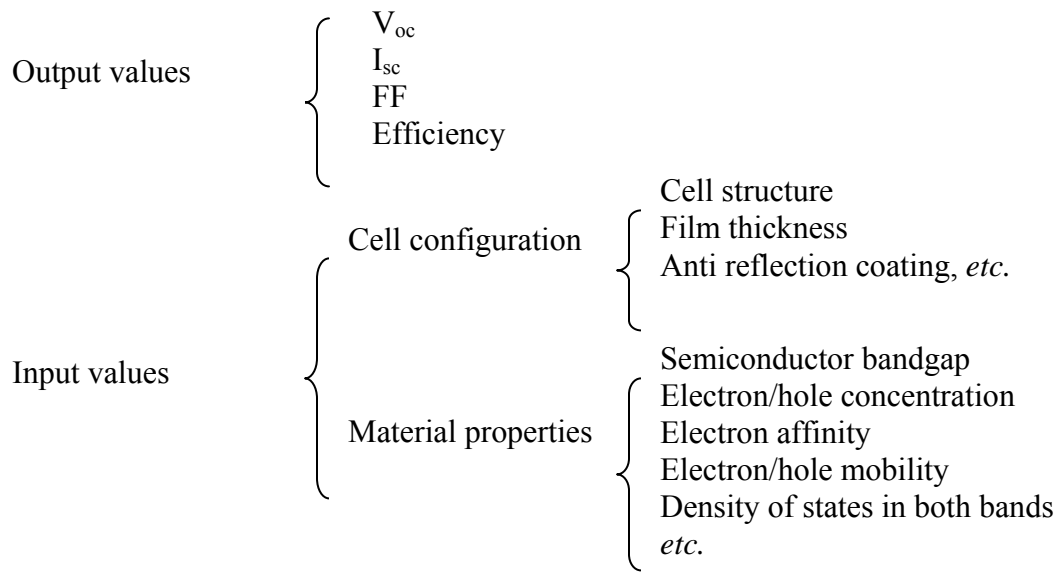


Figure 7-2. Parameter classification with examples for solar devices

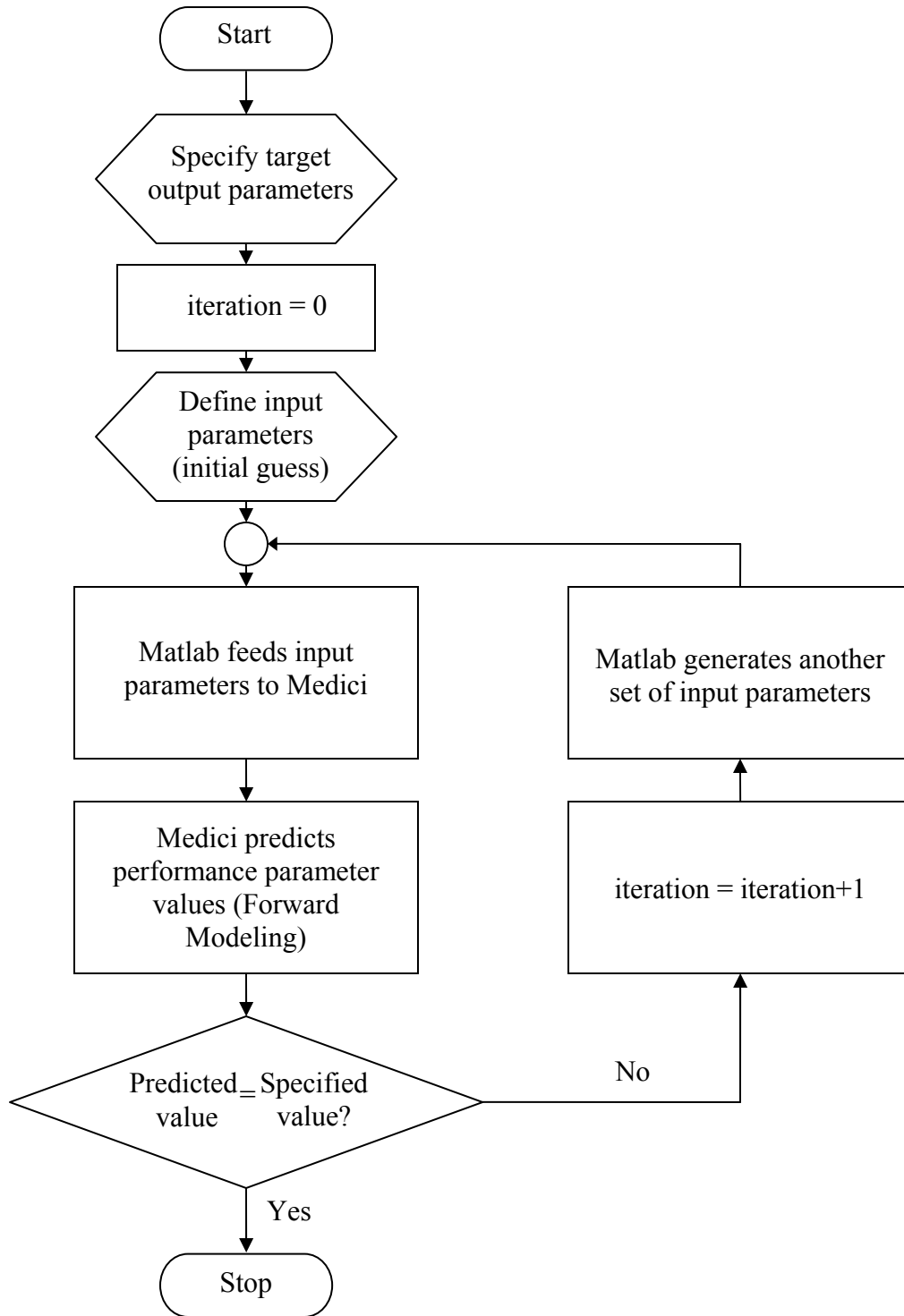


Figure 7-3. Procedure chart for solar cell inverse modeling.

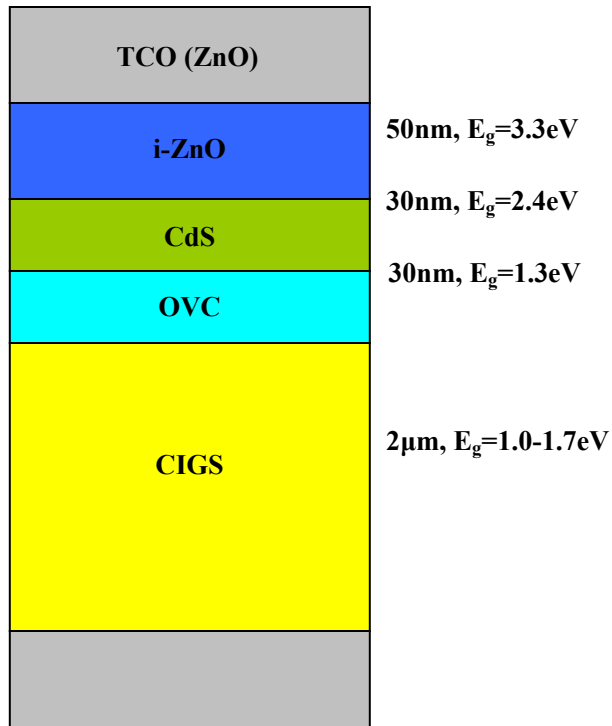


Figure 7-4. A typical CIGS cell structure.

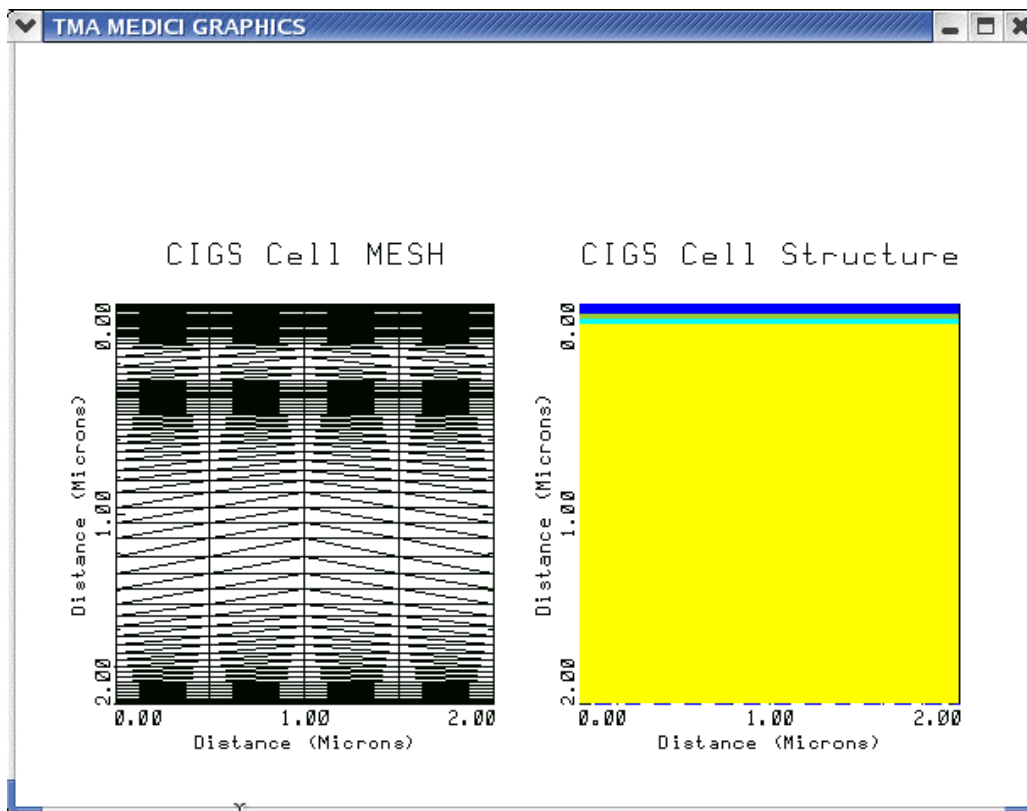


Figure 7-5. Cell structure described in Medici.

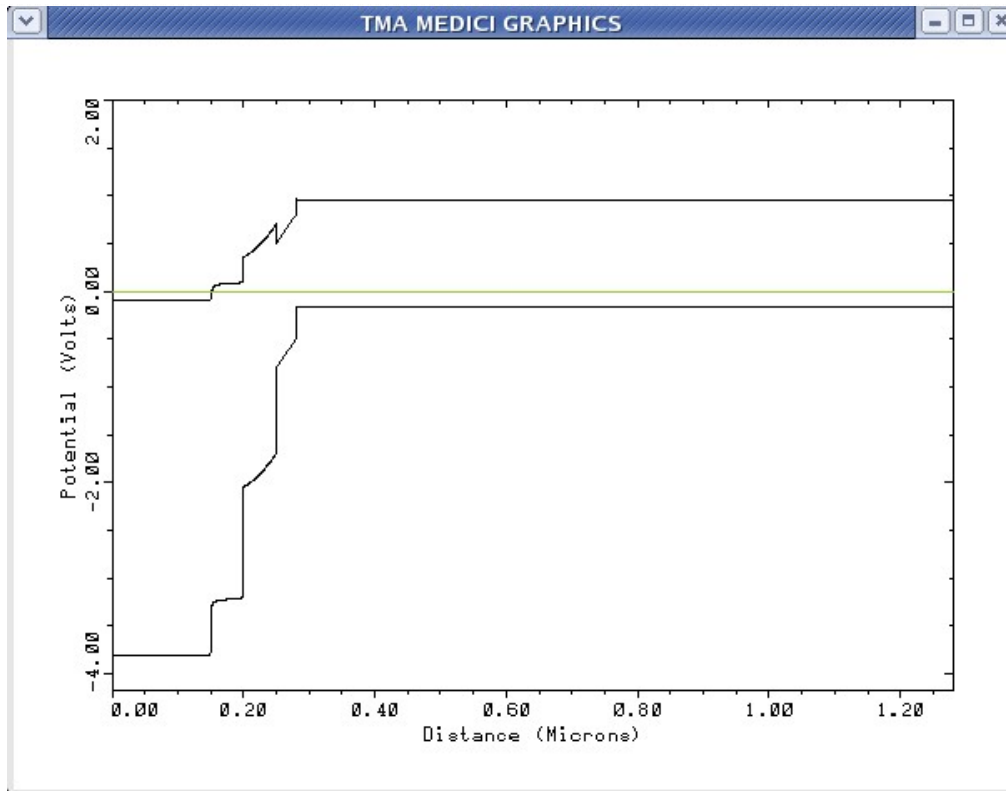


Figure 7-6. Bandgap profile of a CIGS device generated by Medici.

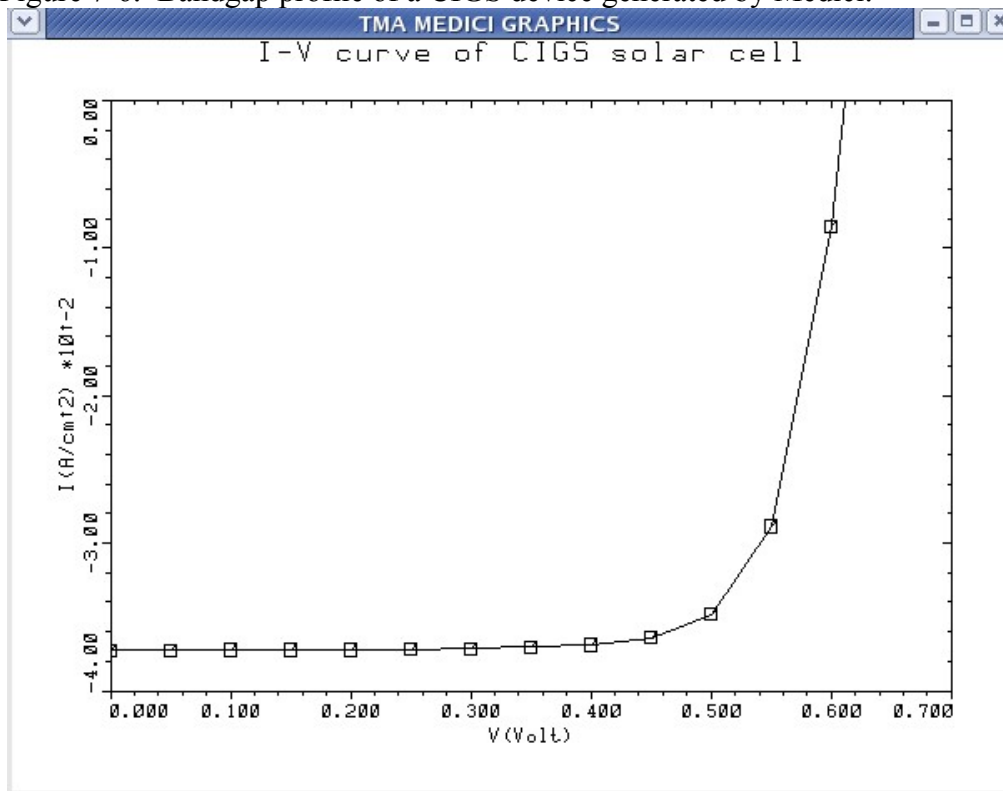


Figure 7-7. A typical I-V curve generated by Medici.

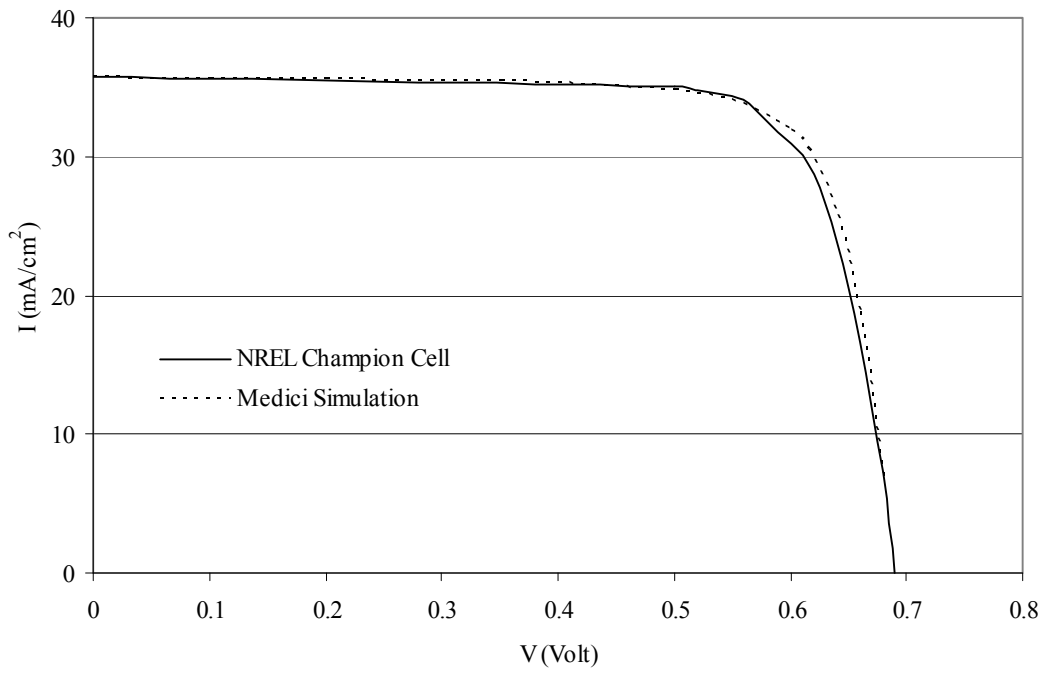


Figure 7-8. Medici simulation result for an NREL champion device.

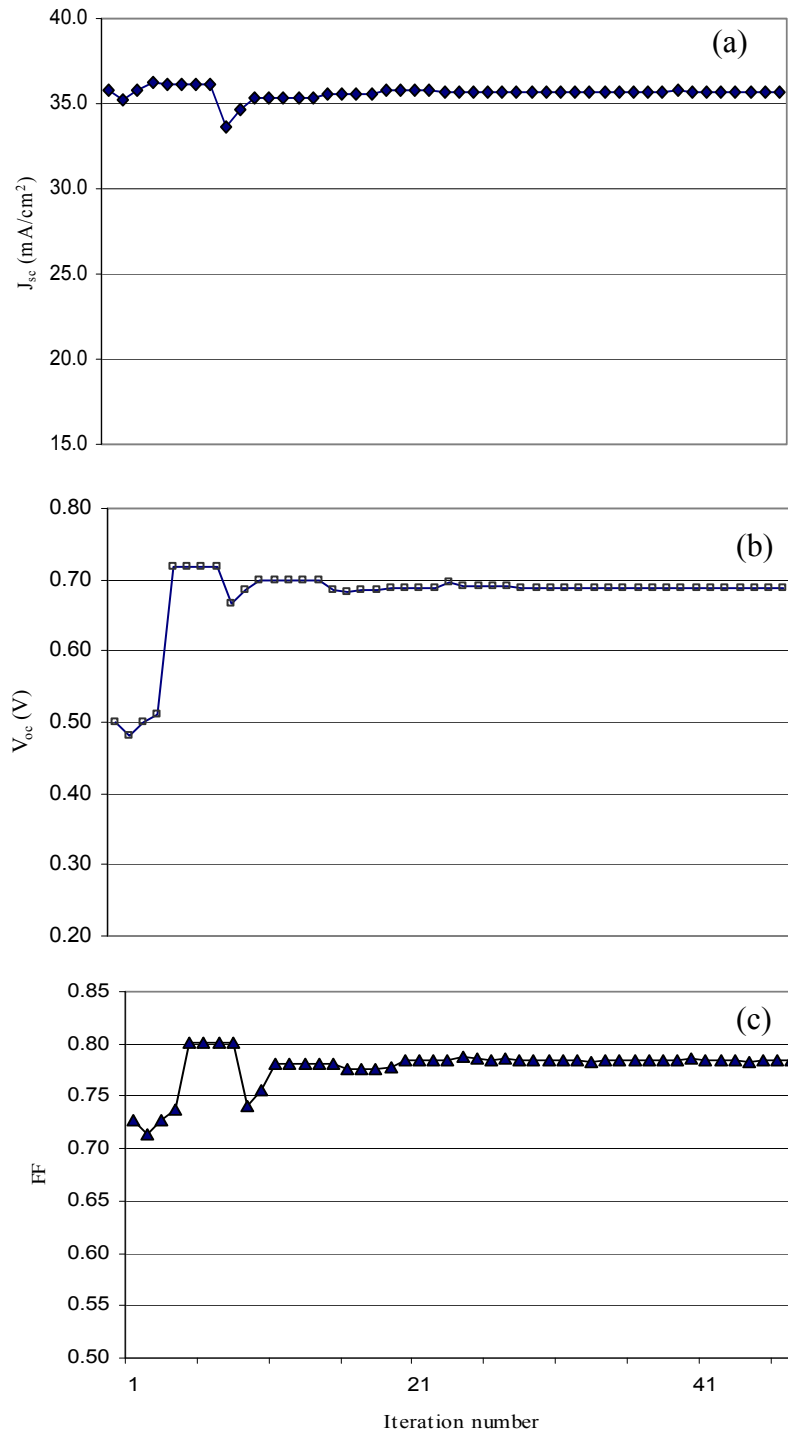


Figure 7-9. Iteration of inverse modeling process for there solar cell performance variables: (a) I_{sc} , (b) V_{oc} , and (c) FF . (Case 1)

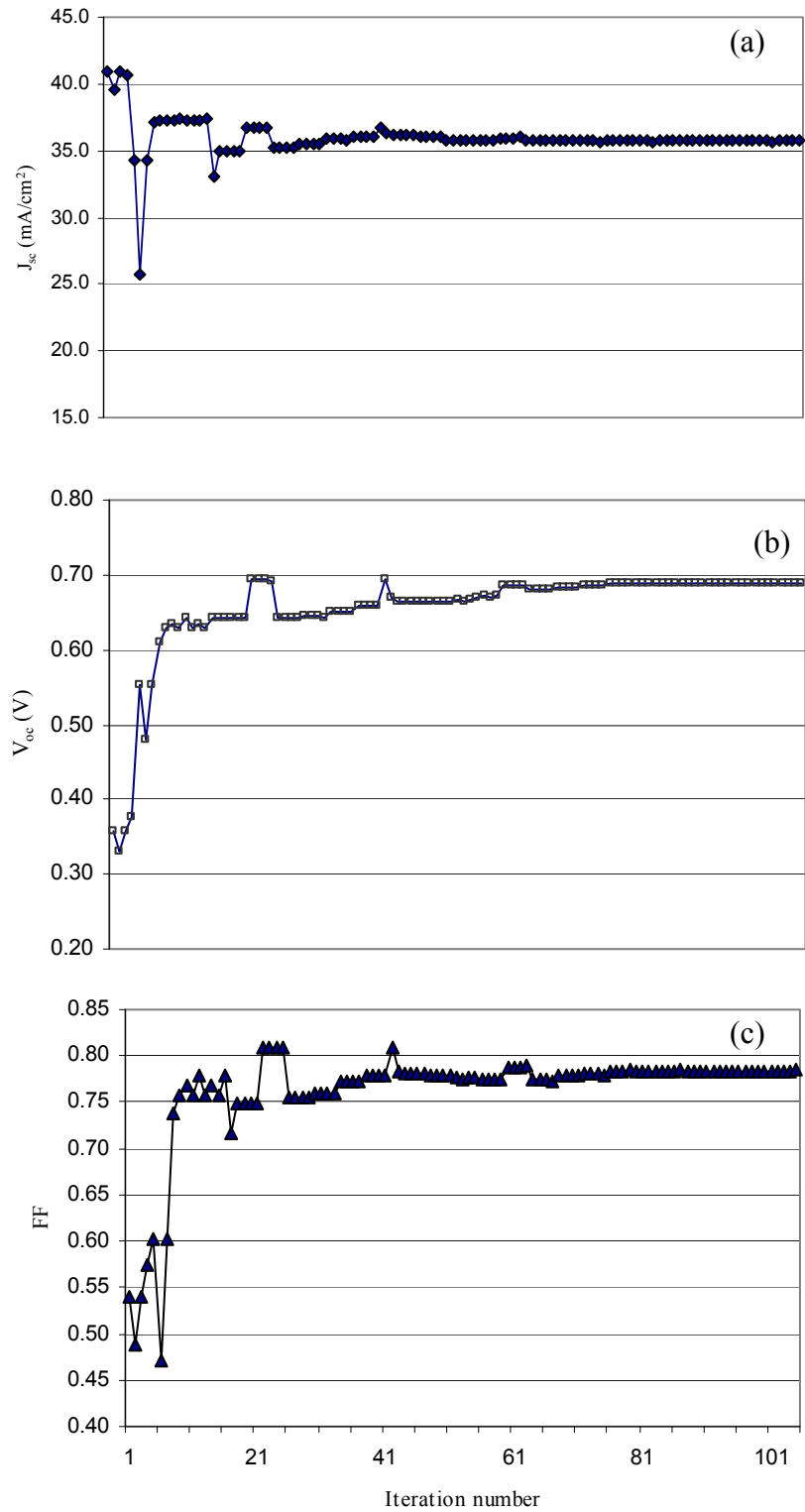


Figure 7-10. Iteration of inverse modeling process for there solar cell performance variables: (a) I_{sc} , (b) V_{oc} , and (c) FF . (Case 2)

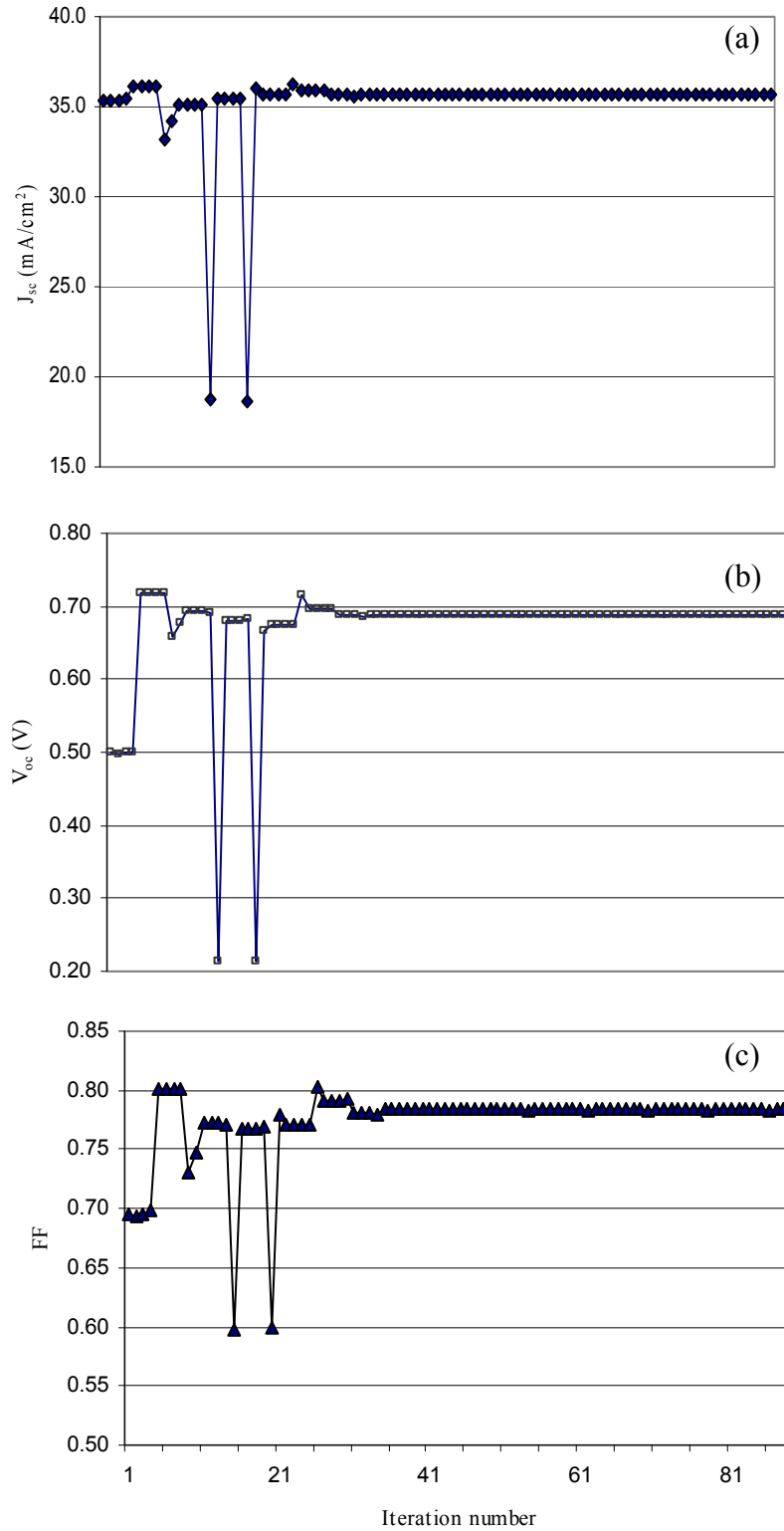


Figure 7-11. Iteration of inverse modeling process for there solar cell performance variables: (a) I_{sc} , (b) V_{oc} , and (c) FF . (Case 3)

Table 7-1. Typical input parameters for Medici.

Parameters	i-ZnO	CdS	OVC	CIGS
Thickness (nm)	50	30	30	2000
Electron affinity χ (eV)	4.0	3.75	3.95	3.8
E_g (eV)	3.3	2.4	1.3	1.12-1.4
Electron mobility (cm ² /V-s)	50	6	10	300
Hole mobility (cm ² /V-s)	5	3	5	30
Density of States in conduction band N_c (cm ⁻³)	1×10^{19}	1×10^{19}	6.6×10^{17}	3×10^{18}
Density of States in valence band N_v (cm ⁻³)	1×10^{19}	1×10^{19}	1.5×10^{19}	1.5×10^{19}
Doping Concentration (cm ⁻³)	5×10^{17}	6×10^{16}	1×10^{12}	N/A
Acceptor State Concentration N_{AS} (cm ⁻³)	N/A	N/A	N/A	5×10^{18}
Electron Trap Concentration N_{ET} (cm ⁻³)	N/A	N/A	N/A	1×10^{19}
Hole Trap Concentration N_{HT} (cm ⁻³)	N/A	N/A	N/A	2.8×10^{18}
Acceptor State Energy level (eV)	N/A	N/A	N/A	$E_v + 0.5E_g - 0.44$
Electron trap Energy level (eV)	N/A	N/A	N/A	$E_v + 0.5E_g + 0.2$
Hole Trap Energy level (eV)	N/A	N/A	N/A	$E_v + 0.5E_g - 0.2$

CHAPTER 8 CONCLUSION

Parameter Effects on Sputtered AZO

The sputtering system setup and deposition parameters greatly affect the optical and electrical properties of deposited AZO thin films. This is the reason for the significant disparities of best resistivity values reported in literature, which can be as high as several orders of magnitude.

The magnetron is a critical part of the experimental set up. The magnetic field created by the magnetron confines electrons near the surface of the target and consequently keeps the plasma close to the target surface instead of evenly distributed between the target and substrate. This reduces the damage done to AZO thin films through bombardment and improves the electrical properties of sputtered AZO thin film.

Zinc is very reactive with oxygen and if oxygen is included in the sputtering gas, its amount has to be small and accurately controlled. Otherwise the resistivity would be significantly increased. Generally for the Perkin Elmer sputtering system used, no oxygen is used during normal sputtering processes.

Deposition parameters can also affect the optical and electrical properties of AZO. Examples of such parameters are deposition power, working pressure and starting base pressure. Generally, increasing the deposition power would increase the sputtering rate, but it tend to reduce the optical transmission if no oxygen is present in the sputtering gas. This effect is done through the modification of the zinc and oxygen ratio at the target surface. When the deposition power is too high, the surface of the target can be reduced to a zinc rich mode if no oxygen is present in the sputtering gas. Depending on the degree of this reduced condition, optical transmission of AZO films deposited can drop to as low as zero. If the target is in such reduced

mode, a regeneration using argon and oxygen mixture gas is required. To prevent the target from reducing, a deposition power below 400W is suggested. Working pressure can also affect the sputtering rate and resistivity of AZO thin films and an operation under the optimized working pressure is recommended.

Experimental results showed a significant decrease of the resistivity with introducing hydrogen into the sputtering gas. It is also found that AZO resistivity is affected by the starting base pressure, which is related with the amount of residue water vapor, a source of hydrogen. These results support the theoretical predictions in literature that hydrogen acts as a doping source for zinc oxide thin films.

Device Fabrication

Window layer of thin film zinc oxide is critical for CIGS solar cells. It affects the solar cell performance through two mechanisms.

First, the thickness of zinc oxide affects the amount of photons that reaches the CIGS absorber layer. This is directly related with the optical transmission of the zinc oxide layer. When there is no antireflection layer present, the thickness of zinc oxide window layer can lead to different optical interferences, which could be constructive interferences or destructive ones. When constructive interference happens, a significant amount of light is direct back into the air without being able to enter the device. This could dramatically reduce the solar cell efficiency.

Second, the electrical property of zinc oxide layer is also very important. The sheet resistance of zinc oxide affects the series resistance of the device. It is known that the fill factor of solar cell is very sensitive with the series resistance. A slight increase of the series resistance could lead to a significant efficiency loss. Therefore, depositing zinc oxide with sufficient low sheet resistance is required for a good solar cell performance.

Defects in CIGS Absorbers

CIGS absorbers can be deposited using various methods including both vacuum and non-vacuum techniques. Performance of these CIGS absorbers can vary significantly. It has been a great interest to discover a theory to explain the disparities among the performance of these CIGS absorbers. Defect distribution is believed to be an important factor.

CIGS is not intentionally doped. The p-type conductivity comes from the various defects existing in the semiconductor. An increase of the shallow acceptor defect concentrations would increase the carrier concentration and simulation results showed a sharp increase of device performance.

An inverse modeling process was constructed and it can be utilized to identify the defect distributions corresponding to different solar cell performance. This could be used as a theoretical approach of determining defect properties to verify results experimentally obtained using DLTS.

Future Work

The experimental work on hydrogen doping of AZO thin films can be further investigated by using different concentrations of hydrogen for the sputtering gas. It is possible that increasing the hydrogen concentration would lead to even lower resistivity of the AZO thin film. An optimum concentration of hydrogen should be determined. It is of benefit to reduce the resistivity so that the same sheet resistance could be achieved with less thickness. This would reduce the material cost and also the processing time. Also thinner AZO window layer could reduce the photon absorption and optical interference if appropriate thickness is chosen.

For good uniformity on large size substrate, the AZO thickness variation should be carefully studied. A sputtering process that would yield good uniformity for large-scale industry

PV applications is desired. This could be achieved by choosing the right shape of the target and better arrangement of the magnetic field distribution.

The defect study on CIGS using inverse modeling should be accompanied by DLTS measurements. A combination of experimental and numerical tools could be of help to both individual techniques.

LIST OF REFERENCES

1. K. Zweibel, in *Harnessing Solar Power: The Photovoltaics Challenge*, (Plenum Press, New York, 1990).
2. L.L. Kazmerski, *International Material Review* **34**, 185 (1989).
3. L. Reith. *Sputter deposition of ZnO thin films*, Ph.D. Dissertation, University of Florida. 2001.
4. L. Kerr. *Growth and thermodynamic modeling of absorber and transparent conductive oxide for copper indium diselenide material based solar cells*, Ph.D. Dissertation, University of Florida. 2004.
5. J. Mazer, in *Solar Cells: An Introduction to Crystalline Photovoltaic Technology*, (Kluwer Academic Publishers, Boston, 1997).
6. P. Würfel, in *Physics of Solar Cells, from principles to new concepts*, (Wiley-Vch, 2005).
7. D. M. Chapin, C. S. Fuller, and G. L. Pearson, *Journal of Applied Physics* **25**, 676 (1954).
8. J. L. Shay, S. Wagner, and H. M. Kasper, *Applied Physics Letters* **27**, 89 (1975).
9. L. L. Kazmerski, F. R. White, and G. K. Morgan, *Applied Physics Letters* **29**, 268 (1976).
10. W. Chen *et al.*, *Conference Record of the Twenty Third IEEE Photovoltaic Specialists Conference*, 422 (1993).
11. K. Ramanathan *et al.*, *Progress in Photovoltaics* **11**, 225 (2003).
12. S. Li, in *Semiconductor Physical Electronics*, (Plenum Press, New York, 1993).
13. M. B. Prince, *Journal of Applied Physics* **26**, 534 (1955).
14. E. Bucher, *Applied Physics* **17**, 1 (1978).
15. T. Koyanagi, *Conference Proceeding 12th IEEE Photovoltaic Specialist Conference*, 627 (1976).
16. A. Goetzberger and V. U. Hoffmann, in *Photovoltaic Solar Energy Generation*, (Springer, 2005).
17. A. W. Blakers *et al.*, *Applied Physics Letters* **55**, 1363 (1989).
18. J. Dietl, D. Helmreich, and E. Sirtl, in *Crystals: Growth, Properties and Applications*, (Springer, 1981).
19. P. Stradins, *Solar Energy Materials and Solar Cells* **78**, 349 (2003).

20. D. L. Staebler and C. R. Wronski, *Applied Physics Letters* **31**, 292 (1977).
21. J. Muller, B. Rech, J. Springer, and M. Vanecek, *Solar Energy* **77**, 917 (2004).
22. S. Bose and A. K. Barua, *Journal of Physics D-Applied Physics* **32**, 213 (1999).
23. O. Kluth *et al.*, *Thin Solid Films* **351**, 247 (1999).
24. M. Yamaguchi, *Journal of Applied Physics* **78**, 1476 (1995).
25. J. Song *et al.*, NCPV and Solar Program Review Meeting 874 (2003).
26. R. G. Gordon, *MRS Bulletin* **25**, 52 (2000).
27. T. Minami, *MRS Bulletin* **25**, 38 (2000).
28. P. S. Nayar and A. Catalano, *Applied Physics Letters* **39**, 105 (1981).
29. X. Jiang, F. L. Wong, M. K. Fung, and S. T. Lee, *Applied Physics Letters* **83**, 1875 (2003).
30. D. H. Xu *et al.*, *Physics Letters A* **346**, 148 (2005).
31. J. Q. Zhao *et al.*, *Synthetic Metals* **114**, 251 (2000).
32. I. D. Kim *et al.*, *Applied Physics Letters* **89**, 022905(2006).
33. P. F. Carcia, R. S. Mclean, M. H. Reilly, and G. Nunes, *Applied Physics Letters* **82**, 1117 (2003).
34. H. C. Cheng, C. F. Chen, and C. Y. Tsay, *Applied Physics Letters* **90**, 012113 (2007).
35. J. Aranovich, A. Ortiz, and R. H. Bube, *Journal of Vacuum Science & Technology* **16**, 994 (1979).
36. M. S. Tomar and F. J. Garcia, *Thin Solid Films* **90**, 419 (1982).
37. M. G. Ambia, M. N. Islam, and M. O. Hakim, *Journal of Materials Science* **29**, 6575 (1994).
38. W. S. Lau and S. J. Fonash, *Journal of Electronic Materials* **16**, 141 (1987).
39. D. C. Agarwal *et al.*, *Journal of Applied Physics* **99**, 123105 (2006).
40. O. A. Fouad, A. A. Ismail, Z. I. Zaki, and R. M. Mohamed, *Applied Catalysis B-Environmental* **62**, 144 (2006).
41. J. H. Hu and R. G. Gordon, *Solar Cells* **30**, 437 (1991).
42. S. K. Tiku, C. K. Lau, and K. M. Lakin, *Applied Physics Letters* **36**, 318 (1980).

43. J. H. Hu and R. G. Gordon, *Journal of Applied Physics* **71**, 880 (1992).
44. T. Hada, K. Wasa, and S. Hayakawa, *Thin Solid Films* **7**, 135 (1971).
45. J. B. Webb, D. F. Williams, and M. Buchanan, *Applied Physics Letters* **39**, 640 (1981).
46. T. Minami, H. Nanto, and S. Takata, *Applied Physics Letters* **41**, 958 (1982).
47. D. M. Mattox, in *Handbook of Physical Vapor Deposition (PVD) Processing*, (Noyes Publications, Westwood, New Jersey, 1998).
48. K. Ellmer, *Journal of Physics D-Applied Physics* **33**, R17 (2000).
49. K. C. Park, D. Y. Ma, and K. H. Kim, *Thin Solid Films* **305**, 201 (1997).
50. C. R. Aita, R. J. Lad, and T. C. Tisone, *Journal of Applied Physics* **51**, 6405 (1980).
51. S. H. Jeong and J. H. Boo, *Thin Solid Films* **447**, 105 (2004).
52. A. Gupta and A. D. Compaan, *Applied Physics Letters* **85**, 684 (2004).
53. V. Sittinger *et al.*, *Thin Solid Films* **496**, 16 (2006).
54. M. A. Contreras *et al.*, *Progress in Photovoltaics* **7**, 311 (1999).
55. C. Agashe *et al.*, *Journal of Applied Physics* **95**, 1911 (2004).
56. K. K. Kim *et al.*, *Applied Physics Letters* **83**, 63 (2003).
57. Lake Shore 7500/9500 Series Hall System User's Manual (2000).
58. G. B. Hoflund, in *Handbook of Surface and Interface Analysis*, Edited by J. C. Riviere and S. Myhra (Marcel Dekker, Inc., New York, 1998), Chap. 4.
59. R. Jenkins and R. L. Snyder, in *Introduction to X-ray Powder Diffractometry*, (Wiley-Interscience, 1996).
60. H. P. Klug and L. E. Alexander, in *X-Ray Diffraction Procedures*, 2 ed., (Wiley, New York, 1974).
61. J. I. Pankove and N. M. Johnson, *Semiconductors and Semimetals* **34**, 1 (1991).
62. C. G. Van de Walle, *Physical Review Letters* **85**, 1012 (2000).
63. D. W. Hamby *et al.*, *Nuclear Instruments & Methods in Physics Research Section B-Beam Interactions with Materials and Atoms* **249**, 196 (2006).
64. A. Rockett *et al.*, *Thin Solid Films* **372**, 212 (2000).

65. A. F. da Cunha, F. Kurdzesau, and P. M. P. Salome, *Advanced Materials Forum Iii, Pts 1 and 2* **514-516**, 93 (2006).
66. J. R. Tuttle *et al.*, *Progress in Photovoltaics* **3**, 383 (1995).
67. M. A. Contreras, M. J. Romero, and R. Noufi, *Thin Solid Films* **511**, 51 (2006).
68. R. Caballero, C. Guillen, M. T. Gutierrez, and C. A. Kaufmann, *Progress in Photovoltaics* **14**, 145 (2006).
69. C. M. Xu *et al.*, *Chinese Physics Letters* **23**, 2259 (2006).
70. W. Li, Y. Sun, W. Liu, and L. Zhou, *Solar Energy* **80**, 191 (2006).
71. T. Wada *et al.*, *Physica Status Solidi A-Applications and Materials Science* **203**, 2593 (2006).
72. C. Eberspacher, C. Fredric, K. Pauls, and J. Serra, *Thin Solid Films* **387**, 18 (2001).
73. V. K. Kapur, A. Bansal, P. Le, and O. I. Asensio, *Thin Solid Films* **431**, 53 (2003).
74. B. J. Stanbery, Heteroepitaxy and nucleation control for the growth of metal chalcogenides using activated reactant sources, Ph.D. Dissertation, University of Florida, 2001.
75. Kincal S., Modeling and control of multiple thermal effusion sources and substrate temperature in molecular beam epitaxy reactors, Ph.D. Dissertation, University of Florida, 2002.
76. J. Song, Development, characterization and modeling of CGS/CIGS thin film tandem solar cells, Ph.D. Dissertation, University of Florida, 2006.
77. W. Chen, Cadmium Zinc Sulfide by Solution Growth, US patent 5,112,410 (1992).
78. K. Ramanathan, J. Keane, and R. Noufi, the 31st IEEE Photovoltaics Specialists Conference and Exhibition 195 (2005).
79. S. Ishizuka *et al.*, *Solar Energy Materials and Solar Cells* **87**, 541 (2005).
80. D. L. Young *et al.*, *Progress in Photovoltaics* **11**, 535 (2003).
81. N. Dhere *et al.*, NCPV and Solar Program Review Meeting, 853 (2003).

BIOGRAPHICAL SKETCH

Wei Liu was born in Hebei, China in April, 1978 and attended elementary school there. He moved with his family to Shandong, China in 1992 and spent his high school time in Yantai, Shandong. He attended Tsinghua University in 1996 and graduated with his BS of Chemical Engineering degree in year 2000. He then was recommended into the master program in the same department and received his MS of Chemical Engineering degree in 2002. During his study in the master program, he did part of his research projects in the Chemical Engineering department at University of Manchester Institute of Science and Technology (UMIST), Manchester, U. K. After obtaining his MS degree, he attended University of Florida and started pursuing his PhD degree in the Chemical Engineering department. His research focused on investigation of $\text{CuInSe}_2/\text{CdS}/\text{ZnO}$ material system and thin film photovoltaic device fabrication and characterization.